

# Moderator Design For Accelerator Based Neutron Radiography and Tomography Systems

by

Donald B. Puffer

Submitted to the Department of Nuclear Engineering in partial fulfillment of the requirements for the degree of

Master of Science in Nuclear Engineering

at the

MASSACHUSETTS INSTITUTE OF TECHNOLOGY

August 1994

© Massachusetts Institute of Technology, 1994. All Rights Reserved.

Author .....  
Department of Nuclear Engineering  
August 19, 1994

Certified by .....  
Dr. Richard Lanza  
Principal Research Scientist, Department of Nuclear Engineering  
Thesis Supervisor

Read by .....  
Dr. Jacquelyn Yanch  
Professor of Nuclear Engineering  
Thesis Reader

Accepted by .....  
Dr. Allen Henry  
Chairman, Committee on Graduate Students  
Department of Nuclear Engineering

MASSACHUSETTS INSTITUTE

NOV 16 1994

Science

# Moderator Design For Accelerator Based Neutron Radiography and Tomography Systems

by

Donald B. Puffer

Submitted to the Department of Nuclear Engineering on August 19, 1994, in partial fulfillment of the requirements for the degree of Master of Science in Nuclear Engineering

## Abstract

MIT is in the initial phase of developing a small accelerator based neutron imaging system. The system includes a radiofrequency quadrupole (RFQ) accelerator--producing neutrons by the reaction  ${}^9\text{Be}(d,n){}^{10}\text{B}$ --a neutron moderator, an object rotation platform, a  ${}^6\text{LiF-ZnS}$  scintillator screen converter, and an electro-optic cooled charged coupled device (CCD) detection system. The objective of this work was to design a neutron moderator which produces a high thermal neutron flux with a uniform flux distribution over a large area, using an accelerator based neutron source. Specifically, the objective was to produce a uniform thermal beam with an area greater than our scintillating converter screen, which has dimensions of 18 x 24 cm (432 cm<sup>2</sup>). Moderator designs producing a cylindrical thermal beam with a cross-sectional area of 491 cm<sup>2</sup> (12.5 cm radius) were analyzed theoretically using a Monte Carlo Neutron-Particle Transport simulation (MCNP) code from Los Alamos National Laboratory. A previously modeled neutron energy and angular distribution for 0.9 MeV  ${}^9\text{Be}(d,n){}^{10}\text{B}$  reaction was analyzed and used for all simulations. A moderator material was chosen after analyzing the moderating characteristics of several materials. The assessment of each moderator design was based on the magnitude and uniformity of the thermal beam flux. Geometric variables unique to each design were altered in an attempt to find the optimum configuration.

Thesis Supervisor: Dr. Richard Lanza  
Title: Principal Research Scientist

# Acknowledgments

I'd like to thank Dick Lanza for supervising this work and carefully reviewing this thesis; and for generously offering financial and intellectual support throughout. Dick is a special person, combining a deep knowledge of science with a childlike enthusiasm for his and his student's work. I have enjoyed working with him.

I thank Jackie Yanch for her careful review of this thesis; for her seemingly infinite supply of optimism; and for her intellectual and emotional assistance and support.

I thank Sidney Yip for his patience, wisdom, and understanding.

I thank Elias Gyftopoulos for not throwing me out of his office after I repeatedly refused to believe that bound electrons have no motion.

All have left an impression on me that will not easily be displaced.

Finally, I'd like to thank the department of Nuclear Engineering and the Harvard-MIT Division of Health Sciences and Technology for giving me the opportunity to study at MIT and Harvard Medical School.

# Table of Contents

<b>List of Figures</b> .....	6
<b>List of Tables</b> .....	9
<b>Chapter</b>	
<b>1 Introduction</b> .....	10
<b>2 Background and Theory</b> .....	17
<b>2.1 Neutron Imaging</b> .....	17
<b>2.1.1 Neutron Sources</b> .....	17
<b>2.1.2 Neutron Interaction With Matter</b> .....	22
<b>2.1.3 Neutron Interaction Cross-Section</b> .....	22
<b>2.1.4 Thermal Neutron Imaging</b> .....	24
<b>2.1.5 Neutrons vs. Photons</b> .....	25
<b>2.1.6 Neutron Detection</b> .....	29
<b>2.1.7 Image Quality</b> .....	30
<b>2.1.8 Computed Tomography</b> .....	32
<b>2.1.8.1 Filtered Back Projection</b> .....	32
<b>2.2 Image Detection</b> .....	35
<b>2.2.1 Charged Coupled Devices</b> .....	35
<b>2.2.1.1 Light to Charge Conversion</b> .....	36
<b>2.2.1.2 Quantum Efficiency</b> .....	36
<b>2.2.1.3 Charge to Voltage Conversion</b> .....	37
<b>2.2.1.4 Spectral Response</b> .....	38
<b>2.2.1.5 Noise Sources</b> .....	39
<b>2.2.1.5.1 Dark Current</b> .....	39
<b>2.2.1.5.2 Readout Noise</b> .....	39
<b>2.2.1.6 Detector Sensitivity</b> .....	40
<b>2.3 Accelerator Neutron Sources</b> .....	41
<b>2.3.1 Particle Accelerator Systems</b> .....	42
<b>2.3.1.1 Electrostatic Accelerators</b> .....	43
<b>2.3.1.2 Linear Radiofrequency Accelerators</b> .....	45
<b>2.3.1.3 Linear Radiofrequency Quadrupole Accelerators</b> .....	46
<b>2.3.1.4 Circular Radiofrequency Accelerators</b> .....	49
<b>2.3.1.4.1 Cyclotron Accelerators</b> .....	49
<b>2.4 Thermal Neutron Beam Production</b> .....	54
<b>2.4.1 Neutron Moderation</b> .....	54
<b>2.4.2 Beam Divergence and L/D Ratio</b> .....	60

2.5 MIT-NCT System.....	60
2.5.1 Accelerator System.....	60
2.5.2 Camera System.....	62
2.6 Summary.....	63
<b>3 Methods.....</b>	<b>64</b>
3.1 Monte Carlo Computer Code .....	65
3.2 Moderator Materials and Simulation Parameters .....	67
3.3 Thermal Beam Flux Assessment .....	68
3.3.1 Spatial Uniformity .....	68
3.3.2 Thermal Beam Flux Statistics.....	69
3.4 Summary.....	70
<b>4 Results and Discussion.....</b>	<b>71</b>
4.1 Energy and Angular Distribution for a 0.9 MeV $^9\text{Be}(d,n)^{10}\text{B}$ Reaction .....	71
4.2 Moderator Thermal Neutron Flux Density .....	75
4.3 Moderator Design .....	79
4.3.1 Moderator Material Assessment.....	79
4.3.2 Model I .....	80
4.3.3 Model II .....	84
4.3.4 Model III.....	88
4.3.5 Model IV.....	90
4.3.5.1 Variations on Model IV and Reflector Importance .....	95
4.4 Thermal Beam L/D Ratio .....	97
4.5 Summary.....	98
<b>5 Conclusions .....</b>	<b>101</b>
<b>References.....</b>	<b>103</b>
<b>Appendix I</b>	
Derivation of Neutron Cross-Section .....	107
<b>Appendix II</b>	
Neutron Beam Attenuation .....	109
<b>Appendix III</b>	
Neutron Source Energy-Angular-Flux Distribution .....	111
<b>Appendix IV</b>	
Moderator Thermal Neutron Flux Density .....	122

## List of Figures

<b>Figure 1.1:</b> Aircraft Age Tally .....	11
<b>Figure 1.2:</b> Maneuverable Neutron Radiography System.....	12
<b>Figure 1.3:</b> Schematic of Neutron Imaging System.....	14
<b>Figure 2.1:</b> Potential neutron yield from accelerator nuclear reactions .....	21
<b>Figure 2.2:</b> Mass absorption coeff. for thermal neutrons and 20 keV photons.....	26
<b>Figure 2.3:</b> (i) Neutron Radiograph, (ii) X-ray radiograph.....	28
<b>Figure 2.4:</b> Projection measurements.....	33
<b>Figure 2.5:</b> Spectral Response .....	38
<b>Figure 2.6:</b> Schematic of Cockcroft and Walton’s experiment.....	42
<b>Figure 2.7:</b> Schematic of a linear DC accelerator .....	43
<b>Figure 2.8:</b> Several DC accelerators including .....	44
<b>Figure 2.9:</b> Schematic of a linear RF accelerator.....	45
<b>Figure 2.10:</b> Schematic showing electromagnetic focuser and electrodes.....	46
<b>Figure 2.11:</b> Schematic of an RFQ resonator.....	47
<b>Figure 2.12:</b> Drawing of an RFQ with manifold.....	48
<b>Figure 2.13:</b> Schematic of a Cyclotron Accelerator.....	50
<b>Figure 2.14:</b> Cyclotron EM frequencies.....	52
<b>Figure 2.15:</b> Maximum energy transfer ratio .....	56
<b>Figure 2.16:</b> Scattered neutron energy distribution.....	57
<b>Figure 2.17:</b> Average energy after neutron scattering.....	58
<b>Figure 2.18:</b> Neutron thermalization distributions.....	59
<b>Figure 2.19:</b> AccSys Technology model DL-1 RFQ accelerator.....	61
<b>Figure 2.20:</b> Schematic of the camera system.....	62
<b>Figure 3.1:</b> Flux uniformity assessment geometry.....	69
<b>Figure 4.1:</b> Neutron energy spectra for ${}^9\text{Be}(d,n){}^{10}\text{B}$ reaction using 0.945 MeV deuterons.....	72
<b>Figure 4.2:</b> Accelerator neutron source energy distribution modeled by (65) for 0.9 MeV deuterons incident on a ${}^9\text{Be}$ target, assuming $10^{10}$ source intensity .....	73
<b>Figure 4.3:</b> Angular flux distribution for neutrons of all energies .....	74
<b>Figure 4.4:</b> Thermal Neutron Flux Density Moderator/Reflector Model. ....	76
<b>Figure 4.5:</b> Thermal neutron flux density for polyethylene (1-8 cm from source).....	77
<b>Figure 4.6:</b> Thermal neutron flux density for polyethylene (9-12 cm from source).....	78

<b>Figure 4.7:</b> Total thermal neutron flux density as a function of distance from source.....	78
<b>Figure 4.8:</b> Schematic (cross-section) of the Cylindrical Polyethylene and D <sub>2</sub> O-Polyethylene moderator. ....	81
<b>Figure 4.9:</b> Thermal neutron beam flux distribution for cylindrical polyethylene moderators .....	82
<b>Figure 4.10:</b> Thermal neutron beam flux distribution for cylindrical D <sub>2</sub> O-polyethylene moderator.....	83
<b>Figure 4.11:</b> Schematic (cross-section) of the void-slab polyethylene moderator and reflector .....	85
<b>Figure 4.12:</b> Thermal neutron beam flux distribution for the void-slab moderator.....	86
<b>Figure 4.13:</b> Schematic (cross-section) of the conical polyethylene moderator and reflector.....	89
<b>Figure 4.14:</b> MCNP generated cross-section diagram of the conical moderator.....	89
<b>Figure 4.15:</b> Thermal neutron beam flux distribution for the conical moderator. ....	90
<b>Figure 4.16:</b> Schematic (cross-section) of the spherical polyethylene moderator and reflector .....	92
<b>Figure 4.17:</b> MCNP generated cross-section diagram of the spherical moderator .....	92
<b>Figure 4.18:</b> Thermal neutron surface flux for spheres with different radii.....	93
<b>Figure 4.19:</b> Thermal neutron beam flux distribution for the spherical moderator .....	94
<b>Figure 4.20:</b> Three geometric perturbations of the 6 cm radius spherical moderator.....	95
<b>Figure 4.21:</b> Thermal neutron beam flux distribution for the 6cm spherical moderator; notched moderator; and cone-beam moderator .....	96
<b>Figure 4.22:</b> Thermal neutron beam flux distribution for the 6cm spherical moderator with and without a polyethylene reflector. ....	96
<b>APPENDIX III:</b> Neutron source energy and angular flux distribution plots .....	111
<b>Figure AIV.1:</b> Thermal neutron flux density for H <sub>2</sub> O (1-8 cm from source). ....	122
<b>Figure AIV.2:</b> Thermal neutron flux density for H <sub>2</sub> O (9-12 cm from source). ....	123
<b>Figure AIV.3:</b> Thermal neutron flux density for D <sub>2</sub> O (1-4 cm from source). ....	123
<b>Figure AIV.4:</b> Thermal neutron flux density for D <sub>2</sub> O (5-12 cm from source). ....	124
<b>Figure AIV.5:</b> Thermal neutron flux density for polyethylene with Be reflector (1-8 cm from source. ....	125
<b>Figure AIV.6:</b> Thermal neutron flux density for polyethylene with Be reflector (9-10 cm from source).....	126
<b>Figure AIV.7:</b> Thermal neutron flux density for H <sub>2</sub> O with Be reflector (1-4 cm from source).....	126
<b>Figure AIV.8:</b> Thermal neutron flux density for H <sub>2</sub> O with Be reflector (5-10 cm from source). ....	127

**Figure AIV.9:** Thermal neutron flux density for D<sub>2</sub>O with Be reflector (1-8 cm from source) ..... 128

**Figure AIV.10:** Thermal neutron flux density for D<sub>2</sub>O with Be reflector (9-10 cm from source). ..... 129



# List of Tables

<b>Table 2.1:</b> Some High-Flux Reactors And Their Properties .....	18
<b>Table 2.2:</b> Properties of Commercially Available Radioisotope Neutron Sources .....	20
<b>Table 2.3:</b> Thermal Neutron (0.025 eV) Linear Attenuation Coefficients For Compounds Found in Aluminum Corrosion .....	25
<b>Table 2.4:</b> Interaction Cross-Sections in Barns ( $10^{-24}$ cm <sup>2</sup> ) for 0.07 eV neutrons and 0.11nm X-rays .....	27
<b>Table 2.5:</b> Properties of Materials for Neutron Converter Screens .....	29
<b>Table 2.6:</b> Characteristics of Converter Screens .....	30
<b>Table 2.7:</b> Neutron Production From Commercially Available Accelerators .....	53
<b>Table 2.8:</b> RFQ Accelerator Operating Parameters.....	61
<b>Table 3.1:</b> Suggested Guidelines for Interpreting MCNP Error.....	66
<b>Table 3.2:</b> MCNP Parameters of Moderator/Reflector Material .....	67
<b>Table 4.1:</b> Polyethylene Moderator Flux Statistics .....	83
<b>Table 4.2:</b> D <sub>2</sub> O Moderator Flux Statistics .....	84
<b>Table 4.3:</b> Void-Slab Moderator Flux Statistics .....	87
<b>Table 4.4:</b> Conical Moderator Flux Statistics.....	90
<b>Table 4.5:</b> Sphere Moderator Flux Statistics .....	94
<b>Table 4.6:</b> Flux Statistics For Variations Of The 6 cm Radius Sphere Moderator.....	97
<b>Table 4.7:</b> Comparison of Spherical and Conical Moderator Flux L/D Ratio .....	98

# Chapter 1

## Introduction

In recent years, neutron radiography and tomography have become a valuable complementary imaging modality to photon imaging for industrial nondestructive evaluation and testing (NDE/NDT) of materials. The medical imaging analogy is the comparison of computed axial tomography (CAT) and magnetic resonance imaging (MRI). These two imaging modalities give the physician complementary information, with CAT yielding useful information of dense high atomic number material (bone) and MRI yielding useful information of soft tissue containing large amounts of hydrogen. Similarly, neutron radiography and tomography result in images differing from those produced using photons. This difference is due to neutrons interacting with the atomic nucleus rather than the surrounding electrons. Since the interactive process of neutrons with matter is nuclear, the characteristic attenuation of a beam of neutrons incident on a material can be very different from a beam of photons. Therefore, neutron radiography and tomography offer an alternative means of qualitatively and quantitatively evaluating a material's composition, yielding information not possible using photons.

Neutron radiographs and tomographic images have been used for many applications, some of which include: the analysis of building materials, plant research, inspection of electrical

components, detection of corrosion in aircraft components, evaluation of nuclear reactor fuel elements, and visualization of fluid flow (1-14). Despite the success of neutron imaging for these applications, and the potential for neutron imaging to become a valuable method of nondestructive evaluation for other industrial applications, neutron imaging has not been embraced by industry with overwhelming enthusiasm. The primary reason neutron imaging has been under utilized is the difficulty of producing an affordable and convenient neutron source of sufficient flux (neutrons/cm<sup>2</sup>-sec). At present, most neutron radiographs are produced using a nuclear reactor as the source. Nuclear reactors have the benefit of producing a very high neutron flux, however, this benefit is compromised by their high maintenance costs, immobility, general inaccessibility, and complexity of operation--including having to comply with Nuclear Regulatory Commission (NRC) regulations.

To emphasize the difficulty and limitations of a reactor source, consider one potential application of neutron imaging, for both industry and the military: detection of corrosion in the aluminum skin of airplane wings and fuselage. There are significant numbers of military and commercial airplanes which have been in operation for more than 25 years (Fig. 1.1); the

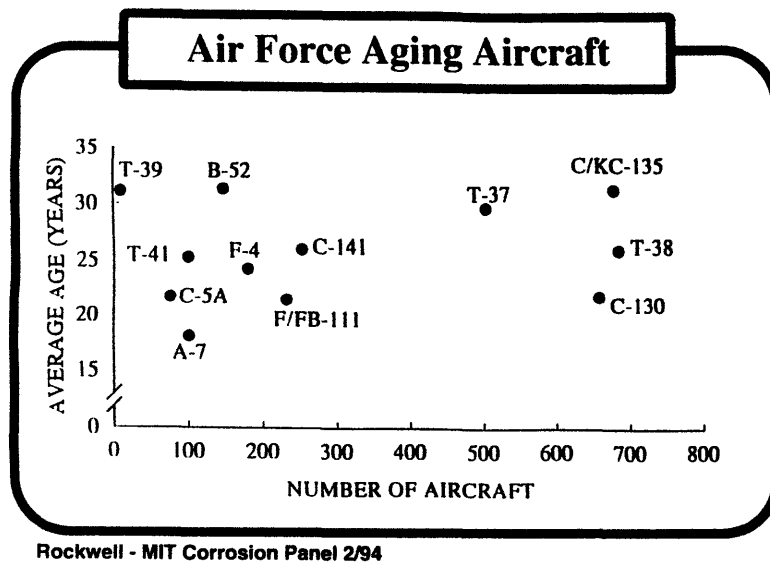
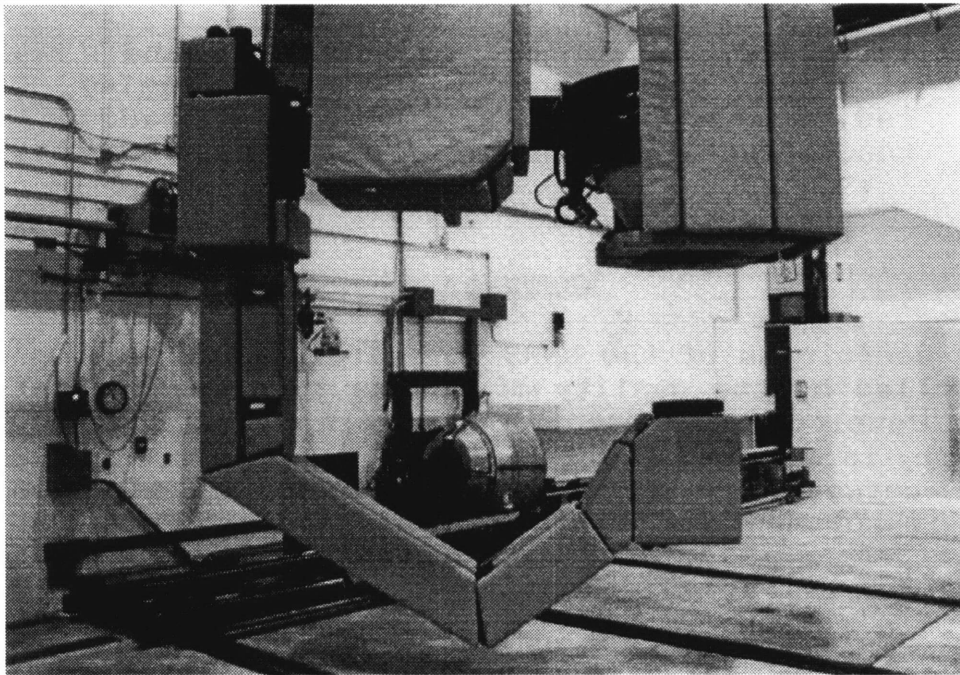


Figure 1.1: Aircraft Age Tally

economical incentive to repair these planes rather than replace them, makes detection of corrosion and repair an increasing objective (5,6). It is obvious that a neutron source which cannot be brought to the airplane is of little use, since it is not economically feasible for a plane to be dismantled for such an evaluation and then reassembled. However, if a compact neutron source could be mounted on a robotic arm and maneuvered about the airplane, this type of application becomes feasible. There is an ongoing effort in this direction by the Air Force, which began using a maneuverable  $^{252}\text{Cf}$  radioisotope neutron imaging system in 1990 (Fig. 1.2); however, due to the relatively low flux of radioisotopes, it would be advantageous to develop a maneuverable accelerator based system (5,6).



**Figure 1.2:** Maneuverable Neutron Radiography System used by the Airforce (5)

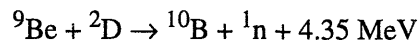
In addition to being able to move the source rather than move the object, a concern as to the accessibility of the source must also be considered. It becomes a disincentive to industry to use neutron imaging if they do not have the imaging system on-site. It is not feasible, from both an

economic and regulatory view, for companies to build their own nuclear reactor for the sole purpose of neutron imaging. Therefore, non-reactor neutron sources must be considered.

There are two alternatives to reactor based neutron sources: accelerators and radioisotopes. Radioisotope sources have the advantage of being technically easy to operate and maintain, and they are relatively small; however, radioisotope sources are typically much lower in intensity than accelerator sources; and since they are a continuous source, radiation protection is also a continuous concern, since there must be continuous monitoring of the radiation dosage to the engineers and technicians. Accelerator sources have the advantage of being able to be turned off when not in use, thereby eliminating the chance of accidental radiation exposure to workers when the accelerator is not in use. Accelerator sources are becoming smaller, more portable, more affordable, and, with the largest and most advanced, are beginning to equal the flux of small reactors (15). Even for smaller accelerators, though they are unable to match the neutron flux from reactors, their neutron flux has become sufficient for many applications (16,17).

Although high flux reactor sources are useful for high resolution radiographic and tomographic imaging of small engine parts and electrical components, if neutron imaging is to achieve widespread applicability the neutron source must be smaller and more easily maintained than a nuclear reactor; and for some applications, it must be maneuverable.

MIT is in the initial phase of developing a small accelerator based neutron imaging system. The system includes a radiofrequency quadrupole (RFQ) accelerator--producing neutrons by the reaction  ${}^9\text{Be}(d,n){}^{10}\text{B}$ --a neutron moderator, an object rotation platform, a  ${}^6\text{LiF-ZnS}$  scintillator screen converter, and an electro-optic cooled charged coupled device (CCD) detection system. A schematic of the system is shown in Fig. 1.3. Neutrons are produced by accelerating deuterium nuclei to an energy of 0.9 Mev; the high energy deuterons are directed into a beryllium target resulting in a nuclear reaction and the emission of high energy neutrons:



Since many materials have significant differences in neutron interaction cross-sections for low energy neutrons, and the efficiency of the LiF-ZnS scintillator screen is highest for neutrons in the thermal energy range (0.025 eV), the high energy fast neutrons emitted from the beryllium target will be slowed down (moderated) to thermal energies before interacting with the material to be imaged and the LiF-ZnS scintillator screen. Thus, a neutron moderator must be placed between the accelerator neutron source and the material being imaged.

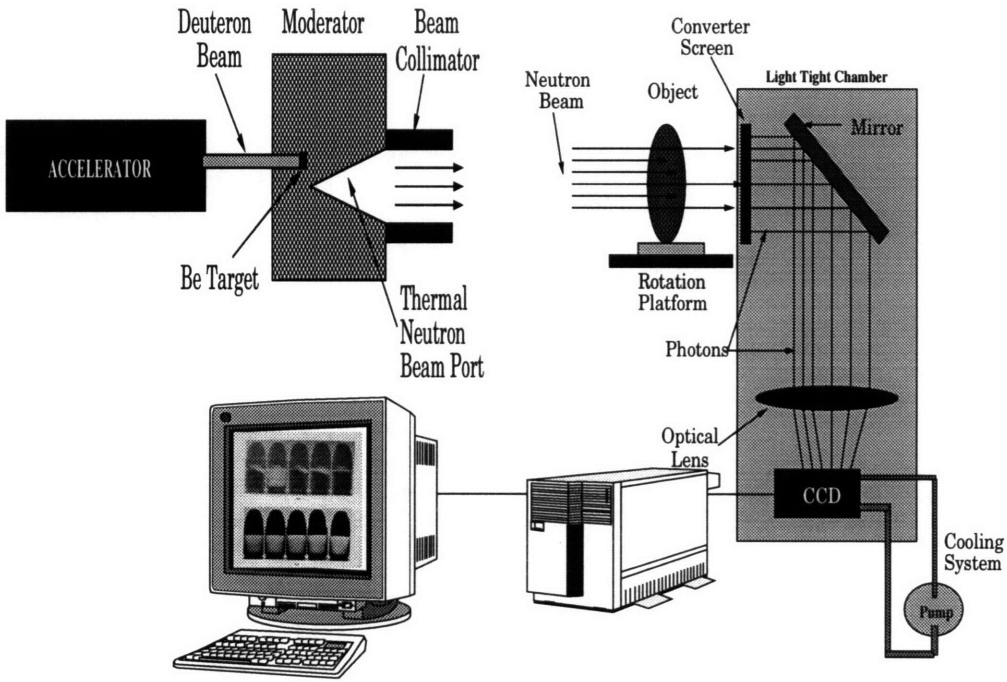


**Figure 1.3:** Schematic of Neutron Imaging System

Photons produced in the scintillator screen are reflected by a front-surface mirror and focused onto the CCD by an optical lens. This configuration allows the CCD to be out of the direct path of the residual neutron beam, thereby preventing damage to the CCD. The electrical charge produced in the CCD by the incident photons is digitized and stored in a computer as a two dimensional matrix which can be displayed and processed. This system is inherently a planar radiographic system, however, tomographic images can be reconstructed by acquiring many images as the object is rotated about one axis.

One major advantage of using an accelerator based neutron source for neutron radiography is that the size of the imaged area is not limited by the dimensions of a reactor's thermal neutron beam port. Thus, they have the potential for imaging larger objects, or larger areas of an object. The challenge, then, when using accelerator sources, is to produce a thermal neutron beam with a large cross-sectional area, and a high, spatially uniform, flux.

The objective of this work was to design a neutron moderator which produces a high thermal neutron flux with a uniform flux distribution over a large area, using an accelerator based neutron source. Specifically, the objective was to produce a uniform thermal beam with an area greater than our scintillating converter screen, which has dimensions of 18 x 24 cm (432 cm<sup>2</sup>). Moderator designs producing a cylindrical thermal beam with a cross-sectional area of 491 cm<sup>2</sup> (12.5 cm radius) were analyzed theoretically using a Monte Carlo Neutron-Particle Transport simulation (MCNP) code from Los Alamos National Laboratory (18). The neutron energy and angular distribution for 0.9 MeV  $^9\text{Be}(d,n)^{10}\text{B}$  reaction previously modeled (19) was analyzed and used for all simulations. A moderator material was chosen after analyzing the moderating characteristics of several materials. The assessment of each moderator design was based on the magnitude and uniformity of the thermal beam flux. Geometric variables unique to each design were altered in an attempt to find the optimum configuration.

Chapter 2 presents a general overview of the components and theory of accelerator based radiography and tomography systems, including: basic neutron physics, neutron imaging theory,

CCD detectors, particle accelerators for neutron sources, thermal neutron moderation and beam production, and a description of the MIT neutron imaging system; chapter 3 describes the methodology of moderator design and assessment; chapter 4 presents the results; and chapter 5 the conclusions.



# Chapter 2

## Background and Theory

### 2.1 Neutron Imaging

Radiography, either photon or neutron, is a two dimensional projection image of a three dimensional object, obtained by detection of the radiation transmitted through the object. Contrast in a radiograph is due to spatial differences in the attenuation of the radiation within the object. To understand the contrast within a radiograph, or the differences between radiographic methods, one must understand the interaction of radiation with matter. An attempt is made to give the reader the necessary information to understand neutron radiography and tomography, however, a complete description of neutron interactions with matter is beyond the scope of this thesis; the reader is referred to (13) for a detailed discussion.

#### 2.1.1 Neutron Sources

Essentially all neutron sources are based on neutron-producing nuclear reactions. These sources can be classified by the type of reaction into four groups: 1) fission, 2) fusion, 3) electron-

bremstrahlung-induced photoneutrons, and 4) accelerator based sources, including low energy ion nuclear reactions, high energy ion spallation, and photofission reactions (20).

Compared to radioisotope and accelerator based sources, nuclear reactor neutron sources have one big advantage: a relatively large neutron flux--typically well collimated by long beam ports extending from the moderator material near the reactor core to the laboratory. However, accelerators are beginning to rival reactors in both total and thermal neutron flux (see section 2.3). Depending on the power of the reactor, the core thermal neutron flux can reach  $10^{15}$  n/cm<sup>2</sup>-s (Table 2.1). As will be discussed in a following section, the resolution of a neutron radiograph is a function of the beam collimation and thermal neutron flux; in other words, for a given beam collimation, the time needed to acquire an image with a certain resolution is dependent on the neutron flux; therefore, it is desirable to use the largest flux possible.

**Table 2.1**  
**Some High-Flux Reactors And Their Properties**

Reactor	Power (MW)	Core Thermal Neutron Flux (n/cm <sup>2</sup> -s)	Coolant	Reflector
HFBR	60	$1.0 \times 10^{15}$	D <sub>2</sub> O	D <sub>2</sub> O
HFIR	100	$1.5 \times 10^{15}$	H <sub>2</sub> O	Be
HFR	57	$1.2 \times 10^{15}$	D <sub>2</sub> O	D <sub>2</sub> O
ORPH'EE	19	$0.3 \times 10^{15}$	H <sub>2</sub> O	D <sub>2</sub> O
HFIR II	200	$4.0 \times 10^{15}$	D <sub>2</sub> O	D <sub>2</sub> O

A significant limitation when using reactor sources--for industrial, academic, and military applications--is the need to bring the material or object to the reactor. With applications for neutron radiography expanding, there becomes an increasing need for 1) on-site neutron sources requiring only a small technical staff to operate and maintain, 2) sources capable of being used to image

large components or surface areas, and 3) sources capable of maneuvering about the object. Given these conditions, it is unlikely reactors will suit the emerging needs of industry, the military, or even academics.

One alternative is radioisotope sources. These sources are portable and can be incorporated into moveable structures that can be maneuvered about the object of interest (5); and radioisotope sources require little technical skill to operate. However, as illustrated in Table 2.2, the neutron yield achievable from these sources is exceedingly low compared to reactors, resulting in radiographs of much poorer quality and resolution for a given exposure time. They also pose a potential health risk due to the inability to abate the radiation when the source is not in use--shielding can be used to minimize the hazard, however, there is always the chance of a worker being exposed accidentally. Thus, from a nuclear regulatory and radiation safety perspective, these sources are not as attractive to industry as those that can be turned off. Additionally, since the flux is a function of half-life, the more intense sources often have disadvantageous half-lives.

Table 2.2 lists the commercially available radioisotopes. Californium-252 is by far the radioisotope of choice due to its small size, low  $\gamma$ -output, low average neutron energy, relatively long half-life (2.65 years), and yield per unit cost (21); as a result, Cf-252 has been used for several radiographic applications (5,22-24).

A third option, and perhaps optimal compromise, is a particle-accelerator based neutron source. Although these sources cannot presently equal the thermal neutron flux of reactors for highly collimated beams, their thermal flux is higher than radioisotope sources; they have the advantage of producing a neutron beam only when needed; accelerators are becoming small and compact enough to be incorporated in maneuverable imaging systems; and as the size and cost of accelerators decrease, the prospect for industry, universities, and military bases having on-site neutron sources becomes more realistic.

**Table 2.2**  
**Properties of Commercially Available Radioisotope Neutron Sources**

Isotope	Half-Life (Years)	Specific Activity (Ci/g)	Reaction	Neutron Yield (n/s-Ci)	Approximate Mean Energy (MeV)
$^{242}\text{Cm}$	163	9.3	$^9\text{Be}(\alpha, n)^{12}\text{C}$	$2.5 \times 10^6$	4, 6
$^{228}\text{Th}$	1.91	833	$^9\text{Be}(\alpha, n)^{12}\text{C}$	$2.0 \times 10^7$	4, 6
$^{252}\text{Cf}$	2.65	550	Spontaneous Fission	$4.3 \times 10^9$	2
$^{244}\text{Cm}$	18.1	83	$^9\text{Be}(\alpha, n)^{12}\text{C}$	$2.5 \times 10^6$	4, 6
$^{227}\text{Ac}$	21.8	74	$^9\text{Be}(\alpha, n)^{12}\text{C}$	$1.5 \times 10^7$	4, 6
$^{238}\text{Pu}$	86.4	17.9	$^9\text{Be}(\alpha, n)^{12}\text{C}$	$2.3 \times 10^6$	4, 6
$^{241}\text{Am}$	458	3.3	$^9\text{Be}(\alpha, n)^{12}\text{C}$	$2.2 \times 10^6$	4, 6
$^{226}\text{Ra}$	1620	1	$^9\text{Be}(\alpha, n)^{12}\text{C}$	$1.3 \times 10^7$	4, 6
$^{124}\text{Sb}$	60	49.4	$^9\text{Be}(\gamma, n)^4\text{He}$	$1.3 \times 10^6$	0.024

Several types of particle-accelerators using different nuclear reactions have been developed (21). The nuclear reactions that have been used include:

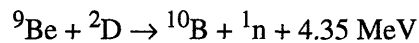
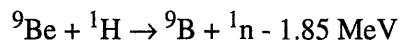
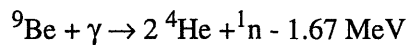
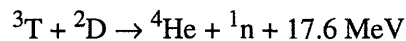
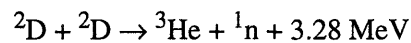
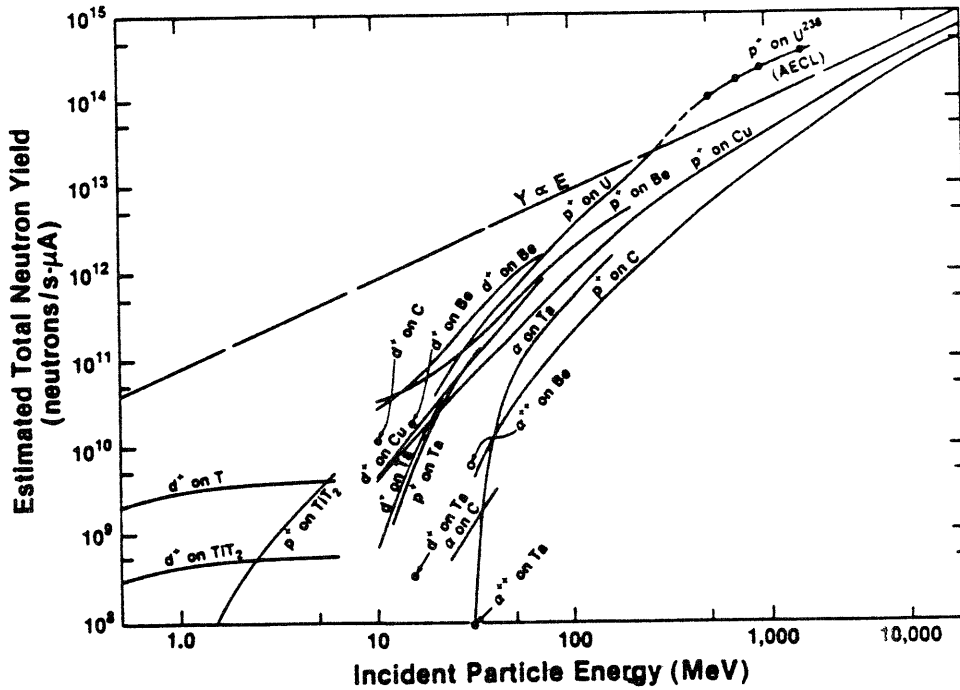


Figure 2.1 illustrates the potential neutron yield from these reactions as a function of incident ion energy.



**Figure 2.1:** Potential neutron yield from accelerator nuclear reactions as a function of incident ion energy (21).

One consideration when engineering a small accelerator is the maximum achievable energy of the bombarding ion. As a general rule, the smaller the accelerator the lower the maximum ion energy. Neutron yield increases with increased ion energy and current, therefore, a compromise must be made with respect to the size of the accelerator, beam current, beam energy, and neutron yield. Figure 2.1 indicates the reaction with the highest neutron yield per unit current at low energies is  $T(d,n)$ ; however, using tritium is disadvantages for thermal neutron radiography due to the very high energy neutrons emitted, and the short target life (21). The  $Be(d,n)$  reaction has proved to be a good choice due to its relatively high yield at low ion energies, and the durability and thermal conductivity of the beryllium target (melting point  $1285^{\circ}\text{C}$ ) resulting in long target

life (21). Accelerators using the Be(d,n) reaction are presently used for aerospace and other applications and appear to be the most suitable for future small accelerator sources (25-27).

### 2.1.2 Neutron Interaction With Matter

Due to the lack of electrical charge, neutrons are able to interact with nuclei in a large number of ways, and in ways differing from charged particles and photons. The lack of electrical charge allows the neutron to easily penetrate the electrical cloud of an atom and interact with the nucleus. Since there is no repulsive electrical force on the neutron by the nucleus, interaction with a nucleus can occur for neutrons with very low energies (meV range). To contrast this with charged particles, a proton or alpha particle must have energy in the MeV range to interact with the nucleus of even light elements having small electrical charge; and photons interact primarily with the surrounding electron cloud, very rarely penetrating to the nucleus and needing large energies (MeV range) to do so (28).

Neutron energy levels are divided into the following classifications:

Cold Neutrons	$E_n \approx < 0.025 \text{ eV}$
Thermal Neutrons	$E_n \approx 0.025 \text{ eV}$
Epithermal Neutrons	$E_n \approx 1 \text{ eV}$
Slow Neutrons	$E_n \approx 1 \text{ keV}$
Fast Neutrons	$E_n \approx 100 \text{ keV} - 10 \text{ MeV}$

Neutron energy can be estimated for low energy neutrons by assuming they are in thermal equilibrium with the medium ( $E_n = kT$ ).

### 2.1.3 Neutron Interaction Cross-Section

A common process when neutrons interact with a nucleus is the absorption of the neutron by the nucleus, forming a transient compound nucleus. Once the compound nucleus is formed, there are several things that can happen, each with a given probability dependent on the type of nucleus

and the kinetic energy of the incident neutron. The compound nucleus may 1) re-emit the incident neutron with its energy unchanged but heading off in a different direction (known as elastic scattering), 2) emit a neutron with more or less energy than the incident neutron (inelastic scattering), 3) emit a proton, alpha particle, more than one neutron, or a photon (radiative capture), or 4) fission into two or more lighter nuclides (28).

The probability that one of these result from a neutron interaction is quantitatively describe by a value known as the cross-section. However, we are rarely, if ever, interested in the interaction of a single neutron, since we almost always deal with material in bulk; therefore, the cross-section is defined the probability of interaction divided by the atomic density and distance traveled through the material, with units of  $\text{cm}^{-2}$ . The cross section,  $\sigma$ , then, is defined such that its product with the atom density,  $\rho$ , and distance  $dx$  is equal to the interaction probability,  $P_i$ :

$$\sigma = \frac{P_i}{\rho dx} \quad (2.1)$$

and is a function of the type of reaction, neutron energy, and target nuclide.

This quantity, with units of  $\text{cm}^{-2}$ , is known as the microscopic cross-section. It is an effective area used to characterize a single nucleus. It is a probability per unit nuclide density and per unit thickness of material through which the neutrons travel. There is also a macroscopic cross-section,  $\Sigma$ , with units of  $\text{cm}^{-1}$ . It is simply the product of the microscopic cross-section and the atom density of a material. The macroscopic cross-section is the probability per unit distance traveled that a neutron will interact with a material; therefore, it also is a function of reaction type, neutron energy, and target nuclide. (See Appendix I for a more detailed derivation of neutron cross-sections.)

## 2.1.4 Thermal Neutron Imaging

Most neutron radiographic systems exploit low energy thermal neutrons due to the larger difference, relative to fast neutrons, in interaction cross-sections among elements used for industrial materials. The larger interaction cross-sections for thermal neutrons means there is a larger differential attenuation of a neutron beam, and therefore, greater contrast in the radiograph. One important industrial concern is the detection of corrosion in aluminum structures. The presence of hydrogen, H<sub>2</sub>O, or aluminum hydrates in corrosion makes neutron imaging particularly sensitive to its detection. Table 2.3 lists the thermal neutron linear attenuation coefficients for aluminum and several compounds found in corrosion. As is discussed further in section 2.1.5, these large differences give neutrons an advantage over photons for detection of hydrogen mediated corrosion as well as other imaging applications.

Direct spatially localized detection of neutrons is difficult, therefore, neutron imaging systems incorporate a neutron-photon converter, placed between the transmitted neutron beam and the detection system (film or electro-optic). Within the converter, neutrons interact with the nuclei of the converter material, releasing secondary radiation; it is this secondary radiation that is detected by film or electronic sensor. These converter, or intensifier, screens are most effective for neutrons with thermal energies (see section 2.1.6). The disadvantage of using thermal neutrons is the limitation in the thickness of the object being imaged, since fast neutrons penetrate thicker material more readily.

As seen in the previous section, neutron sources other than reactors have primarily, or exclusively, fast neutron emissions. Thus, an important aspect of the non-reactor radiography system is the moderation (slowing down) of the neutrons before they reach the target object being imaged. Neutron moderation and thermal beam production is described in section 2.4.



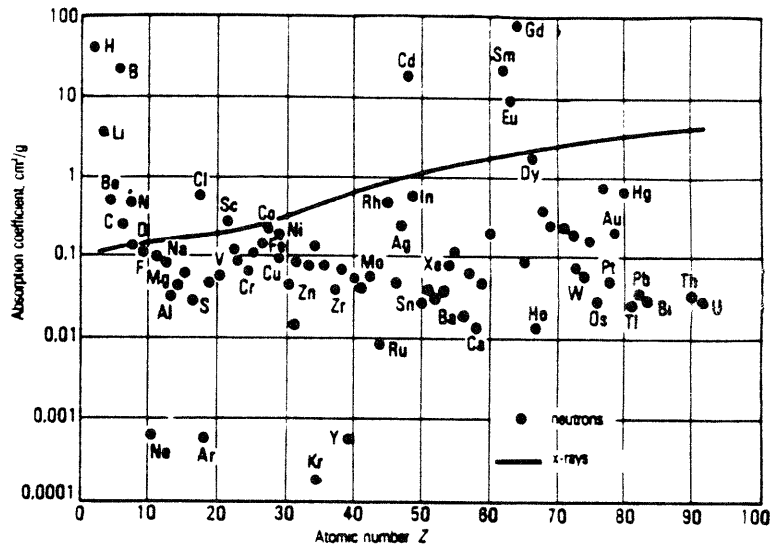
**Table 2.3**  
**<sup>a</sup>Thermal Neutron (0.025 eV) Linear Attenuation Coefficients**  
**For Compounds Found in Aluminum Corrosion**

Material	Density (g/cm <sup>3</sup> )	Linear Attenuation Coefficient (cm <sup>-1</sup> )	Relative Difference of Linear Attenuation Coefficient
Aluminum	2.7	0.1036	1.0
Al(OH) <sub>3</sub>	2.53	2.4	23.17
AlO(OH)	3.014	1.5	14.5
H <sub>2</sub> O	1.0	3.443	33.23

<sup>a</sup> From reference (7).

### 2.1.5 Neutrons vs. Photons

Due to the physical differences in neutron attenuation through matter compared to photons, neutron imaging is better able to distinguish certain elements within a material. Figure 2.2 is a plot of the mass absorption coefficients as a function of atomic number for thermal neutrons and 20 keV photons (29). Figure 2.2 illustrates the large difference in neutron mass attenuation coefficient for certain elements compared to photons. Depending on the composition of the material being imaged, neutron imaging has a great advantage over photon imaging.



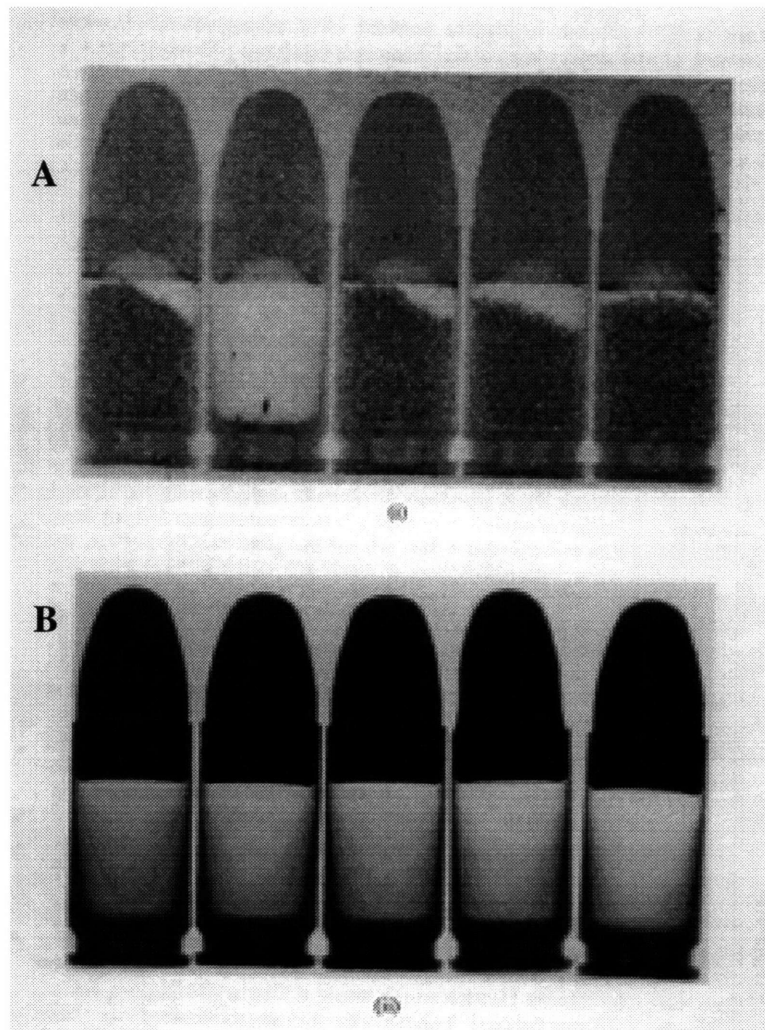
**Figure 2.2:** Mass absorption coefficients as a function of atomic number for thermal neutrons and 20 keV photons (29).

Table 2.4 lists the thermal neutron interaction cross-sections for several elements, and the total cross-sections for x-rays of approximately the same wavelength (28). In general, interaction cross-sections for photons increase with atomic number, whereas this is not the case for neutrons. The photon interaction at this wavelength is primarily absorption, and it is the value of absorption for the heavier elements that prevents photon radiography from detecting light elements within a heavy element material. Table 2.3-2.4 and Figure 2.2 make it clear that neutron radiography becomes a valuable and sensitive technique for applications such as the detection of boron in steel, and the detection of hydrogen mediated corrosion in materials such as aluminum.

**Table 2.4**  
**Interaction Cross-Sections in Barns ( $10^{-24} \text{ cm}^2$ )**  
**for 0.07 eV neutrons and 0.11nm X-rays**

Element	Neutrons			X-rays
	Scattering $\sigma_s$	Absorption $\sigma_a$	Total $\sigma_t$	Total $\sigma_t$
$^1\text{H}$	81	0.2	81.2	0.7
$^2\text{H}$	7.6	0.0005	7.6	0.7
Li	1.1	40	41.1	4.3
Be	7.5	0.005	7.5	9.8
B	4.4	430	434.4	18
C	5.5	0.003	5.5	36
O	4.2	0.0001	4.2	114
Mg	3.7	0.04	3.7	580
Al	1.5	0.13	1.6	810
S	1.2	0.3	1.5	1,780
Fe	11.8	1.4	13.2	11,900
Co	6	21	27	13,900
Ni	18	2.7	20.7	14,700
Cu	8.5	2.2	10.7	17,400
As	8	2.5	10.5	3,940
Ag	6.5	36	42.5	15,700
Au	9	57	66	28,000
Pb	11.4	0.1	11.5	33,200
Bi	9.4	0.02	9.4	35,000

Figure 2.3 illustrates the sensitivity of neutron radiography to the absorbing properties of hydrogen. Figure 2.3 shows five 9 mm revolver bullets, four of which are filled with a powdered hydrogenous propellant and one is empty. The empty cartridge is clearly distinguishable in the neutron radiograph, whereas X-rays result in no apparent distinction since most are absorbed by the metal casing.



**Figure 2.3:** (A) Neutron Radiograph, (B) X-ray radiograph. The empty cartridge is clearly distinguishable in the neutron radiograph, whereas X-rays result in no apparent distinction since most are absorbed by the metal casing (28).

## 2.1.6 Neutron Detection

Once the neutrons have been moderated to thermal energies and have passed through the target object, there must be a way to detect the transmitted neutrons and form an image reflecting the spatial difference in transmission. Since the direct detection of neutrons is difficult at high spatial resolution, all neutron radiographic systems use a converter-intensifier screen preceding the image formation step. Neutron interactions within the converter screen result in the emission of photons which are then detected by the image recorder. Although a large number of materials are possible candidates for converter screens (30,31), the materials most used include boron, lithium, gadolinium, dysprosium, and indium (21). Tables 2.5 and 2.6 list some of the nuclear properties of these elements and some characteristics of the screens made from them (21).

**Table 2.5**  
**Properties of Materials for Neutron Converter Screens**

Material	Thermal Neutron Absorption Coefficient	Predominant Nuclear Reaction	Type and Energy (MeV)	Screen Composition
${}^6\text{Li}$	$0.9 \text{ mm}^{-1}$	(n, $\alpha$ )	$\alpha$ 2.05	${}^6\text{LiF-ZnS}$ 250 $\mu\text{m}$
${}^{10}\text{B}$	$44.8 \text{ mm}^{-1}$	(n, $\alpha$ )	$\alpha$ 1.57	${}^{10}\text{B}_4\text{C}$ 5 $\mu\text{m}$
Gd	$140.3 \text{ mm}^{-1}$	(n, $\gamma$ )	IC $\beta^-$ 0.071	metal foil 25 $\mu\text{m}$
Dy	$3.01 \text{ mm}^{-1}$	(n, $\gamma$ )	$\beta^-$ 1.28 max	metal foil 100 $\mu\text{m}$
In	$0.73 \text{ mm}^{-1}$	(n, $\gamma$ )	$\beta^-$ 1.0 max	metal foil 250 $\mu\text{m}$

**Table 2.6**  
**Characteristics of Converter Screens**

Screen Type	Typical Thickness (mm)	Typical Thermal Neutron Registration Efficiency (%)	Inherent Unsharpness ( $\mu\text{m}$ )	Beam n/ $\gamma$ ratio for ~90%n/10% $\gamma$ image (n/cm <sup>2</sup> -mR)
NE 421	0.65	30	1000	$5 \times 10^4$
<sup>a</sup> NE 426	0.25	20	400	$5 \times 10^4$
NE 905	1.0	80	400	$2 \times 10^5$
Gd Foil	0.025	25	< 100	$10^6$
Dy Foil	0.1	10	200	0

<sup>a</sup> NE 426 is the most highly used <sup>6</sup>LiF-ZnS intensifying screen; produced by Nuclear Enterprises Ltd. Sighthill, Edinburgh, UK.

Many techniques have been used for recording the image formed by the secondary radiation emitted by these converter screens, including: photosensitive film (31-33), etchable plastic film (34,35), electronic/television image recorders (36-38), arrays of photomultiplier tubes (39), and electro-optic charged coupled devices (40-44). The choice of converter screen will depend on the particular image recording device used and the characteristics of the converter-recorder system, including: signal build-up with exposure, neutron registration efficiency, spatial resolving power, and half-life of the isotope emitting the secondary radiation. The reader is referred to (21) for a detail discussion of converter screen characteristics.

### 2.1.7 Image Quality

For any transmission imaging method the fundamental limitation on image quality is the statistical error inherent in the image formation process (41). Consider a beam of neutrons of fluence (neutrons/cm<sup>2</sup>),  $\phi$ , incident on a material with linear attenuation coefficient,  $\mu$ . If we

assume all interactions, both scattering and absorption, remove neutrons from the beam, and neglect the detection of scattered neutrons, then  $N$  particles will enter a detector pixel element of area  $(\Delta x)^2$  after losing  $\Delta N$  particles through interactions in the material:

$$\Delta N = \left[ \frac{d\mu}{\mu} \right] \mu \Delta x N \epsilon \quad (2.2)$$

where  $\epsilon$  is the efficiency of detection. Then,

$$N \approx \phi (\Delta x)^2 e^{-\mu L} \quad (2.3)$$

where  $L$  is the bulk dimensions of the material. To detect  $\Delta N$  above the noise requires that the detector statistical error,  $(N\epsilon)^{-1/2}$ , be less than  $\Delta N$ :

$$\sqrt{N\epsilon} \leq \left[ \frac{d\mu}{\mu} \right] \mu \Delta x N \epsilon \quad (2.4)$$

substituting for  $N$  gives:

$$\sqrt{N\epsilon} = \sqrt{\epsilon \phi (\Delta x)^2 e^{-\mu L}} \leq \left[ \frac{d\mu}{\mu} \right] \mu \Delta x (\phi (\Delta x)^2 e^{-\mu L}) \epsilon \quad (2.5)$$

It is now possible to calculate the minimum incident fluence to achieve a contrast-to-noise ratio  $\eta$ :

$$\phi > \frac{\eta^2 e^{\mu L}}{\epsilon \left[ \frac{d\mu}{\mu} \right]^2 \mu^2 (\Delta x)^4 \left[ \frac{\text{neutrons}}{\text{cm}^2} \right]} \quad (2.6)$$

This is the minimum fluence needed to resolve a feature of size  $\Delta x$  within a material of dimension  $L$  when the absorption cross-section of the feature differs from the bulk material by  $d\mu$ . For good contrast  $d\mu$  should be large. For materials such as aluminum contaminated with hydrogen,  $d\mu$  can be more than 100, making neutron imaging a good method of detecting hydrogen corrosion in aluminum; and, since,  $d\mu$  is typically much smaller for fast neutrons, it is advantageous to use thermal neutrons for neutron imaging (45); however, it must be noted that fast

neutron imaging is possible, and, since it is not necessary to moderate the neutrons, has the advantage of directly utilizing the higher fast neutron flux from non-reactor sources.

### **2.1.8 Computed Tomography**

The theoretical development of computed tomography has its roots in the analysis of Radon in 1917 (46), but it was not until Cormak (1969) and Hounsfield (1973) developed the first medical imaging system that the field took hold. Since then there has been a constant effort to develop faster, more accurate reconstruction algorithms (47).

The field of image reconstruction is large, however, it is fair to say that most techniques, or algorithms, have a foundation in the method of filtered backprojection (FBP). Therefore, FBP will be discussed, leaving the reader to explore for themselves more elaborate methods. In particular the method of cone-beam reconstruction (48) may be of interest, since it involves the reconstruction of images acquired using a conical transmission beam incident on an area detector; this may be an efficient method of neutron imaging when using non-reactor sources and a CCD detector, since the CCD is an area detector and the beam shape can be more easily manipulated using non-reactor sources.

#### **2.1.8.1 Filtered Back Projection**

Inherent to all transmission imaging systems is the detection of projection data. The objective of tomography is to reconstruct a planar slice of the object using these projection data. The projection data for parallel-beam tomography consists of parallel strip integrals through the object at various angles (Fig. 2.4). Typically, each angular position corresponds to a particular source-detector orientation, however, in non-maneuverable neutron radiography systems, the object is rotated instead of the source-detector system; the mathematical analysis is the same, however.



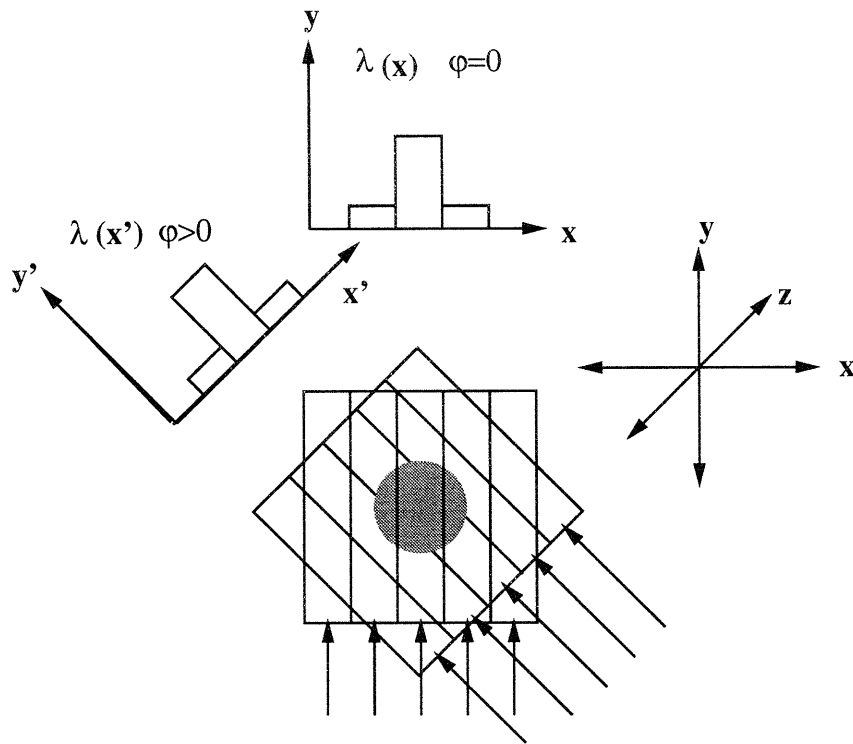


**Figure 2.4:** Projection measurements for an object at two different angular positions with 5 strip integrals (49). For radiography systems using an area CCD detector, strip integrals, for each image plane,  $z$ , at a particular angle,  $\phi$ , constitute a vector,  $\lambda(x')$  (see Eq. 2.10).

In back projection the projection measurements obtained at each angle (strip integrals) are projected back along the same line, essentially *smearing* the projection back over the integral line and assigning a value to each point on the image plane (pixel). As each projection is backprojected, the value of each pixel is incremented, i.e., the back projections are summed. Simply summing all the back projections results in a blurry image; to correct for this blur, the projection data are filtered with a ramp function before being back projected (47).

Mathematically, FBP begins with the projection data, which, for a transmission imaging system, are described by the positional attenuation of the radiation beam at various angular orientations,  $\phi$ , to the object (47):

$$I_z(x') = I_z^0(x') \exp\left[-\int \mu_z(x, y) dy'\right] \quad (2.7)$$

$$x' = x \cos \phi + y \sin \phi \quad (2.8)$$

$$y' = y \cos \phi - x \sin \phi \quad (2.9)$$

where  $I_z^0(x')$  is the intensity of the beam incident on the object at position  $(x', z)$ , where  $z$  is on the axis orthogonal to the tomographic image plane;  $I_z(x')$  is the intensity of the attenuated beam at position  $(x', z)$ ; and  $\mu_z(x, y)$  is the two dimensional distribution of the linear attenuation coefficient for the  $z^{\text{th}}$  tomographic image plane. For CCD image detectors, the image plane,  $z$ , refers to the row of the two dimensional data array; thus, CCD detectors acquire a two dimensional array of projection strip integrals.

For radiography systems using an area CCD detector, strip integrals, for each image plane,  $z$ , at a particular angle,  $\phi$ , constitute a vector,  $\lambda_z(x')$ :

$$\lambda_z(x') = -\ln\left[\frac{I_z(x')}{I_z^0(x')}\right] = \int_{-\infty}^{\infty} \int_{-\infty}^{\infty} \mu_z[x, y] \delta(x \cos \phi + y \sin \phi - x') dx dy \quad (2.10)$$

where the delta function,  $\delta$ , selects the path of the line integral (Fig. 2.4). If  $\Lambda_z(\omega, \phi)$  is the Fourier transform of  $\lambda_z(x')$ , and  $\chi(\omega)$  the Fourier transform of the filter function, then the pixel elements of the reconstructed image, for a given image plane,  $z$ , are:

$$\mu_z[x, y] = \int_0^{\pi} \int_0^{\omega_{max}} \Lambda_z(\omega, \phi) \chi(\omega) e^{i2\pi\omega x'} d\omega d\phi \quad (2.11)$$

The integrals represent continuous sampling of the data, however, in practice the sampling is digital and the integrals become summations.

## 2.2 Image Detection

Our system uses a  ${}^6\text{LiF-ZnS}$  converter scintillation screen to produce light from neutron interactions which is then detected by an electro-optic charged coupled device (CCD). This section describes the fundamental engineering and operation of CCD's. For a more comprehensive description see (50).

### 2.2.1 Charged Coupled Devices

Charged coupled device (CCD) image sensors are integrated circuits that convert a spatial distribution of radiation (optical image) into a time-distributed voltage signal; this voltage can then be digitized and stored in a computer. Thus a CCD sensor is an electro-optic interface in a digital imaging system. In recent years, CCD imaging systems have begun to find widespread applications (40-44). They are particularly useful for tomography, since tomographic images are formed from radiographic projections, and CCD's (being area detectors) acquire thousands of projection integrals simultaneously; and since the tomographic image is reconstructed digitally, having the radiographic data recorded digitally allows for a large dynamic range, low noise, and removes the necessity of digitizing photographic film.

A CCD recorder used for radiography is a two dimensional matrix of metallic oxide semiconductor (MOS) integrated circuits (IC). During exposure, light incident on the IC matrix is converted into a proportional quantity of electrical charge and stored in MOS capacitors. After exposure the accumulated charge in each capacitor is transferred sequentially down the line of capacitors to a readout diode. At the readout diode, the charge on each capacitor is sequentially converted into a voltage proportional to the charge. This voltage is amplified to produce a video signal which can be displayed directly or digitized by a computer.

### 2.2.1.1 Light to Charge Conversion

The initial step in converting light to charge in a CCD is accomplished with an array of photosensitive elements (pixels), which can be photodiodes or photoMOS elements. When a photon enters the silicon element an electron-hole pair is produced. The electron migrates to a depleted zone created by a diode or MOS structure while the hole recombines in the silicon substrate.

Once the charge has accumulated (exposure time) a charge transfer operation takes place which displaces the individual charges on the array such that they migrate along the array elements to the readout point. The time it takes for all the charges of the array elements (pixels) to migrate down the array and be read out is known as the readout time. The readout time will be dependent on the size of the array and is a factor in the amount of noise in the image.

### 2.2.1.2 Quantum Efficiency

Quantum efficiency,  $\epsilon$ , characterizes the sensitivity for each photosensitive element to convert light to charge; it is the ratio of the number of collected photocharges to the number of photons incident on the pixel area. Quantum efficiency is dependent on the pixel aperture (photosensitive area/pixel area), element structure (MOS or photodiode), and substrate structure (thickness of the optically sensitive area); and is evaluated to be:

$$\epsilon = \frac{Q}{E} = \frac{I\Delta t}{P\Delta t} = \frac{I}{P} \quad (2.12)$$

where Q is charge (C), E is energy (J), I is current (A), and P is power (W). Equation 2.12 is the energy conversion efficiency, however, since the wavelength of the incident light can vary, quantum efficiency is usually expressed in terms of electrons/photon:

$$E_\lambda = \frac{hc}{2\pi\lambda} = \frac{197.329 \text{ MeV} \cdot f}{\lambda (f)} \quad (2.13)$$

$$\varepsilon' \left( \frac{e^-}{\text{photon}} \right) = \varepsilon \left( \frac{C}{J} \right) \cdot 6.24 \times 10^{18} \left( \frac{e^-}{C} \right) \cdot 1.602 \times 10^{-13} \left( \frac{J}{\text{MeV}} \right) \cdot \frac{197.329}{\lambda} \left( \frac{\text{MeV} \cdot f}{f \cdot \text{photon}} \right) \quad (2.14)$$

$$\varepsilon' \left( \frac{e^-}{\text{photon}} \right) = \frac{1.97 \times 10^8 \varepsilon'}{\lambda} \quad (2.15)$$

were  $\lambda$  is the photon wavelength in units of fermis ( $f$ ) with energy  $E_\lambda$ ,  $c$  is the speed of light, and  $h$  is Plank's constant.

### 2.2.1.3 Charge to Voltage Conversion

Once the charge has migrated along the array it is converted to a voltage by the readout diode.

The voltage on the diode,  $V_L$ , will be

$$V_L = \frac{Q_L}{C_L} \quad (2.16)$$

where  $Q_L$  is the sensed charge and  $C_L$  is the sensing capacitance. When this voltage is amplified with gain  $G$ , an output video signal,  $V_{os}$ , is produced

$$V_{os} = G V_L = G \frac{Q_L}{C_L} \quad (2.17)$$

The output conversion factor,  $K$ , is typically expressed in  $V/e^-$  by factoring in electric charge,  $q_e$ :

$$K = q_e \frac{V_{os}}{Q_L} = q_e \frac{G}{C_L} \quad (2.18)$$

Using typical values for the gain,  $G$ , and capacitance,  $C_L$ , of 0.7 and 0.08 pF respectively:

$$K = \frac{1.602 \times 10^{-19} C}{e^-} \left( \frac{0.7}{0.08 \times 10^{-12} F} \right) = 1.4 \frac{\mu V}{e^-} \quad (2.19)$$

### 2.2.1.4 Spectral Response

Spectral response (SR) of a CCD is the relation between responsivity and the wavelength of the light incident on the photoelectric elements. Responsivity is the ratio of useful signal ( $V_{OS}$ ) to exposure, and therefore, is a function of quantum efficiency and charge-to-voltage conversion. The spectral response curve is then the plot of responsivity as a function of incident light wavelength. Figure 2.5 shows the spectral response for two CCD's. Figure 2.5 illustrates the dependence of the SR on the type of photoelectric element. The electro-optical characteristics are quite different below 700 nm, where the responsivity, i.e., the quantum efficiency, of MOS photoelements drops off rapidly compared to photodiodes; above 700 nm they are comparable. The difference in quantum efficiency below 700 nm results from the decrease in the mean free path with decreased wavelength of photons in the visual range, i.e, the ability of photons to penetrate material decreases with wavelength in the visual range; and with MOS elements, photons must penetrate the poly-silicon electrodes of the MOS element before entering the photosensitive silicon.

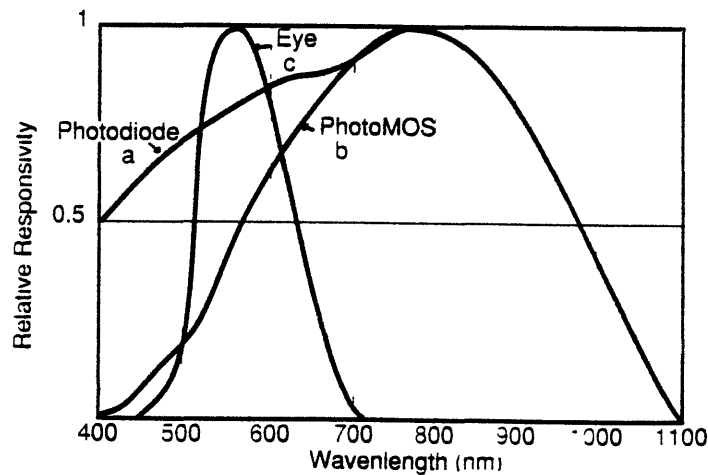


Figure 2.5: Spectral Response (50)

## 2.2.1.5 Noise Sources

The two most significant sources of noise are dark current and readout noise. They are not completely independent, but are the two main parameters used to characterize the noise.

### 2.2.1.5.1 Dark Current

Dark current voltage,  $V_{DS}$ , is generated in the silicon element by thermal motions of the electrons. If the thermal energy is sufficient, electrons can move into the conduction band where they are trapped and contribute to the detected charge, i.e., the detected signal from that pixel element. Thermal dark charge is a function of time and temperature, and is governed by the principle of intrinsic conduction by thermal carrier generation for semiconductors. This principle is quantified for CCDs by the general form for predicting the number of intrinsic charge carriers in a semiconductor,  $N$ , integrated over the time of exposure and readout:

$$N = C \int_{t_1}^{t_2} \exp\left[-\frac{E_g}{2kT}\right] dt \quad (2.20)$$

where  $E_g$  is the semiconductor gap energy needed for electrons to enter the conduction band,  $T$  is temperature in Kelvin,  $k$  is Boltzmann's constant, and  $C$  is constant over small temperature ranges (51).

Dark current typically varies by a factor of two for each  $7^\circ\text{C}$  change in temperature. Thus, it is beneficial to minimize the readout time, and essential to operate the CCD at the lowest possible temperature.

### 2.2.1.5.2 Readout Noise

Readout noise, or temporal noise, is defined as the fluctuation in time of a given pixel; it is generally referred to by the root mean square value of the detector array when no light is incident on the detector. Readout noise is influenced by several factors, including: 1) dark current, 2)

amplifier bandwidth, 3) reset noise, which is introduced when recharging the diode to its reference potential, and 4) transfer noise due to charge transfer efficiencies less than one.

Charge transfer efficiency (CTE) is a function of the drive clock frequency, which determines how fast the charges collected in the pixel array migrate to the readout diode. If the transfer efficiency is less than one, some of the electrons get left behind with each transfer. Therefore, a low charge transfer efficiency can result in both pixel variance and decreased resolution, since charges get spread over many pixels. With low CTE, the resolution will degrade across an image, with the last pixels to be read out having the lowest resolution; however, modern CCDs have CTE's in excess of 0.9999, virtually eliminating CTE non-linearities.

### 2.2.1.6 Detector Sensitivity

The photosensitive elements of a CCD are small ( $22.5 \times 22.5 \mu\text{m}$  for our detector), and even though a CCD can have a large array of these elements ( $1152 \times 1242$  for our detector), the overall area of the detection array is small; therefore, the use of a CCD detection system necessitates the miniaturization of the incident optical image. Miniaturization is accomplished with an optical lens, resulting in a large loss of detectable light. The fraction of light emitted by a Lambertian radiator (the scintillating screen in this case) that is captured by the lens is:

$$L = \frac{1}{(2F(m+1))^2} \quad (2.21)$$

where  $F$  is the f-number of the lens and  $m$  is the minification (41). The number of electrons produced in the CCD,  $N_e$ , for each incident neutron absorbed by the scintillator screen is then:

$$N_e = L \times \epsilon_L \times N_\gamma \times \epsilon_Q \quad (2.22)$$

where  $\epsilon_L$  is the transmission of the lens,  $\epsilon_Q$  is the quantum efficiency of the CCD, and  $N_\gamma$  is the light output of the screen in photons per neutron.



If we assume an ideal detector with signal-to-noise determined only by the statistics of the incident particles, then,  $(N)^{-1/2}$  will be the noise from  $N$  detected neutrons. The noise,  $\sigma_n$ , in terms of the number of neutrons in a CCD with  $N_e$  electrons per absorbed neutron, is:

$$\sigma_n = N^{1/2} \left(1 + \frac{1}{N_e}\right)^{1/2} \quad (2.23)$$

When dark current,  $N_{DC}$ , and readout noise,  $N_{RO}$ , are considered, the noise,  $\sigma_e$ , in terms of number of electrons generated in the CCD is:

$$\sigma_e^2 = NN_e^2 \left(1 + \frac{1}{N}\right) + N_{DC}^2 + N_{RO}^2 \quad (2.24)$$

For our CCD detector, 1 count is approximately 7-8 electrons, dark current at  $-50^\circ\text{C}$  is rated at 3-6 electrons/pixel/second, and readout noise is reported to be 1-1.2 RMS counts (52).

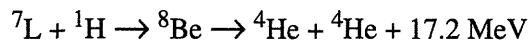
## 2.3 Accelerator Neutron Sources

The neutron source to be used for the MIT Neutron Computed Tomography (MIT-NCT) project is a radiofrequency quadrupole (RFQ) linear accelerator. This accelerator uses the electrical component of a variable radio-frequency electromagnetic field to accelerate deuterium nuclei along a linear path to an energy of 0.9 MeV, using the quadrupole magnetic component to focus the particle beam onto a  $^9\text{Be}$  target. Deuterons incident on the target interact with the  $^9\text{Be}$  nuclei, producing neutrons with energies ranging from 1-5 MeV (see results).

All accelerator based neutron sources share the common method of bombarding a target element with particles accelerated to high energies. This section discusses the various means of particle acceleration. For a detailed presentation of particle accelerator theory the reader is referred to (53-55); for a thorough review of accelerator applications see (56).

### 2.3.1 Particle Accelerator Systems

In 1927, Rutherford proposed that new nuclear transformations could be accomplished by bombarding the nuclei of various substances with hydrogen ions (protons) accelerated to high velocities using a direct-current (DC) generator (55). In 1928 Wideroe used a linear accelerator to accelerate potassium and sodium ions (55,57); in 1932 Lawrence and Livingston accelerated the first proton beam using their newly developed cyclotron (55,58); however, the first charged particle accelerator used to investigate Rutherford's hypothesis was developed by Cockcroft and Walton, also in 1932 (55, 59). Cockcroft and Walton developed what they called a proton gun, in which hydrogen atoms were ionized by electrons moving through hydrogen gas and accelerated to an energy of 150 keV by a constant 150 kV potential; a lithium target was placed in the path of the proton beam (Fig. 2.6). Using this device they were able to observe particles emitted from the lithium target and hypothesized the nuclear reaction:



This experiment was the first nuclear transformation produced using a non-radioisotope source of charged particles. Since then, accelerators have been applied in many areas of science and engineering (56), however, their initial development and motivation for advancement are rooted in nuclear physics.

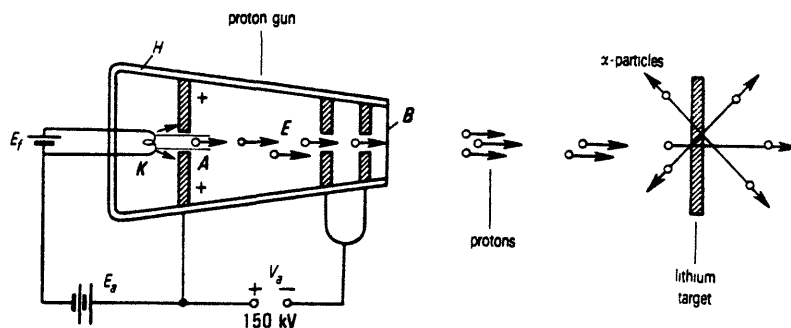


**Figure 2.6:** Schematic of Cockcroft and Walton's experiment with the first particle accelerator (55).

Particle accelerators are based on the interaction of electric charge with either static voltage potentials or dynamic electromagnetic (EM) fields. Accelerators utilize EM fields ranging from nearly static to radiofrequency (MHz) and GHz fields. Several different types of accelerators now exist, each differing in the method of acceleration and/or particle accelerated, and the maximum particle energy.

### 2.3.1.1 Electrostatic Accelerators

In electrostatic, also known as direct-current (DC), accelerators, a potential difference between two electrodes is used to accelerate charged particles. The simplest design has both sides of an evacuated linear accelerating chamber connected to a high-voltage generator; a large voltage potential difference between the charged particle source and the opposite end of the chamber accelerates the ions (Fig. 2.7). The final energy of the ions is determined by the potential difference of the chamber. More elaborate designs contain many electrodes throughout the acceleration chamber, making the voltage gradient more uniform. Several types of DC accelerators have been developed including: cascade generators, Van de Graaff accelerators, and induction accelerators (Fig. 2.8). The primary difference between these DC accelerators is their method of generating a high voltage potential.

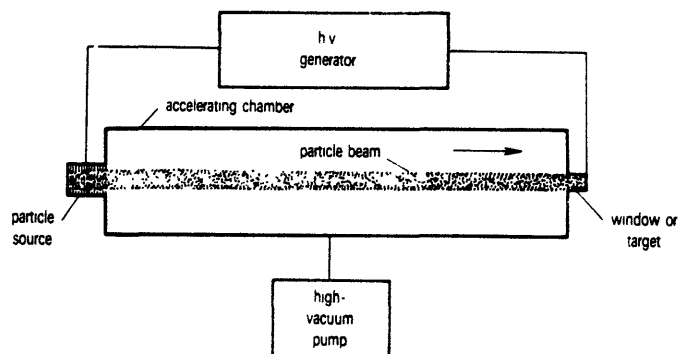


**Figure 2.7:** Schematic of a linear DC accelerator (55).

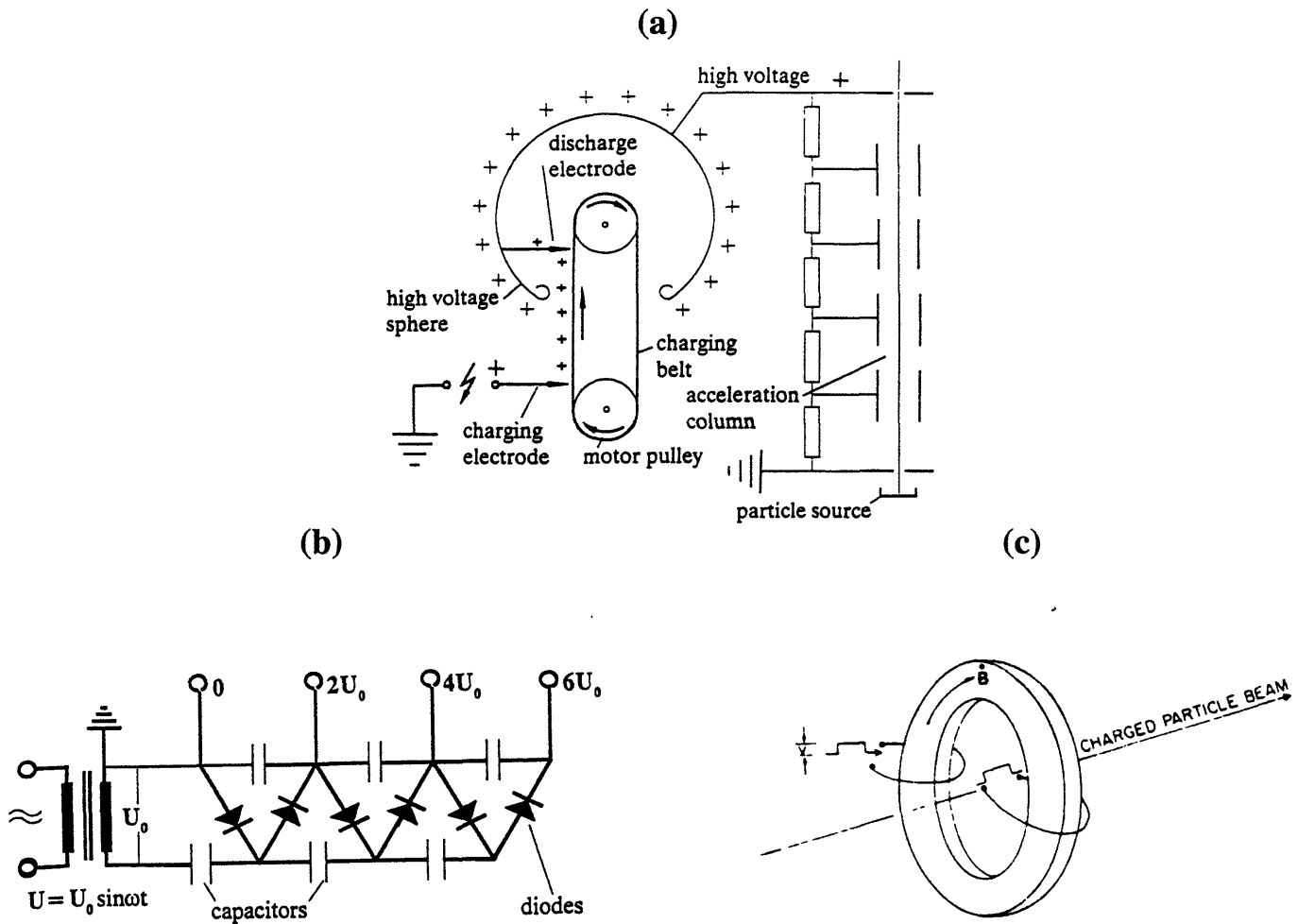


**Figure 2.8:** Several DC accelerators including: (a) Van de Graaff accelerator (b) cascade generator, (c) induction accelerator (53,55).

The primary disadvantage of DC accelerators is that the accelerating chamber holds the entire accelerating voltage. Thus, the insulating requirements for these chambers are the major limitation on the maximum voltage which can be applied, although they can still achieve potentials as high as 30 MeV; however, for particles with a charge of one, energies are limited to 30 MeV. This limitation is overcome by accelerators using radiofrequency EM fields.

### 2.3.1.2 Linear Radiofrequency Accelerators

Linear RF accelerators accelerate particles in a straight line through a chamber containing a number of EM field segments. These field segments are produced by electrodes and are separated by field gaps. Within the field segments a radiofrequency voltage is applied such that the particle is accelerated; the particle then drifts through a field gap (at constant velocity) to the next field segment where it is again accelerated. The length of the field gaps correspond with the oscillating EM field such that the particle only *feels* the accelerating electrical force of the bipolar EM field, i.e., the field gap length ( $L_n$  in Fig 2.9) increases with each acceleration to match the increased velocity of the particle, resulting in the particle reaching the next EM field just as the polarity of the field changes to create an accelerating force on the particle (Fig. 2.9).

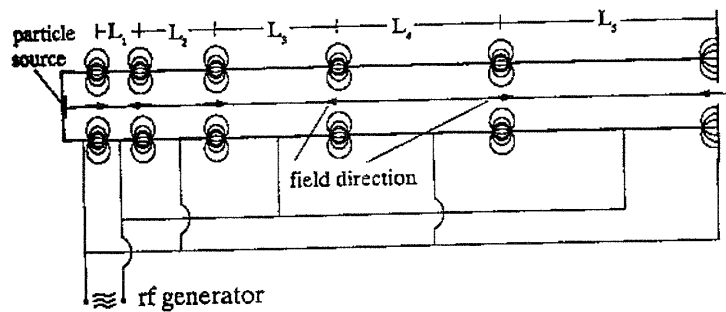


**Figure 2.9:** Schematic of a linear RF accelerator. The field gap distance,  $L_n$ , is the distance the particle travels at constant velocity before being accelerated again; with each acceleration the particle velocity increases, therefore, the length of  $L_n$  must also increase as the particle moves down the acceleration chamber (53).

Their primary disadvantage is the need for long acceleration chambers to reach high energies and the need for additional magnetic fields to focus the beam. The electron linear RF accelerator built at Stanford uses a chamber of 3200m to reach energies of 22 GeV.

### 2.3.1.3 Linear Radiofrequency Quadrupole Accelerators

RFQ accelerators were first proposed by Kapchinskii and Teplyakov in 1970 (60). These accelerators use radiofrequency EM fields to simultaneously focus, bunch, and accelerate the ion beam (55). One major advantage of RFQ accelerators is their ability to focus and bunch an ion beam at low energies, thereby capturing almost all ions extracted from the ion source at low voltage and accelerate them to an energy of 1-2 MeV in a very short distance (a few meters).

RFQs focus the ion beam with electromagnetic quadrupole fields uniformly distributed along the length of the beam channel. Figure 2.10 is a schematic showing the arrangement of a four-conducting-line electromagnetic focuser and modulated electrodes. Particles with off-axis trajectories experience a focusing force in one plane and defocusing force in the other on alternate RF half cycles, switching the focusing-defocusing planes with each half cycle. This results in a strongly focusing system that will transport an ion beam without acceleration.

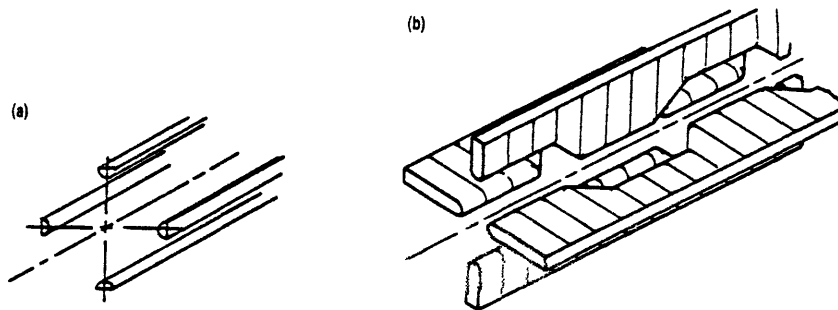


**Figure 2.10:** Schematic showing (a) the arrangement of four conducting line electromagnetic focuser, (b) modulated electrodes (55).

The ion beam is accelerated due to the mechanical perturbation on the four-line EM focuser. If the separation of electrodes of similar polarity varies periodically along the beam channel (Fig. 2.10b), a longitudinal accelerating field,  $E_z$ , results. The gap distance,  $D_{gap}$ , is a function of the particle velocity,  $v$ , and wavelength,  $\lambda$ , of the EM field:

$$D_{gap} = \frac{v\lambda}{2c} = \frac{\beta\lambda}{2} \quad (2.25)$$

where  $c$  is the speed of light and  $\beta=v/c$ .

Figure 2.11 is a schematic of a section of an RFQ resonator designed at Los Alamos. At any given time the voltage on adjacent pole tips is the same in magnitude but opposite in sign; after each half cycle these voltages reverse sign, thus producing a net quadrupole focusing force in the plane transverse to particle acceleration. The focusing force is spatially contiguous along the direction of acceleration.

If the pole tips have a constant radius, only a radial focusing force will be present and no acceleration will take place; however, if the pole-tip distance is modulated periodically, a longitudinal accelerating field is produced in addition to the transverse focusing field.

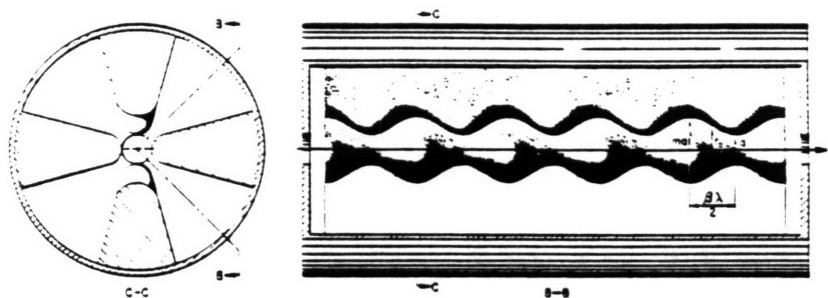


**Figure 2.11:** Schematic of a section of an RFQ resonator designed at Los Alamos. The figure on the right depicts the longitudinal accelerating field resulting from periodically modulating the pole-tip distance (55).

The focusing-accelerating quadrupole fields allow RFQs to capture and bunch a high percentage of the ions from the pre-accelerator ion source, resulting in small ion losses and high transmission efficiencies. The ions can be accelerated to high energies over short distances, and the RF amplitude of an RFQ accelerator is the only physical parameter to adjust during operation; thus, RFQs are smaller and relatively simple to operate compared to conventional linear accelerators (55). Disadvantages include 1) output-energy variation is less flexible than in DC accelerators, and 2) the total power efficiency is less than conventional linear accelerators above approximately 2 MeV (55). Figure 2.12 is a drawing of a RFQ with manifold, designed at Los Alamos.

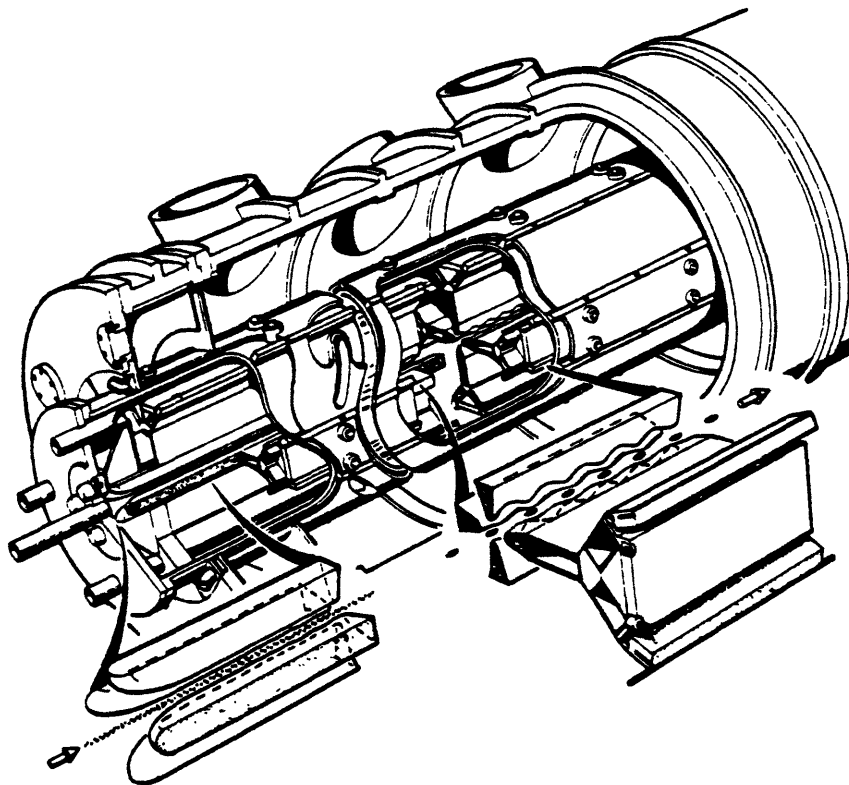


**Figure 2.12:** Drawing of an RFQ with manifold, designed at Los Alamos (55).



### **2.3.1.4 Circular Radiofrequency Accelerators**

Circular accelerators use magnetic fields to guide charged particles around a closed orbital trajectory. The acceleration is generally conducted in a circular cavity in which particles move in circular or gradually expanding orbits. Particles orbiting within the cavity periodically gain energy from an RF EM field. This configuration simplifies the RF system compared to linear RF accelerators, allowing protons and heavier ions to be accelerated to extremely high energies: the Fermi National Accelerator Lab (FNAL) accelerates protons up to 1000 GeV (61). The function of the magnetic field is only to guide the particles around a circular orbit. The RF field oscillations must be synchronized with the particle motion to achieve acceleration: the time for a particle to travel around one orbit must be an integer multiple of the RF field oscillation period. This synchronization depends on the particle velocity, path length, magnetic field strength, and frequency of EM field.

Although we will not use this type of accelerator for our neutron source, circular RF accelerators--specifically, cyclotrons--have the potential to provide industry with intense non-reactor neutron sources. Their usefulness seems limited to applications where a relatively high immobile neutron flux is needed; however, the neutron yields being reported and theorized (see Table 2.7) suggest they may be the accelerator of choice when mobility and portability are not the primary concern and nuclear reactors are impractical.

#### **2.3.1.4.1 Cyclotron Accelerators**

Cyclotrons use a uniform magnetic field and an RF cavity extending over the entire aperture of the magnet (Fig. 2.13). The accelerating cavity is cut in two halves with the accelerating fields generated between the two sections and the poles of the magnet. Thus, most of the particle's orbital path is without a tangential accelerating force. Cyclotrons accelerate particles in a nearly circular path that spirals outward. The ion path is curved using magnetic fields perpendicular to the particle's trajectory. As the particles gain energy their radius of curvature increases, since the

magnetic field is constant, and they spiral outward. The beam is extracted using magnetic fields to divert the particles from their near orbital path into a beam tube.

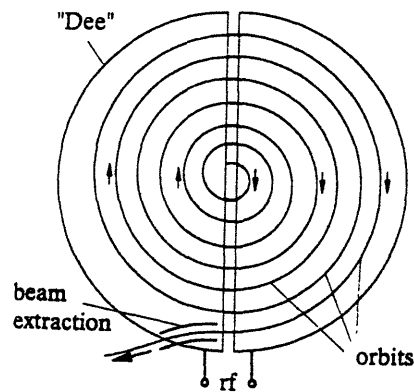
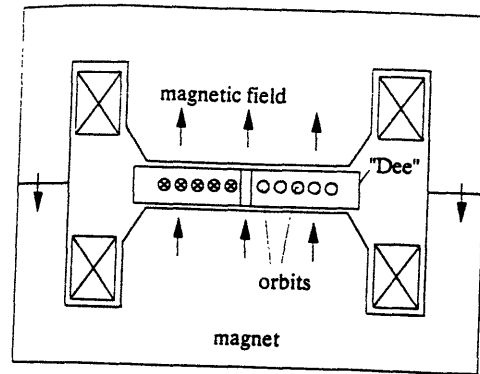


**Figure 2.13:** Schematic of a Cyclotron Accelerator. Cyclotrons use a uniform magnetic field and an RF cavity extending over the entire aperture of the magnet. The accelerating cavity is cut in two halves (called Dees) and the accelerating fields are generated between the two sections and the poles of the magnet. Particles are accelerated in a near circular path that spirals outward. The ion path is curved using magnetic fields perpendicular to the particle's trajectory. As the particles gain energy their radius of curvature increases, since the magnetic field is constant, and they spiral outward. The beam is extracted using magnetic fields to divert the particles from their orbital path into a beam tube (53).

The particles pass through the acceleration force twice per revolution. The revolution time,  $\tau$ , in a cyclotron is given by:

$$\tau = \frac{2\pi r}{v} = \frac{2\pi mc}{e} \frac{\gamma}{ZB} \quad (2.26)$$

where  $\gamma$  can be set to one for nonrelativistic particles,  $Z$  is the charge of the particle,  $e$  the electron charge,  $B$  the magnetic field,  $r$  the radius of orbit,  $m$  is particle mass, and  $v$  is velocity (53). If the magnetic field is constant the particles have constant revolution frequency, which then defines the appropriate EM frequency:

$$f_{rev} = f_{RF} = \frac{ZeB}{2\pi mc} = const \quad (2.27)$$

Equation 2.27 shows the EM frequency is dependent on charge,  $Z$ , and magnetic field strength,  $B$ , resulting in the following relations for protons, deuterons, and  $\alpha$ -particles:

$$\begin{aligned} f_{RF} \text{ (MHz)} &= 1.53 B \text{ (kG) protons} \\ &= 0.76 B \text{ (kG) deuterons} \\ &= 0.76 B \text{ (kG) } \alpha\text{-particles} \end{aligned}$$

Figure 2.14 is a plot of the necessary frequencies as a function of magnetic field strength for protons, deuterons, and  $\alpha$ -particles. The frequencies in Fig. 2.14 are actually the lowest possible frequencies for the given magnetic field strength: any odd integer multiple would also be acceptable (53).

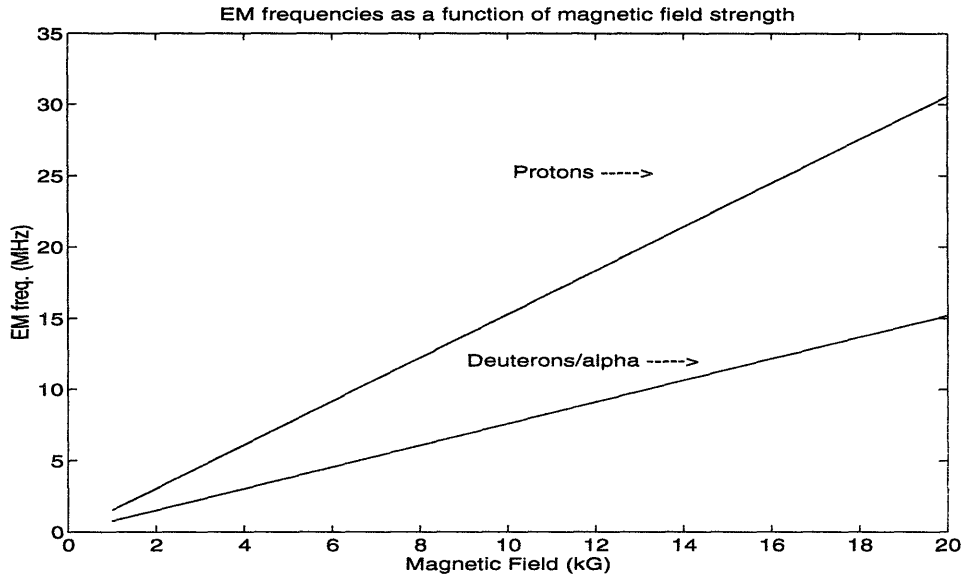


**Figure 2.14:** Cyclotron EM frequencies as a function of magnetic field strength for protons, deuterons, and  $\alpha$ -particles.

The maximum energy a particle can acquire in a cyclotron is a function of the particle mass, charge, magnetic field, and maximum orbital radius,  $R$ :

$$E_{max} = \frac{1}{2}mv^2 = \frac{(cp)^2}{2mc^2} = \frac{(ZeBR)^2}{2mc^2} \quad (2.28)$$

where  $p$  is momentum (53). Thus, for protons, deuterons, and  $\alpha$ -particles we have the following relations for  $E_{max}$ :

$$\begin{aligned} E_{max} (^1\text{H}) &= 0.48 B^2(\text{kG}^2) R^2(\text{m}^2) \\ E_{max} (^2\text{H}) &= 0.24 B^2(\text{kG}^2) R^2(\text{m}^2) \\ E_{max} (\alpha) &= 0.48 B^2(\text{kG}^2) R^2(\text{m}^2) \end{aligned}$$

Although cyclotrons are relatively compact, the need for strong magnetic fields excludes their use for applications needing a maneuverable neutron source. However, as stationary neutron sources, cyclotrons may be the best alternative to nuclear reactors, producing neutron fluxes

rivaling even high power reactors. Table 2.7 lists some of the characteristics of commercially available accelerators

**Table 2.7**  
**<sup>a</sup>Neutron Production From Commercially Available Accelerators.**

Model	Target Reaction	Incident Particle Energy (MeV)	Beam Current ( $\mu\text{A}$ )	Total Neutron Yield (n/s)	<sup>b</sup> Peak Thermal Flux ( $\text{n}/\text{cm}^2\text{-s}$ )
TN 46 Tube (Sodern)	T(d,n)	0.225	10,000	$4 \times 10^{11}$	$1.2 \times 10^9$
PI-4 Linac (Accsys)	Be(p,n)	3.9	1,000	$1.2 \times 10^{12}$	$2.6 \times 10^{10}$
Cyclotron 3D (IBA)	Be(d,n)	3.8	2,000	$5.7 \times 10^{12}$	$6.4 \times 10^{10}$
Cyclotron 3D-7P	Be(p,n)	7	2,000	$2.0 \times 10^{13}$	$3.3 \times 10^{11}$
Cyclotron 18/9	Be(p,n)	18	100	$1.0 \times 10^{13}$	$6.5 \times 10^{10}$
Cyclotron 18+	Be(p,n)	18	2,000	$2.1 \times 10^{14}$	fast n only
Cyclotron 30 (IBA)	Be(p,n)	30	400	$1.3 \times 10^{14}$	$6.11 \times 10^{11}$
Cyclotron 30	Be(p,n)	30	800	$2.6 \times 10^{14}$	$1.22 \times 10^{12}$
Cyclotron 140 (IBA)	Pb(p,n) <sup>238</sup> U fission	140 slow n	1,000	$6 \times 10^{15}$ ( $> 2 \times 10^{16}$ for k=5)	$5.0 \times 10^{13}$ $2.5 \times 10^{14}$
Rhodotron (IBA)	e <sup>-</sup> beam <sup>238</sup> U( $\gamma$ ,n)	15	10,000	$2.0 \times 10^{14}$	$2.4 \times 10^{12}$

<sup>a</sup> From Ref. 60.

<sup>b</sup> Thermal neutron flux suppose a point isotropic target in the center of a 20 cm radius H<sub>2</sub>O moderator.

## 2.4 Thermal Neutron Beam Production

Accelerator neutron sources produce fast neutrons with energies in the MeV range through nuclear reactions between the incident ion and target material. Since radiography is most efficient when using low energy (thermal) neutrons, the initial fast neutrons must be slowed down before interacting with the object to be imaged. This slowing down process is called moderation. Moderation of neutrons is accomplished by allowing them to collide with nuclei, thereby transferring some of their energy in the process. Since neutrons are not influenced by electrical fields, the extraction of a moderated thermal neutron beam must be passive, i.e., a port is constructed within the moderator allowing neutrons to enter and travel unobstructed to the imaged object. The objective is to maximize the thermal neutron flux emanating from the beam port.

It is possible to produce images using the fast neutrons emitted from the accelerator target, however, fast neutron interaction cross-sections are lower and do not differ as much among materials as for thermal neutrons, resulting in a decreased image resolution and converter screen sensitivity (see section 2.1.5). However, there are two advantages to using the fast neutrons from accelerators: 1) without the need for moderation, the usable flux is substantially higher, compensating somewhat for the smaller differential in cross-section among materials, and 2) since the transmittance for fast neutrons is higher than for thermal neutrons, fast neutrons may be better (or even necessary) for imaging very thick objects.

### 2.4.1 Neutron Moderation

Neutrons with energies less than 10 MeV are traveling at velocities less than 0.1 the speed of light and can be treated non-relativistically. Since our accelerator source produces neutrons in the range of 1-5 MeV, all theoretical development will be from a classical perspective. Thus, we have the following energy-velocity relation for non-relativistic neutrons:

$$E = \frac{1}{2}mv^2 \quad (2.29)$$

$$v = \sqrt{\frac{2E}{m}} \quad (2.30)$$

where  $E$  is kinetic energy,  $m$  is neutron mass, and  $v$  is velocity. Equations 2.29 and 2.30 show that a change in velocity is also a change in energy; thus, the slowing down process is an energy transfer from the neutron to the medium.

If a neutron with initial energy  $E$  and velocity  $v$  collides with an atom of mass  $A$  initially at rest, then, using conservation of energy and momentum, the ratio of the neutron energy after the collision,  $E'$ , and the initial energy,  $E$ , is:

$$\frac{E'}{E} = \frac{A^2 + 1 + 2A \cos \theta}{(A + 1)^2} \quad (2.31)$$

Where  $\theta$  is the scattering angle in the center of mass. When  $\theta = 0$  (no scattering) this ratio is 1; and when  $\theta = 180^\circ$  (maximum scattering), i.e., a head-on collision, Eq. 2.31 becomes:

$$\left[ \frac{E'}{E} \right]_{\theta = 180^\circ} = \left[ \frac{A - 1}{A + 1} \right]^2 \quad (2.32)$$

Equation 2.32 can be used to compare the efficiency of energy transfer between a neutron and nuclides with different mass. Figure 2.15 shows the maximum energy transfer ratio for elements with mass numbers 1 to 50 using Eq. 2.32. The conclusion from this analysis is that light elements are better at slowing down neutrons due to the larger energy transfer per collision. As a general rule this is true, however, when deciding on a moderator material one must also be aware of the possibility of neutron absorption, which will remove the neutron entirely.

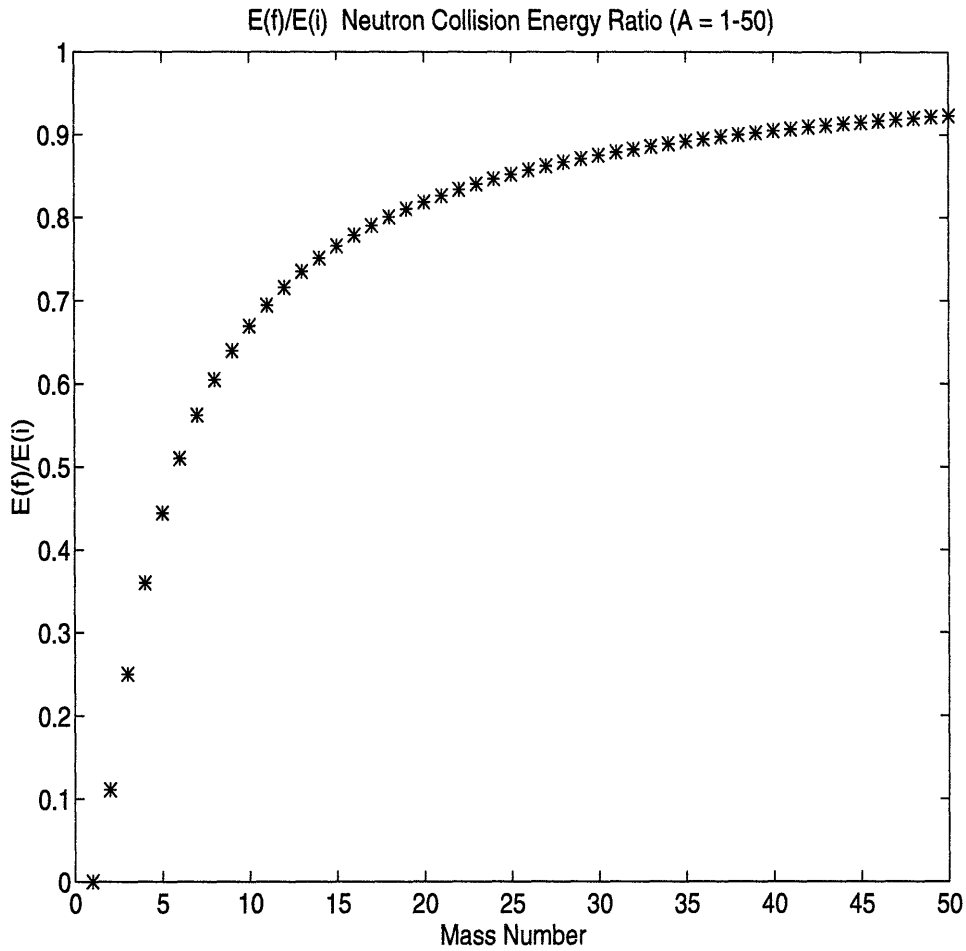


**Figure 2.15:** Maximum energy transfer ratio for elements with mass number 1-50 using Eq. 2.32. Light elements appear to be better at slowing down neutrons due to the larger energy transfer per collision.

Neutron scattering cross-sections are essentially independent of scattering angle for neutrons below 10 MeV; thus, the distribution of energy transfer ( $E'/E$ ) for one collision is uniform over the range  $(E'/E)_{\theta=180^\circ}$  to 1.0. If we consider many neutrons with the same initial energy, each subsequent collision also has a uniform energy transfer distribution; however, the neutrons are now themselves distributed in energy, which broadens the spectrum after the first collision (Fig. 2.16).



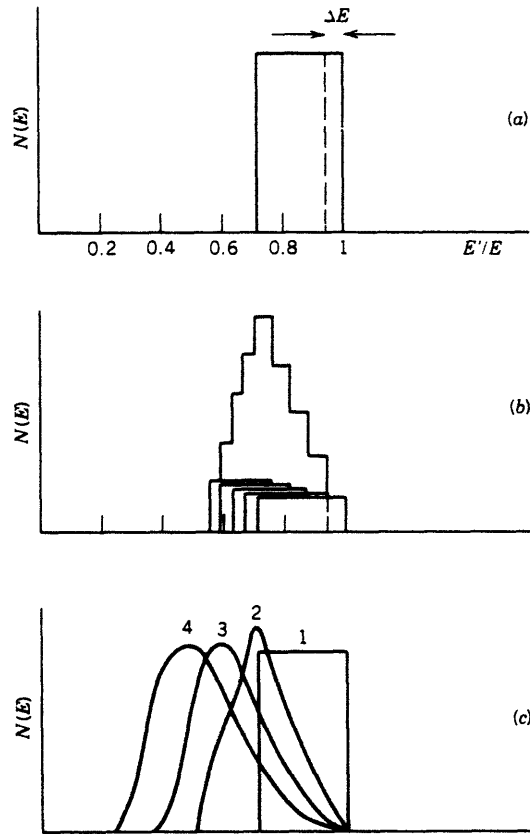


**Figure 2.16:** (a) After a single scattering from  $^{12}\text{C}$ , a monoenergetic beam of neutrons with initial energy  $E$  yields a flat distribution of energies  $E'$  from  $0.72E$  to  $E$ . (b) Dividing the scattered distribution into five narrow, nearly monoenergetic distributions of width  $\Delta E$ , we get after a second scattering the five flat distributions shown, whose sum is the peaked distribution. (c) An exact calculation of the energy distribution after 1, 2, 3, and 4 scatterings (62).

We can evaluate this quantitatively by defining a parameter  $\xi$  to be the average value of  $\ln(E/E')$  after each collision:

$$\xi = \left[ \ln \frac{E}{E'} \right]_{\text{avg}} = \frac{\int \ln \left[ \frac{(A+1)^2}{A^2 + 1 + 2A \cos \theta} \right] d\Omega}{\int d\Omega} \quad (2.33)$$

where  $d\Omega$  is the solid angle in the center of mass, and scattering is assumed to be isotropic.

Integrating (2.33) gives:

$$\xi = 1 + \frac{(A-1)^2}{2A} \ln \left[ \frac{A-1}{A+1} \right] \quad (2.34)$$

The average value of  $\ln E'$  is decreased by each collision an amount  $\xi$ , and after  $n$  collisions is  $\ln E'_n$ :

$$\ln E'_n = \ln E - n\xi \quad (2.35)$$

Figure 2.17a is a plot of  $\xi$  for target nuclides with mass numbers from 1 to 50. Figure 2.17b shows the number of collisions needed to reduce the average neutron energy from 5 MeV to a thermal energy of 0.025 eV for target nuclides with mass numbers from 1 to 50.

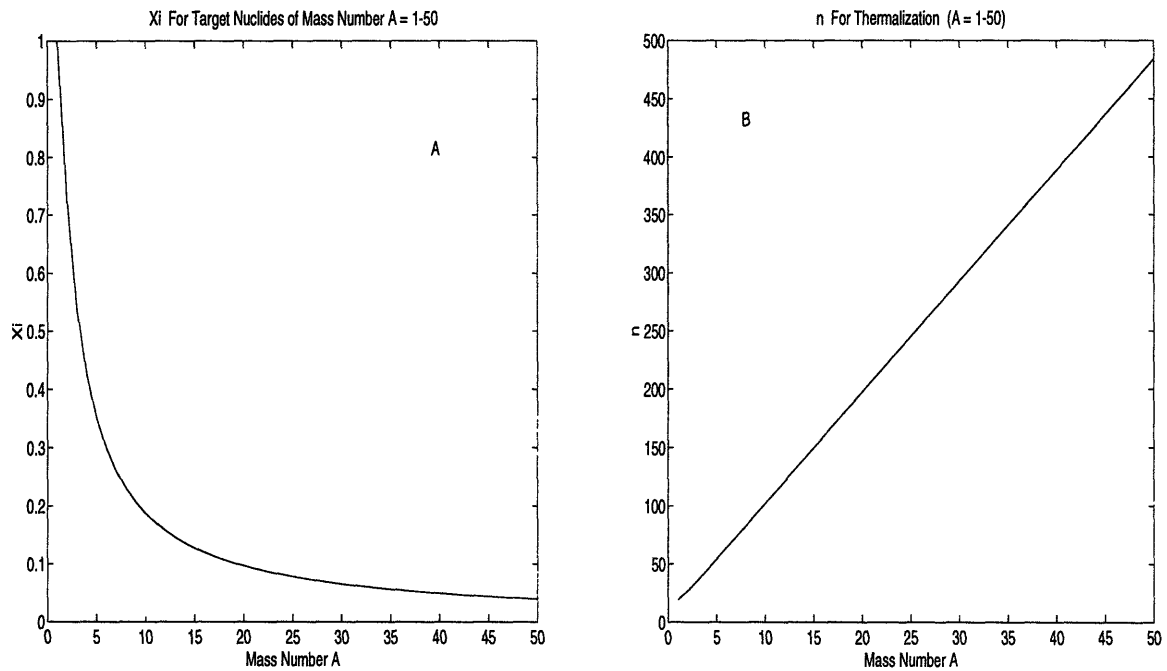


**Figure 2.17:** (A)  $\xi$  for target nuclides with mass numbers from 1 to 50. (B) The number of collisions,  $n$ , needed to reduce the average neutron energy from 5 MeV to a thermal energy of 0.025 eV for target nuclides with mass numbers from 1 to 50.

Equations 2.33-2.35 assume the target nuclide is at rest; although this assumption is valid for high energy neutrons in the MeV range, as neutrons approach energies equal to the thermal motions of the moderating atoms ( $E_{\text{therm}} = kT$ ) they will reach thermal equilibrium with the moderator. At thermal equilibrium, the energy distribution of the neutrons is best described by a Maxwell distribution:

$$f(E) = \frac{2\pi n}{(\pi kT)^{3/2}} E^{1/2} e^{-\frac{E}{kT}} \quad (2.36)$$

where  $n$  is the neutron density,  $T$  is the temperature of the moderator,  $E$  is the neutron energy, and  $k$  is the Boltzmann constant. Figure 2.18 illustrates three idealized thermalization distributions for moderator temperatures of 100, 200, and 300° K. It is important to notice the distribution becomes more sharply peaked as the temperature decreases, and to bear this in mind when considering materials, densities, and temperature parameters for a moderator.

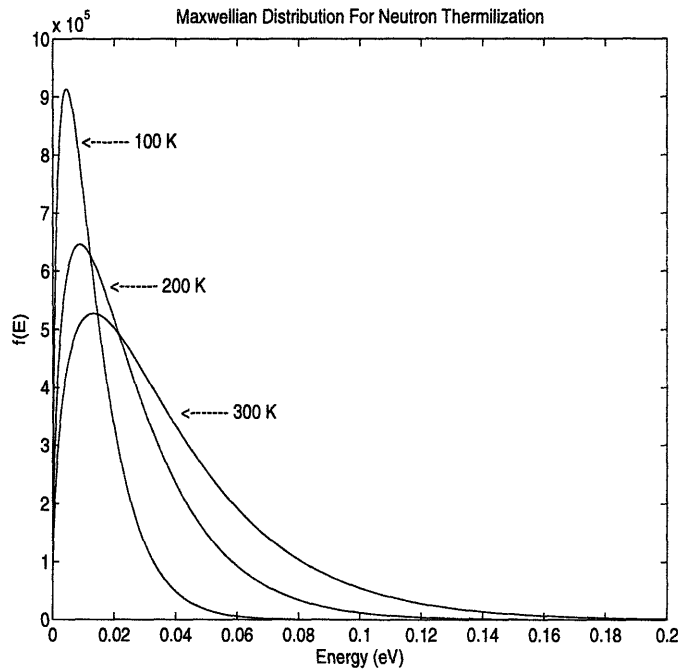


**Figure 2.18:** Neutron thermalization distributions for moderator temperatures of 100, 200, and 300° K.

## 2.4.2 Beam Divergence and L/D Ratio

Ideal conditions for parallel-beam radiography and tomography is for the radiation beam to be absolutely parallel, and orthogonal to the radiographic image plane. However, in practice, the beam will have some degree of divergence. Beam divergence is typically defined by the L/D ratio, where L is the length and D the diameter of a collimator:

$$R_{\theta} = \frac{L}{D} \quad (2.37)$$

which relates to the angle of divergence by:

$$\theta \cong \frac{1}{R_{\theta}} \quad (2.38)$$

becoming exact in the limit of large L (63). Reactor neutron beam ports often yield thermal neutron beams with  $L/D > 100$ .

## 2.5 MIT-NCT System

### 2.5.1 Accelerator System

An AccSys Technology model DL-1 RFQ accelerator will be used. This accelerator is a compact RFQ ion accelerator which produces 0.9 MeV deuterons directed onto a beryllium target. Neutrons with energies ranging from 1 to 5 MeV are produced by a  ${}^9\text{Be}(d,n){}^{10}\text{B}$  reaction. These fast neutrons will be thermalized by a moderator assembly to produce thermal neutrons for imaging. Table 2.8 list the operating parameters for this accelerator.

The system consists of three main components: 1) the RFQ accelerator with ion source, 2) the RF power amplifiers, and 3) the ion source power supply and control system. Figure 2.19 shows the accelerator system prior to shipment to MIT.

**Table 2.8**  
**RFQ Accelerator Operating Parameters**

Accelerated Particle	deuteron
Beam Energy (nominal, MeV)	0.9
Neutron Yield (n/s/mA)	$7.8 \times 10^7$
Beam Current/Pulse (mA)	10
Beam Pulse Width (msec)	30-120
Pulse Repetition Rate (Hz)	1-120
Maximum Target Current (mA)	140
Maximum Target Yield (n/s/ $4\pi$ )	$1 \times 10^{10}$
Accelerator Length (ft)	4.0
Accelerator weight (lb)	400
Electrical Requirement (kVA)	12
Pulsed RF Power (kW)	40

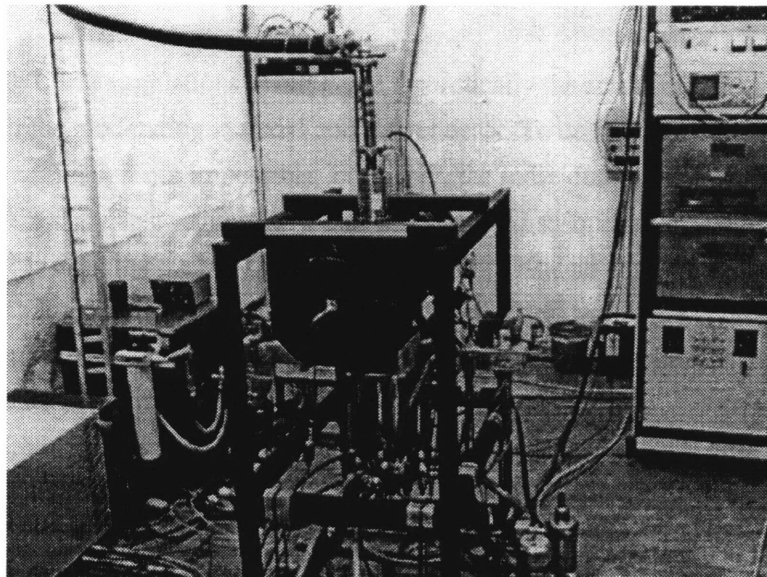


**Figure 2.19:** AccSys Technology model DL-1 RFQ accelerator prior to shipment to MIT. The RFQ is in the center; RF amplifier cabinet on the left rear; and ion source power supply and controls on the right.

## 2.5.2 Camera System

The camera system consists of a scintillation-converter screen, mirror, lens, CCD device, CCD controller, and computer. Figure 2.20 shows a schematic of the camera system.

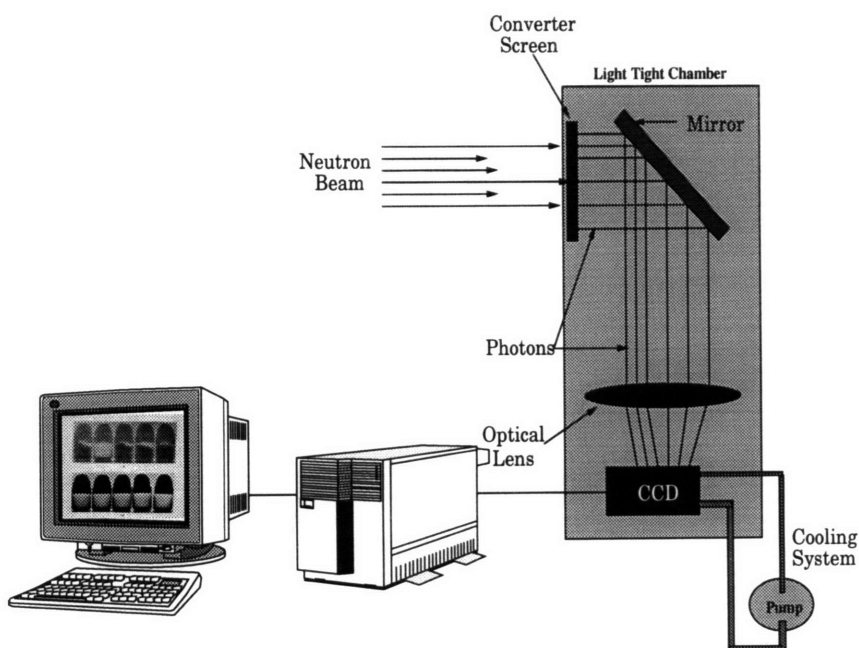


**Figure 2.20:** Schematic of the camera system.

The scintillation-converter screen is a Nuclear Enterprises NE-426 consisting of  ${}^6\text{LiF}$  powder mixed with  $\text{ZnS}(\text{Cu})$ , with dimensions of 180 x 240 mm. The screen uses a Cu scintillation activator rather than the standard Ag activator. This shifts the wavelength spectrum of the light emission toward the red region where the quantum efficiency is higher (see Fig. 2.5). The scintillator light emission is reflected by a front surface mirror and focused onto a CCD detector by either of two lenses: 1) a Nikon 50mm F/1.2 lens, or 2) a Perkin-Elmer 100mm F/0.95 lens. The CCD camera is a Princeton Instrument TE/CCD-1242E which uses an EEV 05-30 CCD array of

1152 x 1242 pixels (26 x 28 mm) with pixel dimensions of 22.5 x 22.5  $\mu\text{m}$ . The camera is interfaced with a Princeton Instruments ST-138 controller which can read out at two speeds (12 bits, 1MHz; 15 bits, 430 kHz). The controller also controls the thermoelectric cooling of the CCD. The CCD has a flow chamber for additional cooling and a lower limit rating of  $-70^\circ\text{C}$  using methanol as a coolant ( $-54^\circ\text{C}$  has been achieved using water cooling). The dark current decreases by a factor of 2 for each decrease in temperature of  $\sim 7^\circ\text{C}$ . The controller is also interfaced with a computer which can store the data array information, and has software to control certain camera parameters (52).

## 2.6 Summary

From both a theoretical and engineering perspective, accelerator based thermal neutron imaging systems are complex; it is beyond the scope of this thesis to thoroughly describe all aspects these systems. This chapter attempts to introduce the reader to the basic theory and engineering involved in the major components of accelerator based thermal neutron imaging systems utilizing electro-optic CCD image detection, such that the reader has an understanding of the basic engineering and theoretical basis of the imaging system to be used at MIT, and the motivation for its development. An important aspect for all neutron imaging systems utilizing a fast neutron source is the moderation of fast neutrons emitted by the source. The following chapters describe our effort in designing a moderator assembly which yields a thermal neutron beam with both a large cross-sectional area and a high, spatially uniform, flux. The following chapter discusses the methodology of our work.

# Chapter 3

## Methods

The objective of this work was to design a neutron moderator which produces a high thermal neutron flux with a uniform flux distribution over a large area, using an accelerator based neutron source. Specifically, the objective was to produce a uniform thermal beam with an area greater than our scintillating converter screen, which has dimensions of 18 x 24 cm (432 cm<sup>2</sup>). Moderator designs producing a cylindrical thermal beam with a cross-sectional area of 491 cm<sup>2</sup> (12.5 cm radius) were analyzed theoretically using a Monte Carlo Neutron-Particle Transport Simulation (MCNP) code from Los Alamos National Laboratory (18). The neutron energy and angular distribution for a 0.9 MeV <sup>9</sup>Be(d,n)<sup>10</sup>B reaction previously modeled (19) was analyzed and used for all simulations. A moderator material was chosen after analyzing the moderating characteristics of several materials. The assessment of each moderator design was based on the magnitude and uniformity of the thermal beam flux. Geometric variables unique to each design were altered in an attempt to find the optimum configuration. For additional comparison, thermal beam flux for the best designs were evaluated for ranges of L/D ratio. For relative comparison of all designs, simulations were run with 5 x 10<sup>4</sup> particles; for L/D ratio evaluation of the best designs, simulations were run with 5 x 10<sup>5</sup> particles to improve the simulation statistical error.



## 3.1 Monte Carlo Computer Code

MCNP is a general-purpose Monte Carlo code that can be used for neutron, photon, electron, or coupled neutron/photon/electron transport. Pointwise cross-section data are used for all particle interactions. The code accounts for incoherent and coherent neutron scattering, fluorescent emission after photoelectric absorption of photons, and bremsstrahlung radiation. MCNP allows the user to define the energy and angular distribution of the source, allowing us to use a simulated neutron emission spectrum for a  ${}^9\text{Be}(d,n){}^{10}\text{B}$  reaction.

Monte Carlo simulations were used to duplicate theoretically the statistical process of the neutrons interacting with both the moderating material and the reflector. To do this using deterministic methods becomes extremely complex if not impossible. In MCNP, the individual probabilistic events that comprise a process are simulated sequentially. The probability distributions governing these events are statistically sampled to describe the total phenomenon. The statistical sampling process is based on the selection of random numbers. In particle transport, the Monte Carlo technique is a theoretical experiment, consisting of actually following each of many particles from a source throughout its life to its death in some terminal category (absorption, annihilation, escape, etc.). Probability distributions are randomly sampled to determine the outcome at each step of its life. Tallies can be requested that give, as in our case, flux across certain surfaces for certain energies (18).

MCNP tallies include a relative error,  $R$ , defined as one estimated standard deviation from the mean, divided by the mean. This error can be used to assess the precision of the simulation by using it to form confidence intervals about the estimated mean,  $\chi$ : there is a 68% and 95% chance the true result of the simulation (not the physical reality) will be in the range of  $\chi(1 \pm R)$  and  $\chi(1 \pm 2R)$  respectively (18). In essence, the relative error reported with each tally entry is an indicator of the quality of the tally entry. Table 3.1 lists the guidelines suggested in the MCNP manual (18) for interpreting the MCNP error.

**Table 3.1**  
**Suggested Guidelines For Interpreting MCNP Error**

Range of the Relative Error	Quality of the Tally
0.5-1.0	Garbage
0.2-0.5	Factor of a Few
0.1-0.2	Questionable
< 0.1	Generally Reliable

To run an MCNP simulation the user creates an input file which defines 1) the geometry of the assembly to be analyzed, 2) parameters of the materials comprising the geometric assembly, including density, molecular structure, and temperature, 3) the intensity and energy/angular distribution of the source, and 4) the desired tallies, including, among others, flux and fluence across surfaces of the geometric structure. This file is then read by the MCNP executable program when the simulation is run. When an interaction between a particle and an atom or nuclide of the material occurs, the program references a file containing interaction cross-sections; the cross-section used for an interaction is dependent on 1) the type of particle, 2) the particle energy, 3) the atom or nuclide the particle is interacting with, and 4) the temperature of the material which the atom or nuclide comprise. For materials with particularly well characterized interaction cross-sections, there are material codes which can be entered in the input file in addition to the molecular structure of the material comprising the geometric assembly: H<sub>2</sub>O, D<sub>2</sub>O, and polyethylene are among those materials having material codes.

## 3.2 Moderator Materials and Simulation Parameters

Nuclear reactor engineering and reactor based neutron radiography systems have provided a great deal of information concerning neutron moderation (20,21). It has been found that H<sub>2</sub>O, D<sub>2</sub>O, and polyethylene are among the best moderating materials, due to their high hydrogen content. Therefore, moderator analysis was limited to these three materials. Reactor engineering has also shown that surrounding the moderator with a reflector, i.e., a material having large scattering cross-sections for fast neutrons, can increase the thermal neutron yield within a moderator by deflecting fast neutrons back into the moderating material (20,21). Beryllium has been found to be one of the best reflectors (21), therefore, the ability of Be to increase thermal flux was evaluated. Table 3.1 lists the material parameters used in the simulations.

**Table 3.2**  
**MCNP Parameters of Moderator/Reflector Material**

Material	Density (g/cm <sup>3</sup> )	Temperature (°K)
<sup>a</sup> H <sub>2</sub> O	1.0	300
<sup>ab</sup> D <sub>2</sub> O	1.0	300
<sup>a</sup> CH <sub>2</sub> (polyethylene)	0.925	300
Be	1.85	300

<sup>a</sup> Material code for 300° K used.

<sup>b</sup> The actual density of pure D<sub>2</sub>O is 1.1 gm/cm<sup>3</sup>

## 3.3 Thermal Beam Flux Assessment

All moderator designs produced a cylindrical thermal neutron beam. In this analysis, thermal neutron energy is defined to include all neutrons with energy less than 0.1 eV. Thermal beam flux was assessed for all designs by measuring the thermal flux over a 12.5 cm radius circular surface of the moderator, a given distance from the source. For all but one design this surface was 10 cm from the source. For some designs this surface was not actually the surface of the moderating material but a circular area in the empty beam port, defined in the MCNP simulation as a surface to produce a flux tally.

### 3.3.1 Spatial Uniformity

To assess the thermal neutron flux uniformity the circular surface of the thermal beam used for the flux tally was divided into 13 concentric sections (Fig. 3.1). For each section, the MCNP code produced a flux tally and a relative error indicating the simulation's statistical precision. The results of the flux measurements are presented graphically in chapter 4 for each moderator design by plotting the magnitude of the flux as a function of distance from the center of the beam. Each point in these plots represents the average thermal flux across the circular segment of the beam bounded by the circumference of two circles differing in radius by 1 cm (see Fig. 3.1). Thirteen circular segments 1 cm thick (except for the last segment which was 0.5 cm thick) spanned the 12.5 cm beam port. Therefore, each point in these plots represents the average flux at the approximate radial distance from the center of the beam given for that point.

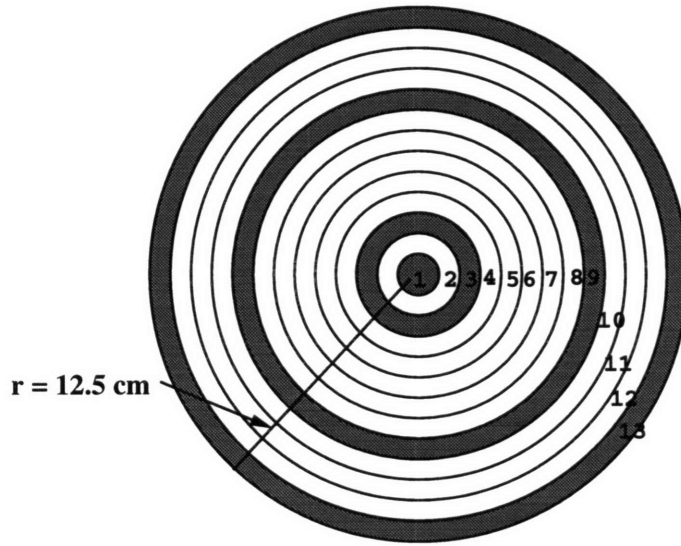


**Figure 3.1:** Flux uniformity assessment geometry. Each moderator produced a 12.5 cm radius cylindrical thermal beam. The circular surface used for the flux tally was segmented into 13 sections. Each section was 1 cm thick except for the outer most segment which was 0.5 cm thick. The shaded segments represent the points on the flux distribution plots denoted as 1, 3, 9, and 13 cm.

### 3.3.2 Thermal Beam Flux Statistics

In addition to presenting the thermal beam flux distribution graphically, flux statistics are also presented in chapter 4. The sample mean, sample standard deviation, coefficient of variation, and mean MCNP error were calculated from the flux distribution data for each moderator design. The sample mean,  $\bar{\chi}$ , and sample standard deviation,  $s$ , were calculated using the following equations:

$$\bar{\chi} = \frac{\sum \chi_i}{n} \quad (3.1)$$

$$s = \sqrt{\frac{\sum (\chi_i - \bar{\chi})^2}{n - 1}} \quad (3.2)$$

where  $\chi_i$  is the value of each sample (e.g., the flux at a given distance from the center of the beam, or the MCNP error for the flux measurement at a given distance from the center of the beam), and  $n$  is the number of samples.

The thermal beam flux distribution coefficient of variation (COV) for each design is used as a quantitative measure of flux spatial uniformity:

$$COV = \frac{s}{\bar{\chi}} \quad (3.3)$$

### 3.4 Summary

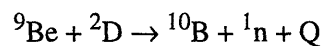
MCNP simulations were used to evaluate several materials for their ability to thermalize neutrons, and to assess the magnitude and spatial uniformity of the thermal neutron beam for different moderator designs. Materials included H<sub>2</sub>O, D<sub>2</sub>O, Be, and polyethylene. Quantitative comparisons of thermal beam flux uniformity for the different moderator designs was accomplished by segmenting the thermal beam cross-sectional area and calculating a flux coefficient of variation (COV) for each design; evaluation of the magnitude of thermal flux for each design was achieved by calculating the mean flux across the segmented beam. Chapter 4 presents the results of these simulations.

# Chapter 4

## Results and Discussion

### 4.1 Energy and Angular Distribution for a 0.9 MeV ${}^9\text{Be}(d,n){}^{10}\text{B}$ Reaction

Neutrons will be produced from a RFQ linear accelerator by accelerating deuterons to an energy of 0.9 MeV and directing them onto a  ${}^9\text{Be}$  target:



The reaction transforms  ${}^9\text{Be}$  to  ${}^{10}\text{B}$  with the emission of a neutron and an energy release of  $Q$ . However, the energy spectrum is quite complex for this incident deuteron energy. For deuterons above a few MeV, neutrons are produced primarily from deuteron stripping; and for low incident energies neutrons are produced primarily from compound nucleus formation and decay. However, at energies around 1.0 MeV, both compound nucleus formation and stripping occur (64).

Even if compound nucleus formation predominated, there are five well known excitation states of  ${}^{10}\text{B}$  in addition to the 4.35 MeV to ground reaction: 0.72, 1.74, 2.15, and 3.58 MeV (64). Additionally, there is evidence to suggest an excitation state at 2.9 MeV, and that this state may actually be two states at 2.75 and 3.17 MeV (65). With the additional possibility of neutron

stripping, it is not surprising that the  ${}^9\text{Be}(d,n){}^{10}\text{B}$  energy spectrum for deuterons in the range of 1 MeV is a near continuous spectrum from 1-5 MeV (Fig. 4.1).

The MCNP simulations presented here use a neutron source energy and angular distribution modeled by (19) for 0.9 MeV deuterons incident on a  ${}^9\text{Be}$  target with a neutron intensity of  $10^{10}$  n/s/ $4\pi$ . Figure 4.2 shows the neutron energy distribution of the source. Figure 4.3a shows an angular distribution for neutrons of all energies. Figure 4.3 was obtained by placing the source at the center of a 10 cm radius sphere and measuring the average flux (n/cm<sup>2</sup>-s) across sections of the spherical surface (Fig. 4.3b). Appendix III contains a series of figures similar to 4.3a showing this angular distribution for 0.2 MeV energy bins spanning the range of the neutron source energy distribution.

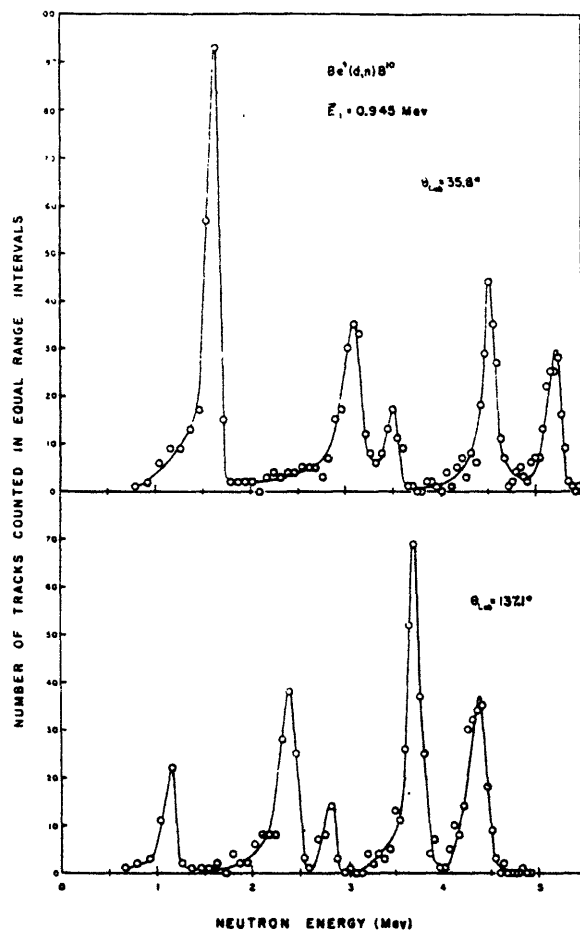


**Figure 4.1:** Neutron energy spectra for  ${}^9\text{Be}(d,n){}^{10}\text{B}$  reaction using 0.945 MeV deuterons for lab frame angles of  $35.8^\circ$  and  $137.1^\circ$  (64).



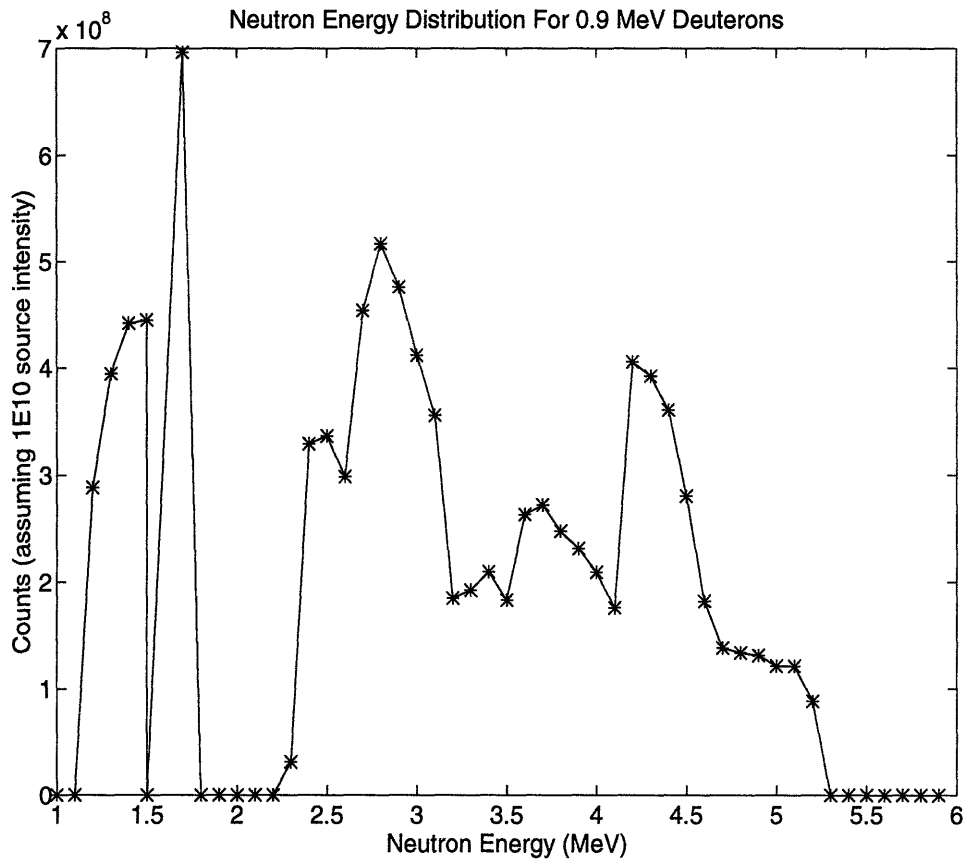


**Figure 4.2:** Accelerator neutron source energy distribution modeled by (65) for 0.9 MeV deuterons incident on a  $^9\text{Be}$  target, assuming  $10^{10}$  source intensity.

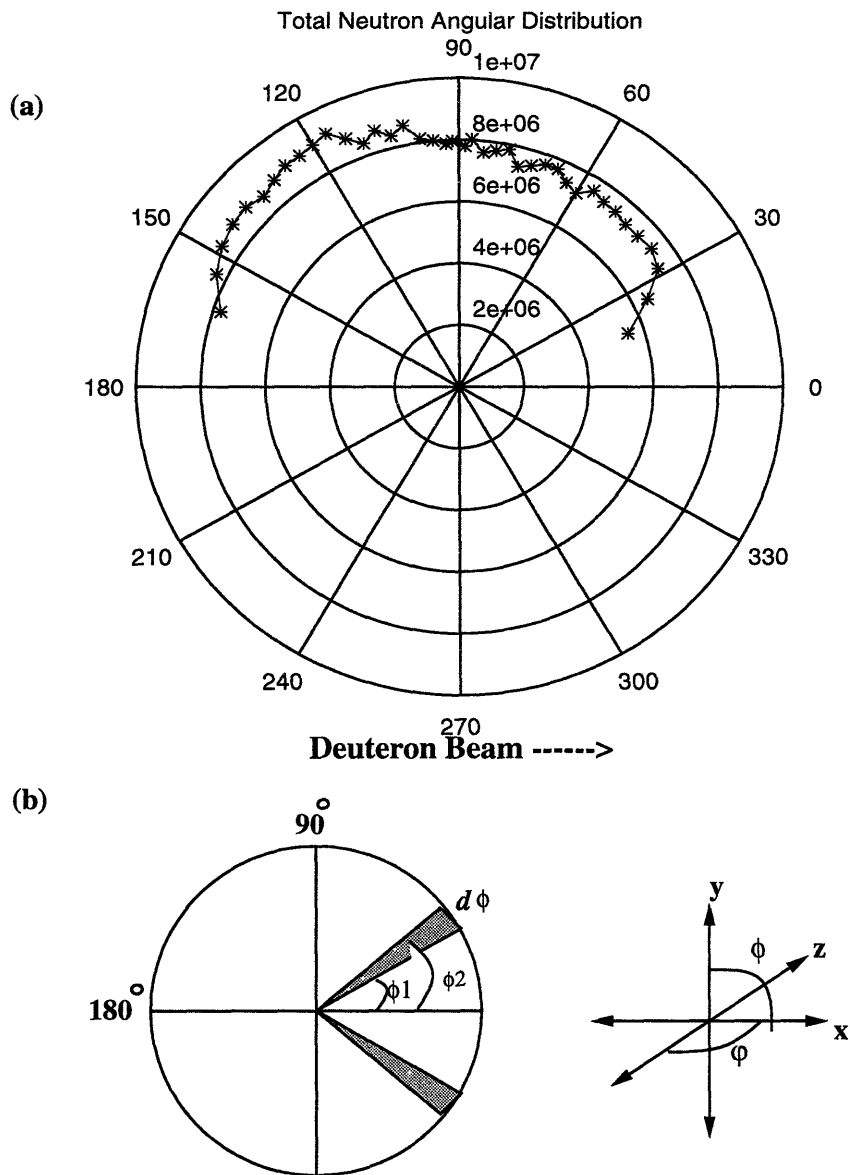


**Figure 4.3:** (a) Angular flux distribution for neutrons of all energies, obtained by placing the source at the center of a 10 cm radius sphere and measuring the average flux ( $\text{n}/\text{cm}^2\text{-s}$ ) over sections of the sphere. (b) Each point in (a) denotes the average flux across a section of the spherical surface defined by the surface  $2\pi\sin\phi d\phi$ , symmetric about  $\phi$ . (Source intensity was  $10^{10}$  n/s).

## 4.2 Moderator Thermal Neutron Flux Density

When designing a neutron moderator it is important to understand the neutron thermalization characteristics of potential moderating materials. A particular concern for our tomography system arises from the desire to image relatively large objects using a scintillator screen with an area of  $432 \text{ cm}^2$ . To create meaningful radiographs of this size we will need a thermal neutron beam with at least this cross sectional area with a uniform distribution of thermal neutrons. Therefore, an important moderating characteristic is the distribution of thermal neutrons within the moderator. This analysis also allowed us to evaluate the effect on the thermal distribution from the backward biased distribution of the accelerator neutron source (see Fig. 4.3a).

Thermal neutron flux densities for polyethylene,  $\text{H}_2\text{O}$ , and  $\text{D}_2\text{O}$  were investigated with and without a solid Be reflector. Flux densities were investigated using MCNP simulations, modeling a spherical moderator (20 cm radius) with the accelerator source distribution and intensity modeled as a point source at the center of the sphere. Thermal neutron flux density was estimated across the surface of concentric spherical regions within the 20 cm sphere with radii ranging from 1-20 cm and 1-10 cm for the non-reflector and reflector models (Fig. 4.4). The term *flux density* is used because neutrons can potentially cross a tally surface multiple times during the simulation, thereby incrementing the same flux tally multiple times. To determine if the nonuniformity of the source distribution affects the thermal neutron distribution, each sphere was divided into two hemispheres, representing the backward and forward directions with respect to the deuteron beam; thus, two flux tallies were recorded for each spherical surface.

For all analyses presented, thermal neutrons are defined as neutrons having energy less than 0.1 eV. Defining the thermal energy range in this way allows for the possibility of cold neutrons contributing to the thermal neutron count; however, since all moderator materials were simulated at 300 °K, the contribution from cold neutrons is minimal.

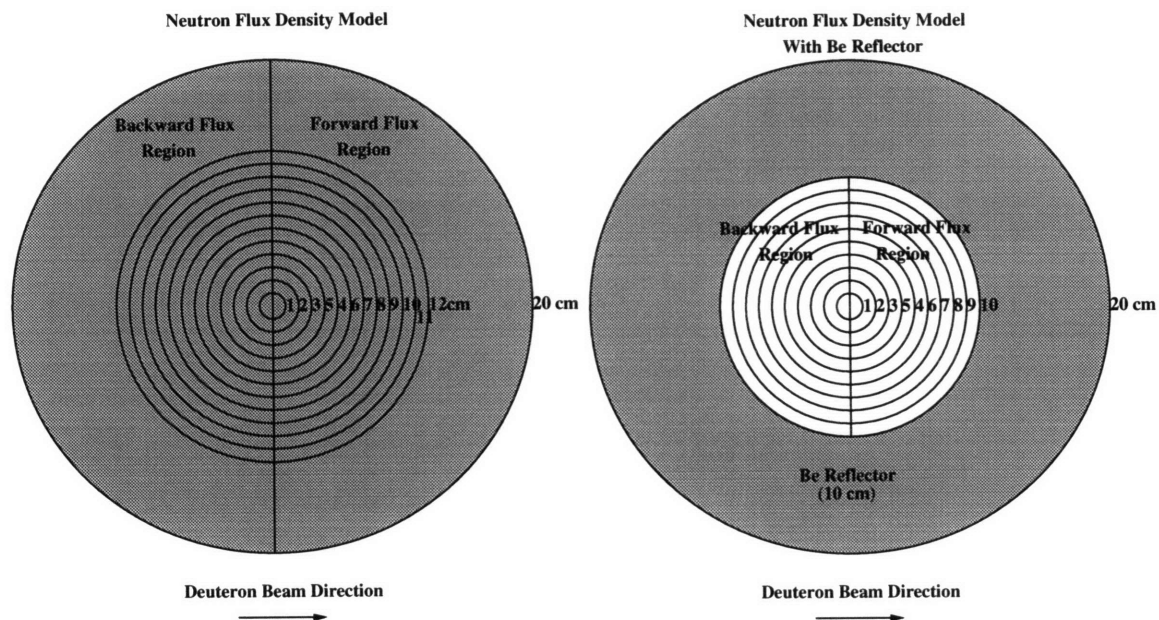


**Figure 4.4:** Thermal Neutron Flux Density Moderator/Reflector Model. Flux densities were investigated using MCNP simulations, modeling a spherical moderator with the accelerator source distribution and intensity modeled as a point source at the center of the sphere. Thermal neutron flux density was estimated across the surface of concentric spherical regions within the 20 cm radius sphere with radii ranging from 1-20 cm and 1-10 cm for the non-reflector and reflector models. To determine if the nonuniformity of the source distribution affects the thermal neutron distribution, each sphere was divided into two hemispheres, representing the backward direction and forward direction with respect to the deuteron beam.

Figures 4.5 and 4.6 show the flux density energy distribution within a sphere of polyethylene without a Be reflector. Similar plots for H<sub>2</sub>O, D<sub>2</sub>O, H<sub>2</sub>O + Be reflector, D<sub>2</sub>O + Be reflector, and polyethylene + Be reflector can be found in Appendix IV. Figure 4.7 shows the total thermal flux density as a function of distance from the source (center of sphere) for the moderating materials with and without a Be reflector.

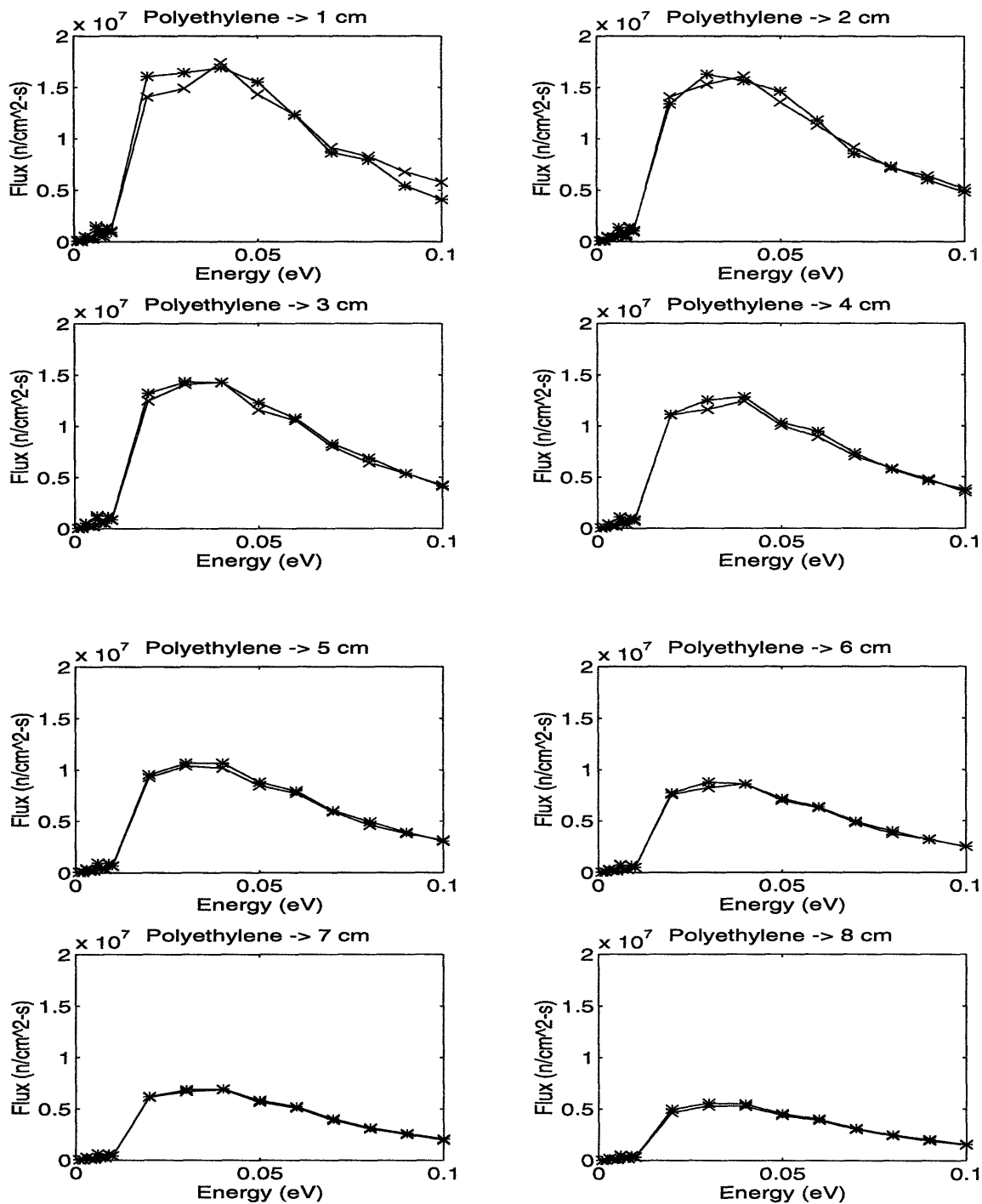


**Figure 4.5:** Thermal neutron flux density for polyethylene (1-8 cm from source). (\*)Backward hemisphere, (x) Forward hemisphere.

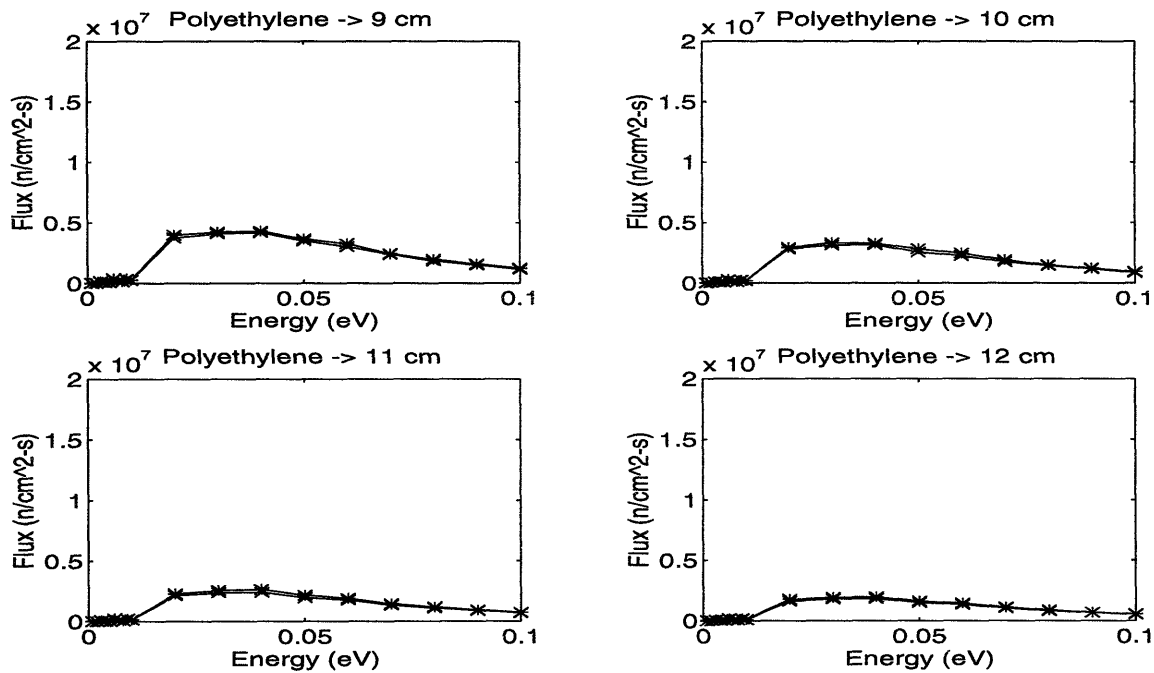


**Figure 4.6:** Thermal neutron flux density for polyethylene (9-12 cm from source).  
 (\*) Backward hemisphere, (x) Forward hemisphere.

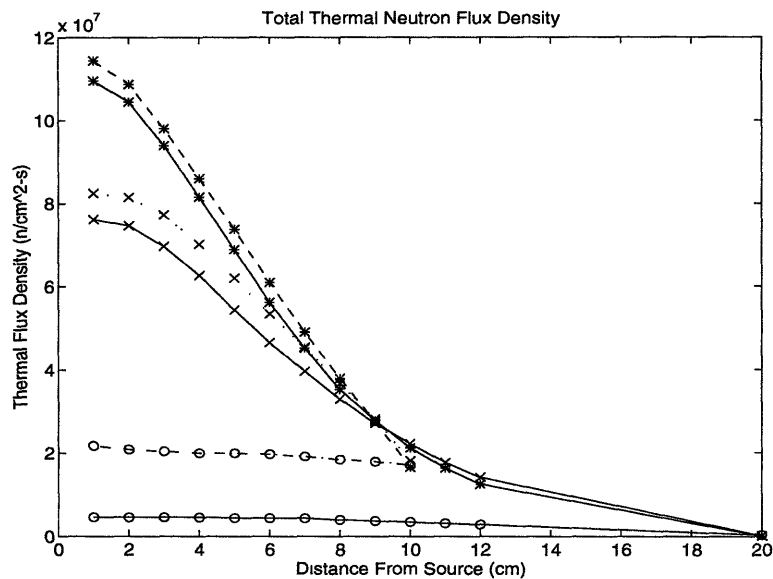


**Figure 4.7:** Total thermal neutron flux density as a function of distance from source. (\*, solid) polyethylene; (\*, dashed) polyethylene with Be reflector; (x, solid) H<sub>2</sub>O; (x, dotted) H<sub>2</sub>O with Be reflector; (o, solid) D<sub>2</sub>O; (o, dot-dash) D<sub>2</sub>O with Be reflector. Total flux was calculated for each distance by summing the fluxes for neutrons with energies  $\leq 0.1$  eV, and averaging the total flux for the two hemispheres.

## 4.3 Moderator Design

### 4.3.1 Moderator Material Assessment

Figures 4.5-4.7 and figures in Appendix IV, lead to the following conclusions:

- Although the accelerator source fast neutron spatial distribution is biased in the backward direction, neutron interactions within the material resulting in thermalization eradicate directional bias of thermal neutrons.
- Polyethylene yields the highest thermal neutron flux density for distances of 1-10 cm from the source; H<sub>2</sub>O yields the second highest flux density over this distance; and D<sub>2</sub>O yields the lowest flux density.
- At a distance of 10 cm from the source, all moderating materials yield essentially the same thermal neutron flux density.
- Although polyethylene and H<sub>2</sub>O result in relatively high thermal densities close to the source, both show a rapid decrease in thermal density with distance from the source.
- The most uniform density distribution within the sphere was produced by D<sub>2</sub>O.
- A 10 cm Be reflector surrounding the moderator material increased thermal flux density for all materials. The largest increase was for D<sub>2</sub>O. The increase in flux density for H<sub>2</sub>O and polyethylene was relatively small.
- The Be reflector did not significantly alter the rate of decrease in flux density with distance from the source for any material.
- To utilize the high flux density of polyethylene and H<sub>2</sub>O near the source, the opening to the beam port should be as close as possible to the source and should displace as little moderator material as possible. However, the need for a large beam cross-sectional area will necessitate a compromise.

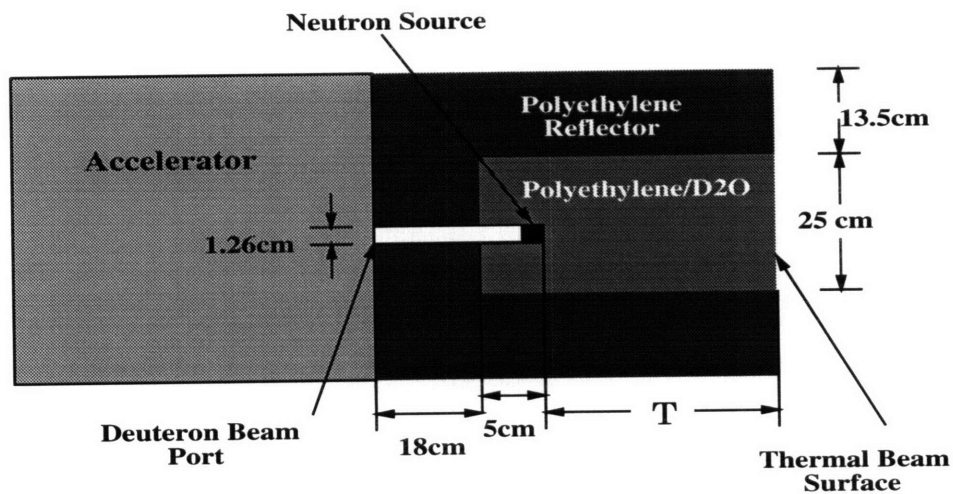
- Although  $D_2O$  does not yield the highest flux density near the source, the density does not drop off as rapidly as for  $H_2O$  or polyethylene; therefore, if a large beam port is needed,  $D_2O$  may result in a more uniform thermal beam.

Polyethylene was chosen as the primary moderator material for the four moderator designs presented below due to its ability to thermalize neutrons, as assessed by thermal neutron density analysis.  $D_2O$  was tested on a limited basis (model I only) to evaluate its ability to produce a more spatially uniform thermal beam than polyethylene. It was decided not to use beryllium as a reflector despite its use as a reflector in reactor engineering based on the minimal gains achieved in thermal neutron density when beryllium was used as a reflector; and after considering the difficulty of obtaining, handling, and machining beryllium.

### **4.3.2 Model I**

Model I is a cylindrical moderator surrounding the neutron source. A schematic of the design is shown in Fig. 4.8. Two materials were tested: 1) polyethylene, and 2)  $D_2O$  surrounded by a polyethylene container.  $D_2O$  was chosen due to its relatively uniform flux density distribution in the previous analysis; thus, it was thought  $D_2O$  may result in a more spatially uniform thermal flux distribution across the face of the thermal beam surface. For the  $D_2O$  moderator, the surrounding polyethylene acts as both a container and reflector. The only geometric variable in this model was the thickness,  $T$ , of the cylindrical moderator relative to the neutron source (Fig. 4.8). Moderator thicknesses of 1, 2, 3, 4, 5, and 10cm were analyzed for polyethylene, and 1, 5, and 10 cm for  $D_2O$ .





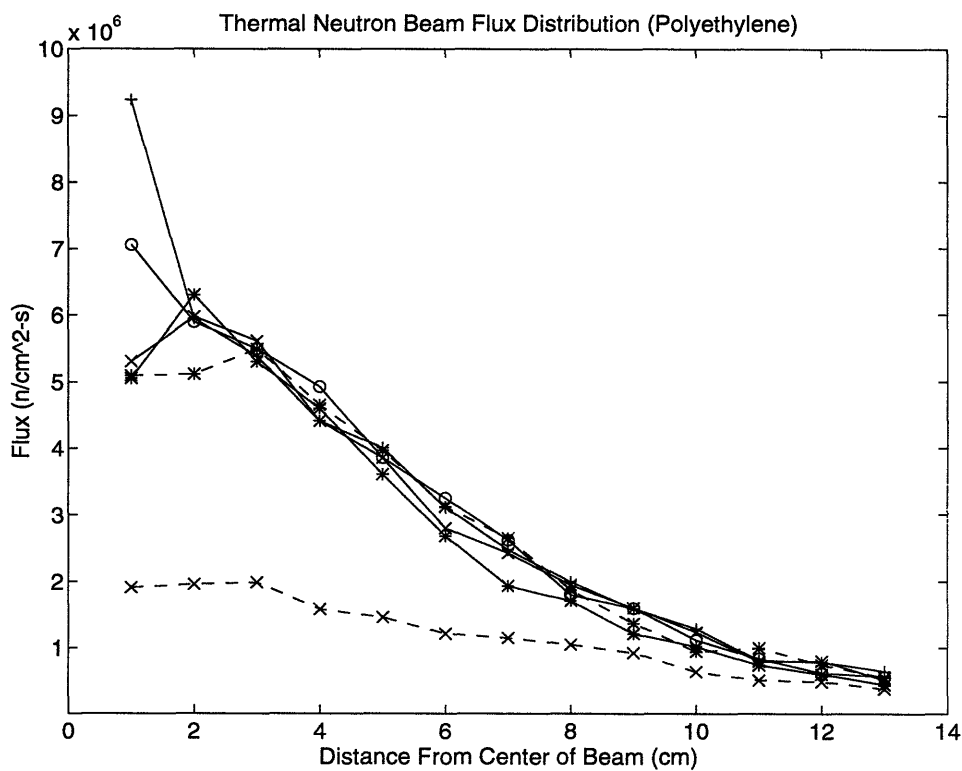
**Figure 4.8:** Schematic (cross-section) of the cylindrical polyethylene and D<sub>2</sub>O-polyethylene moderator. The thickness, T, was varied from 1-10 cm, all other dimensions remained constant.

Figure 4.9 and Table 4.1 present the results for the polyethylene moderator. Figure 4.9 illustrates the decrease in flux with radial distance from the center of the beam, with the coefficient of variation (COV) ranging from 0.49-0.79. A thickness of 3 cm yielded the highest mean flux ( $3.21 \times 10^6$  n/cm<sup>2</sup>-s) emerging from the thermal beam surface, however, this thickness also had the largest COV (0.79).

Results of the D<sub>2</sub>O-polyethylene moderator are presented in Fig.4.10 and Table 4.2. D<sub>2</sub>O yielded a more spatially uniform thermal beam with COV ranging from 0.17-0.41; however, the increase in flux uniformity was at the expense of flux magnitude (e.g.,  $6.0 \times 10^5$  n/cm<sup>2</sup>-s mean flux for the most uniform beam).

Given the results of the flux density analysis, and the fact that in this design the distance from the source to the thermal beam surface increases with distance from the center of the thermal beam surface, it is not surprising that spatial uniformity of the polyethylene moderator is poor. Additionally, the fact that D<sub>2</sub>O results in a more uniform thermal beam with lower flux is also

consistent with the flux density results. The next model attempts to produce a more uniform beam by displacing the moderator a certain distance from the source.



**Figure 4.9:** Thermal neutron beam flux distribution for cylindrical polyethylene moderators with thicknesses of 1, 2, 3, 4, 5, and 10 cm. (\*, solid) 1cm; (x, solid) 2cm; (+, solid) 3cm; (o, solid) 4cm; (\*, dashed) 5cm; (x, dashed) 10cm.

**Table 4.1**  
**Polyethylene Moderator Flux Statistics**

<sup>a</sup> Thickness	Mean Flux (n/cm <sup>2</sup> -s)	Standard Deviation	Coefficient of Variation	Mean MCNP Error
1 cm	2.71 x 10 <sup>6</sup>	2.04 x 10 <sup>6</sup>	0.75	0.10
2 cm	2.87 x 10 <sup>6</sup>	2.0 x 10 <sup>6</sup>	0.68	0.08
3 cm	3.21 x 10 <sup>6</sup>	2.54 x 10 <sup>6</sup>	0.79	0.08
4 cm	3.05 x 10 <sup>6</sup>	2.22 x 10 <sup>6</sup>	0.73	0.08
5 cm	2.81 x 10 <sup>6</sup>	1.86 x 10 <sup>6</sup>	0.66	0.08
10 cm	1.17 x 10 <sup>6</sup>	5.76 x 10 <sup>5</sup>	0.49	0.11

<sup>a</sup> Distance from the center of the source to the beam port surface.

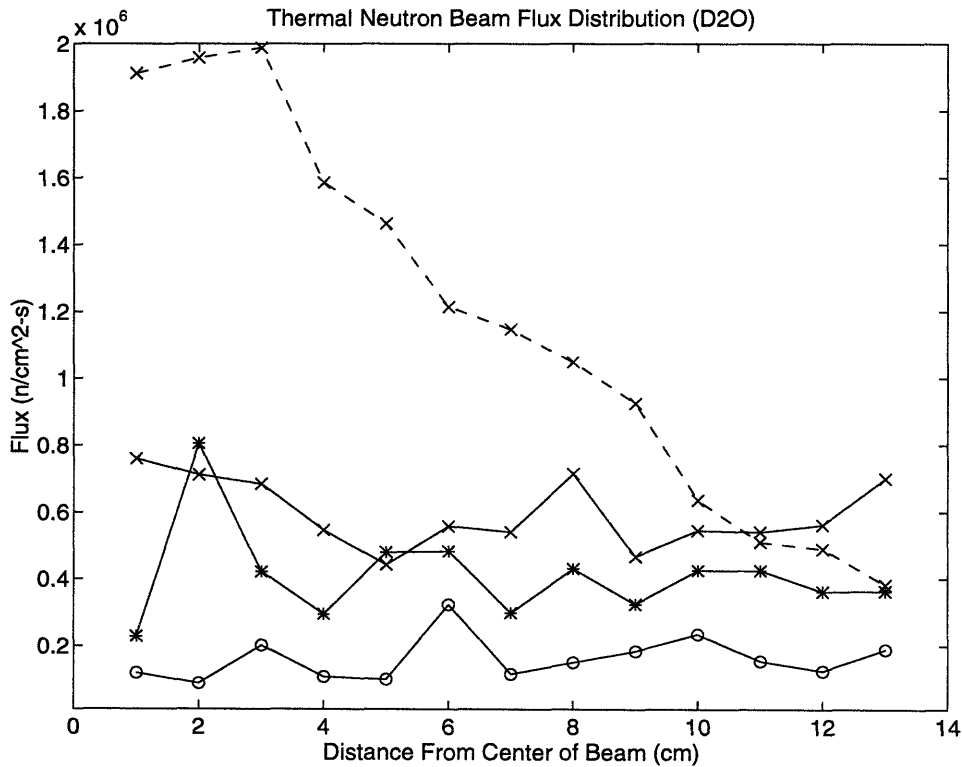


**Figure 4.10:** Thermal neutron beam flux distribution for cylindrical D<sub>2</sub>O-polyethylene moderator with thicknesses of 1, 5, and 10 cm. The curve for the 10 cm thick polyethylene is included for comparison. (o, solid) 1cm D<sub>2</sub>O; (\*, solid) 2cm D<sub>2</sub>O; (x, solid) 10cm D<sub>2</sub>O; (x, dashed) 10cm polyethylene.

**Table 4.2**  
**D<sub>2</sub>O Moderator Flux Statistics**

<sup>a</sup> Thickness	Mean Flux (n/cm <sup>2</sup> -s)	Standard Deviation	Coefficient of Variation	Mean MCNP Error
1 cm	1.61 x 10 <sup>5</sup>	6.62 x 10 <sup>4</sup>	0.41	0.35
5 cm	4.11 x 10 <sup>5</sup>	1.41 x 10 <sup>5</sup>	0.34	0.26
10 cm	6.0 x 10 <sup>5</sup>	1.03 x 10 <sup>5</sup>	0.17	0.19

<sup>a</sup> Distance from the center of the source to the beam port surface.

### 4.3.3 Model II

Model II attempts to produce a more uniform thermal beam by displacing a polyethylene moderator a distance D from the neutron source (Fig. 4.11). Fast neutrons are emitted by the source into a void which is enclosed by a polyethylene reflector and moderator. Two geometric parameters were varied in this design: 1) the thickness of the moderator, T, and 2) the distance, D, from the center of the neutron source to the beginning of the moderator. Moderator thickness was varied from 1-5 cm; distance, D, varied from 1-5 cm. A schematic of the moderator design and MCNP generated geometry diagrams are shown in Fig. 4.11.

Figure 4.12 and Table 4.3 present the simulation results. Mean thermal neutron flux ranged from 7.2 x 10<sup>5</sup> to 1.39 x 10<sup>6</sup> n/cm<sup>2</sup>-s, with COV ranging from 0.12 to 0.48. The configurations with the highest mean flux also had the highest COV; however, there were several configurations yielding mean thermal fluxes in the range of 9.0 x 10<sup>5</sup> n/cm<sup>2</sup>-s with COVs less than 0.20. Thus, this model yielded thermal beams with higher more uniformly distributed fluxes than model I.

One possible explanation for the improvement in COV with model II is that the combination of fast neutrons entering the moderating material directly from the source and those deflected into

the moderator by the reflector result in a relatively uniform distribution of fast neutrons entering the moderator, and therefore, produce a more uniform thermal neutron flux at the thermal beam surface. The next model returns to the concept of surrounding the source with moderating material, and uses a conical shaped moderator.

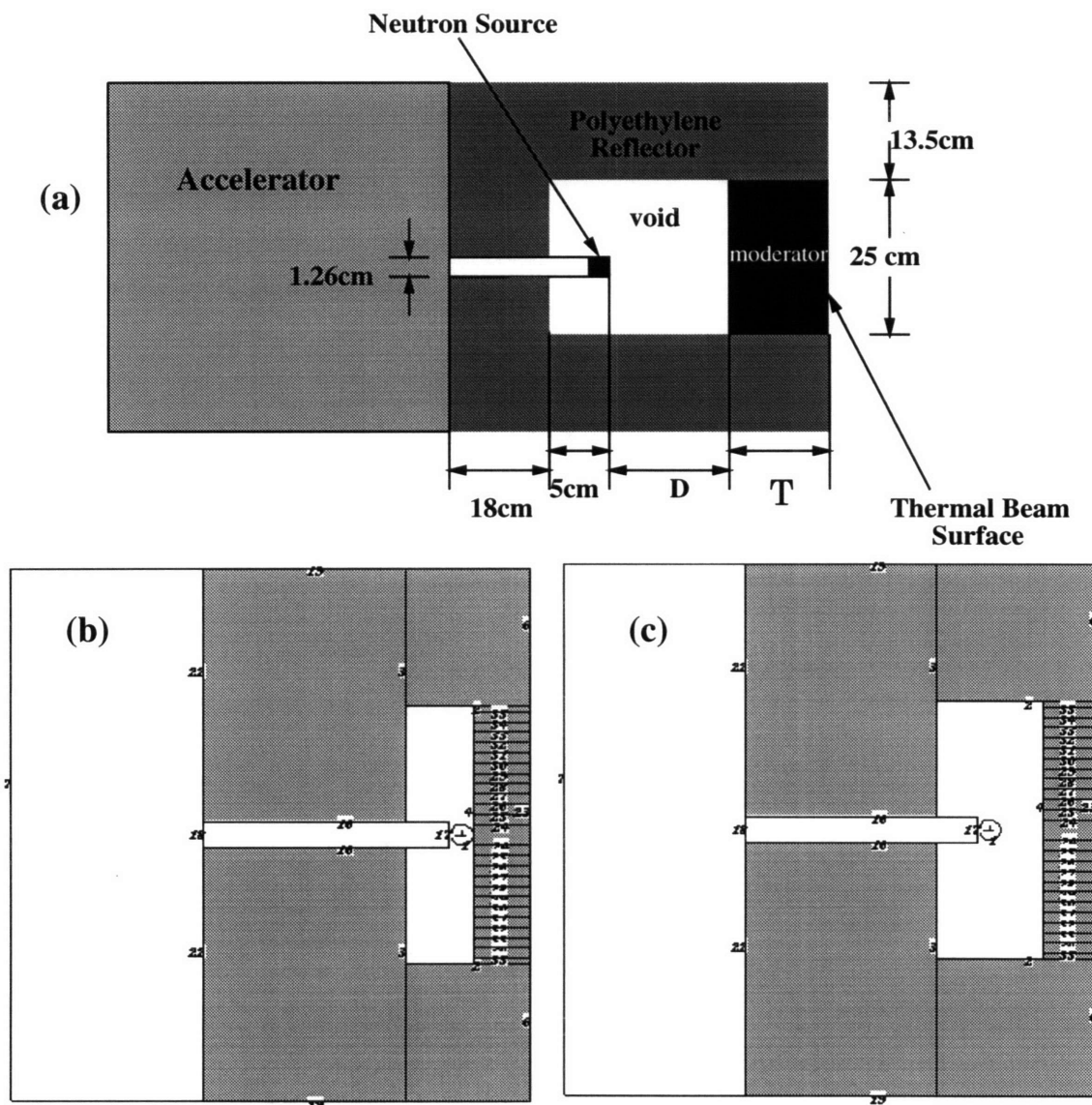


**Figure 4.11:** Schematic (cross-section) of the void-slab polyethylene moderator and reflector (a), and MCNP generated geometry diagrams for (b)  $T=5$   $D=1$ , and (c)  $T=5$   $D=5$ . Two geometric parameters were varied in this design: 1) the thickness of the moderator,  $T$ , and 2) the distance,  $D$ , from the center of the neutron source to the beginning of the moderator. Moderator thickness was varied from 1-5 cm; distance,  $D$ , varied from 1-5 cm; all other dimensions remained constant.

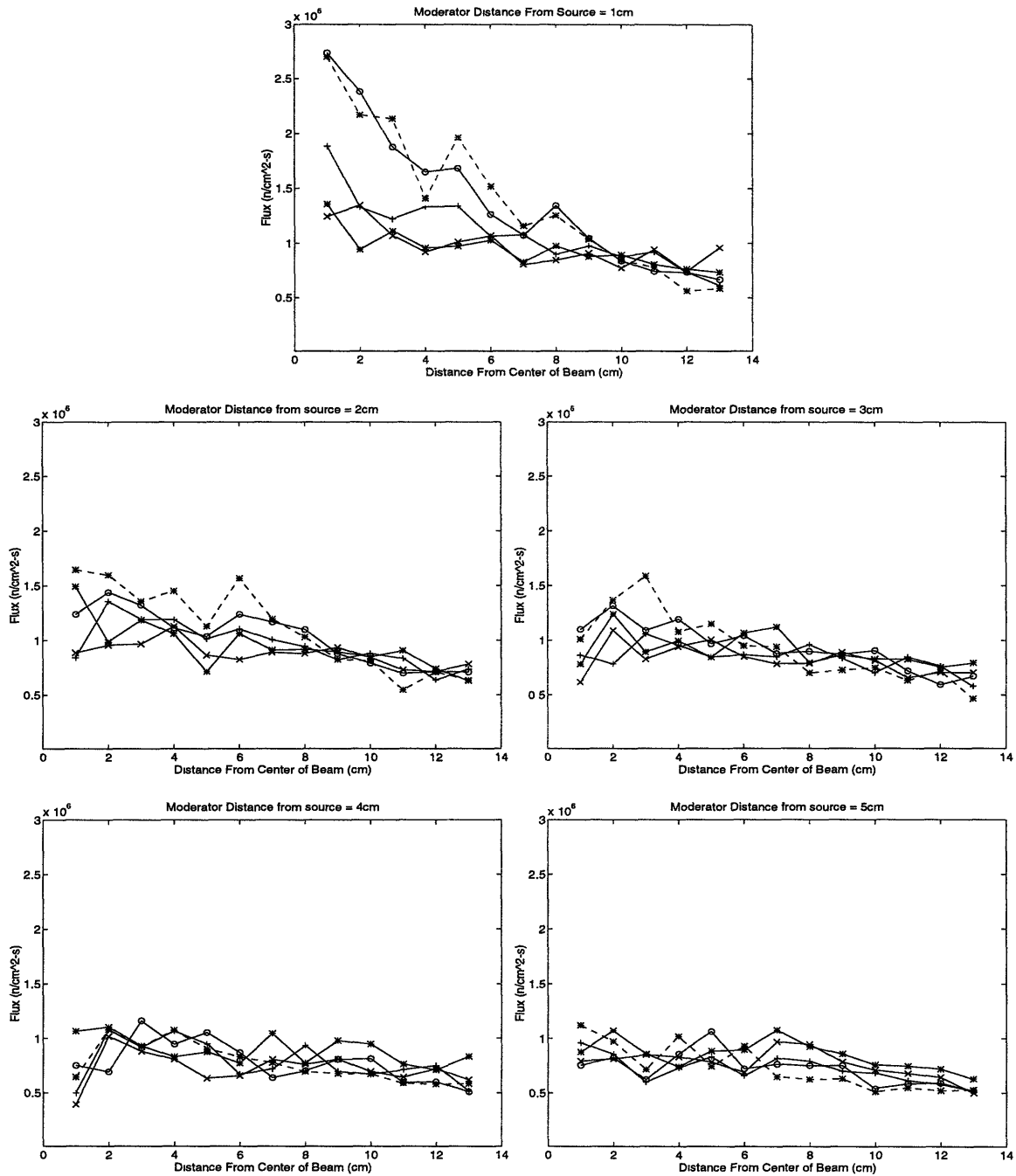


**Figure 4.12:** Thermal neutron beam flux distribution for the void-slab moderator. Moderator thickness was varied from 1-5 cm; distance,  $D$ , varied from 1-5 cm. Each plot represents a constant distance,  $D$ , with thickness,  $T$ , varying from 1-5 cm. (\*, solid)  $T=1$  cm; (x, solid)  $T=2$  cm; (+, solid)  $T=3$  cm; (o, solid)  $T=4$  cm; (\*, dashed)  $T=5$  cm.

**Table 4.3**  
**Void-Slab Moderator Flux Statistics**

Distance From Source	Moderator Thickness	Mean Flux (n/cm <sup>2</sup> -s)	Standard Deviation	Coefficient of Variation	Mean MCNP Error
1 cm	1 cm	9.41 x 10 <sup>5</sup>	1.64 x 10 <sup>5</sup>	0.18	0.13
1 cm	2 cm	9.71 x 10 <sup>5</sup>	1.78 x 10 <sup>5</sup>	0.18	0.12
1 cm	3 cm	1.1 x 10 <sup>6</sup>	3.3 x 10 <sup>5</sup>	0.30	0.11
1 cm	4 cm	1.39 x 10 <sup>6</sup>	6.52 x 10 <sup>5</sup>	0.47	0.13
1 cm	5 cm	1.39 x 10 <sup>6</sup>	6.73 x 10 <sup>5</sup>	0.48	0.12
2 cm	1 cm	9.51 x 10 <sup>5</sup>	2.23 x 10 <sup>5</sup>	0.23	0.13
2 cm	2 cm	8.78 x 10 <sup>5</sup>	1.09 x 10 <sup>5</sup>	0.12	0.13
2 cm	3 cm	9.67 x 10 <sup>5</sup>	2.03 x 10 <sup>5</sup>	0.21	0.13
2 cm	4 cm	1.04 x 10 <sup>6</sup>	2.51 x 10 <sup>5</sup>	0.24	0.12
2 cm	5 cm	1.12 x 10 <sup>6</sup>	3.87 x 10 <sup>5</sup>	0.35	0.13
3 cm	1 cm	9.08 x 10 <sup>5</sup>	1.5 x 10 <sup>5</sup>	0.17	0.13
3 cm	2 cm	8.22 x 10 <sup>5</sup>	1.37 x 10 <sup>5</sup>	0.17	0.13
3 cm	3 cm	8.4 x 10 <sup>5</sup>	1.2 x 10 <sup>5</sup>	0.14	0.13
3 cm	4 cm	9.43 x 10 <sup>5</sup>	2.07 x 10 <sup>5</sup>	0.22	0.12
3 cm	5 cm	9.29 x 10 <sup>5</sup>	3.13 x 10 <sup>5</sup>	0.33	0.13
4 cm	1 cm	9.0 x 10 <sup>5</sup>	1.27 x 10 <sup>5</sup>	0.14	0.13
4 cm	2 cm	7.28 x 10 <sup>5</sup>	1.51 x 10 <sup>5</sup>	0.21	0.15
4 cm	3 cm	7.85 x 10 <sup>5</sup>	1.89 x 10 <sup>5</sup>	0.24	0.15
4 cm	4 cm	7.82 x 10 <sup>5</sup>	1.89 x 10 <sup>5</sup>	0.24	0.14
4 cm	5 cm	7.73 x 10 <sup>5</sup>	1.77 x 10 <sup>5</sup>	0.23	0.14
5 cm	1 cm	8.5 x 10 <sup>5</sup>	1.35 x 10 <sup>5</sup>	0.15	0.13
5 cm	2 cm	7.7 x 10 <sup>5</sup>	1.26 x 10 <sup>5</sup>	0.16	0.14
5 cm	3 cm	7.19 x 10 <sup>5</sup>	1.27 x 10 <sup>5</sup>	0.17	0.14
5 cm	4 cm	7.2 x 10 <sup>5</sup>	1.49 x 10 <sup>5</sup>	0.21	0.15
5 cm	5 cm	7.33 x 10 <sup>5</sup>	2.09 x 10 <sup>5</sup>	0.29	0.14

### 4.3.4 Model III

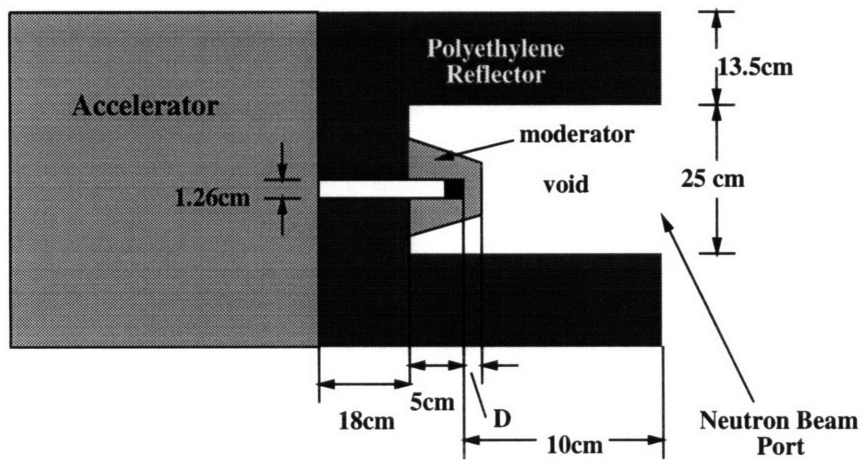
Model III incorporates a truncated-cone-shaped polyethylene moderator (referred to below as the conical moderator) surrounding the neutron source and a polyethylene reflector (Fig. 4.13). The geometric variables included the distance,  $D$ , the moderator extends from the source, and the apex of the moderator cone. The conical shape resulted from defining a cone (in the MCNP input file) which was truncated near the apex by the surface at distance  $D$ . The apex of the cone was moved farther from the source as  $D$  increased, resulting in a larger increase in the amount of moderator surrounding the source than if it was held constant; however, the only variable referenced in the following results is the distance  $D$ . Distances of 1, 3, 4, 5, and 6 cm were tested. Figure 4.13 and 4.14 show a schematic of the moderator and MCNP generated geometry diagrams for moderators with  $D$  equal to 3 and 6 cm.

Figure 4.15 and Table 4.4 present the simulation results. Mean thermal neutron flux ranged from  $2.49 \times 10^6$  to  $3.22 \times 10^6$  n/cm<sup>2</sup>-s, with COV ranging from 0.08 to 0.15. The configuration with  $D$  equal to 6 cm had both the highest mean flux and the lowest COV. Thus, this model yielded thermal beams with higher more uniformly distributed fluxes than either models I or II.

There is a major difference between this model and models I and II that may play a role in producing a more uniform thermal beam with a larger flux: part of the beam port is exposed to the reflector. Although the term *reflector* is used, neutrons within the reflector are moderated in addition to being deflected back into the conical moderator; thus, thermal neutrons emitted from the reflector in the direction of the beam port will contribute to the thermal beam flux.

The next model also benefits from thermal neutrons emitted from the reflector, but attempts to distribute the moderator material around the source more uniformly than model III by using a spherical, as apposed to conical, moderator design.





**Figure 4.13:** Schematic (cross-section) of the conical polyethylene moderator and reflector. The geometric variables included the distance,  $D$ , the moderator extends from the source, and the apex of the moderator cone.

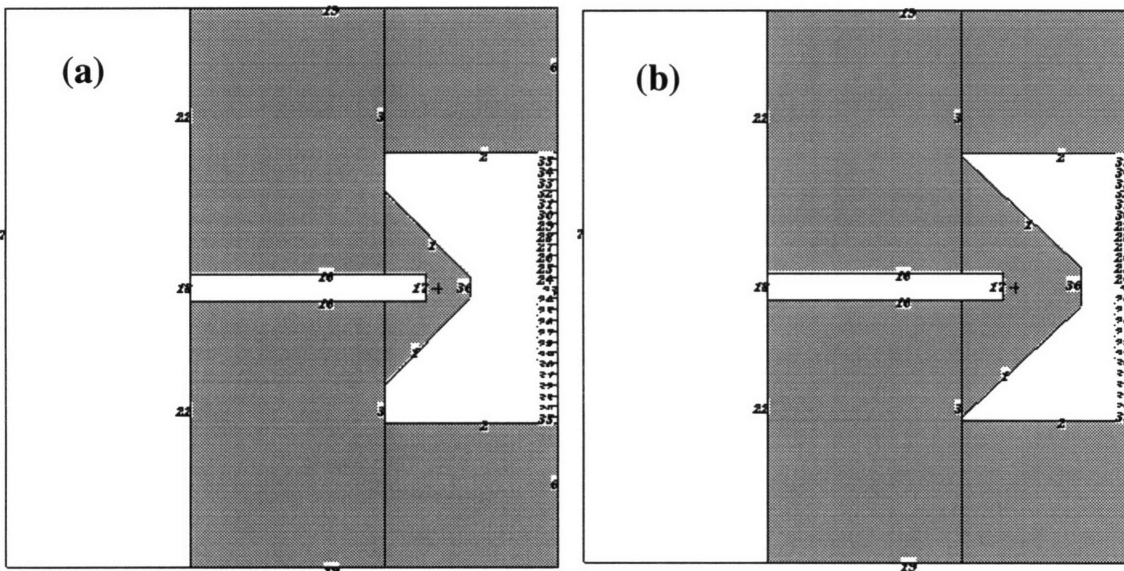


**Figure 4.14:** MCNP generated cross-section diagram of the conical moderator with (a)  $D = 3$  cm, and (b)  $D = 6$  cm. The apex of the cone was moved farther from the source as  $D$  increased, resulting in a larger increase in the amount of moderator surrounding the source than if it was held constant.

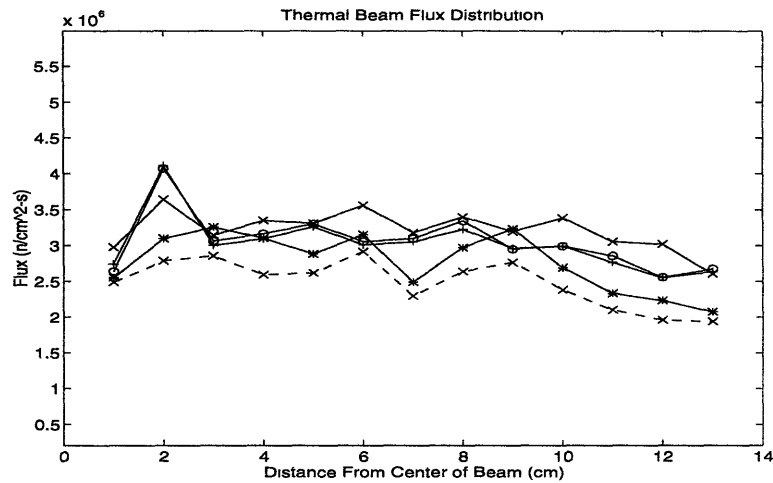


**Figure 4.15:** Thermal neutron beam flux distribution for the conical moderator. Distance,  $D$ , varied from 1-6 cm. (x, dashed)  $D=1$ cm; (\*, solid)  $D=3$ cm; (+, solid)  $D=4$ cm; (o, solid)  $D=5$ cm; (x, solid)  $D=6$ cm.

**Table 4.4**  
**Conical Moderator Flux Statistics**

Thickness	Mean Flux (n/cm <sup>2</sup> -s)	Standard Deviation	Coefficient of Variation	Mean MCNP Error
1 cm	$2.49 \times 10^6$	$3.32 \times 10^5$	0.13	0.08
3 cm	$2.78 \times 10^6$	$4.05 \times 10^5$	0.15	0.08
4 cm	$3.03 \times 10^6$	$3.87 \times 10^5$	0.13	0.08
5 cm	$3.06 \times 10^6$	$3.88 \times 10^5$	0.13	0.08
6 cm	$3.22 \times 10^6$	$2.72 \times 10^5$	0.08	0.07

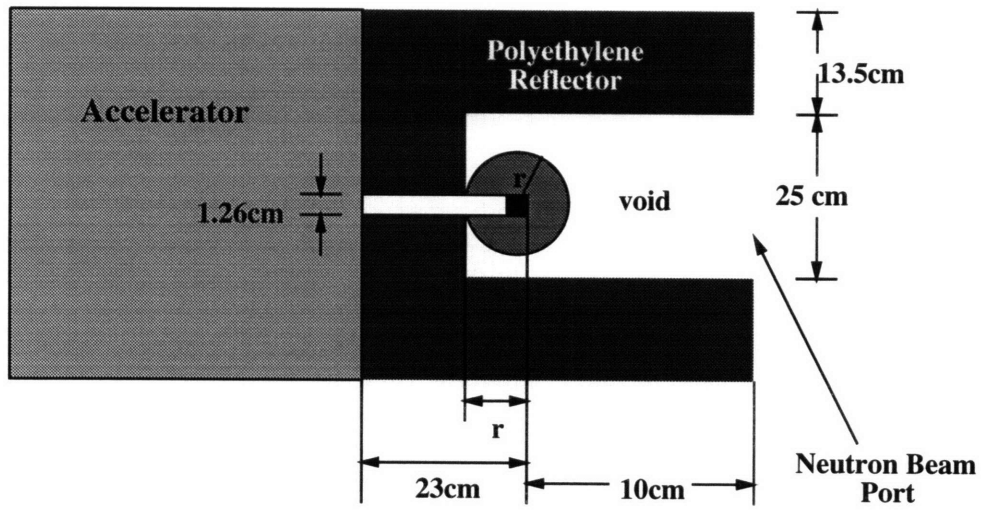
### 4.3.5 Model IV

Model IV is similar to model III but incorporates a spherical polyethylene moderator instead of the conical shape (Fig. 4.16). The neutron source was positioned at the center of the sphere, resulting in a radially uniform thickness of moderator surrounding the source. The only geometric variables were the radius,  $r$ , of the sphere, and the thickness of the inner back wall of the reflecting container, which was altered so that each sphere touched the back wall. To determine the range of

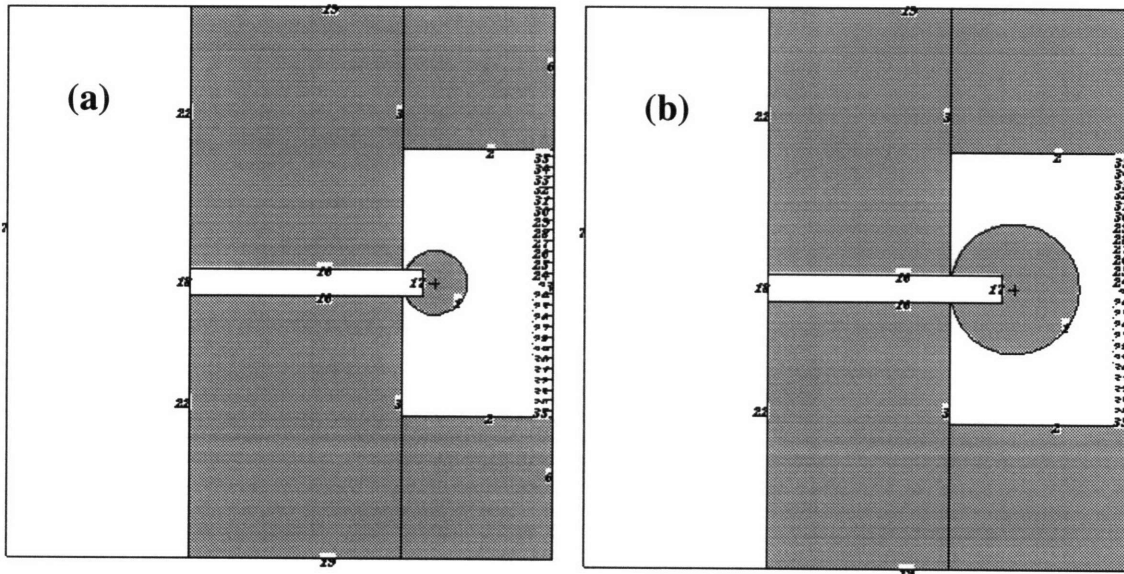
radii to study, a series of simulations was run for spheres with different radii; the neutron source was positioned in the center of each sphere, and the flux across the spherical surface was measured. Results for these simulations are presented Fig. 4.18. Total thermal flux was calculated by summing the neutron flux measurements with energy  $\leq 0.1$  eV and shows a peak at 6 cm; therefore, the radii used for this model were limited to 3, 4, 5, 6, 7, and 8 cm. Figures 4.16 and 4.17 show a schematic of the moderator configuration and MCNP generated diagrams for moderators with radii of 3 and 6 cm.

Figure 4.19 and Table 4.15 show the thermal neutron beam flux distribution and flux statistics for the spherical moderator. Mean flux ranged from  $2.48 \times 10^6$  to  $3.62 \times 10^6$  n/cm<sup>2</sup>-s, with COV ranging from 0.09 to 0.13. A radius of 6 cm yielded both the highest flux and lowest COV. Compared to the best conical moderator, the best spherical moderator yielded slightly higher flux ( $3.62 \times 10^6$  vs.  $3.22 \times 10^6$  n/cm<sup>2</sup>-s) and slightly higher COV (0.09 vs. 0.08). As the radius of the sphere increased--increasing the amount of moderator material surrounding the source--less of the reflector was obstructed compared model III, where the cone was extended; thus, the higher flux for model IV may be due to a larger area of the reflector contributing thermal neutrons to the beam compared to model III.

The results presented next include two geometric variations on the 6 cm spherical moderator. Additionally, the importance of the reflector for thermal beam production of the 6cm spherical moderator was evaluated.



**Figure 4.16:** Schematic (cross-section) of the spherical polyethylene moderator and reflector



**Figure 4.17:** MCNP generated cross-section diagram of the spherical moderator with (a) radius of 3 cm, and (b) radius of 6 cm.

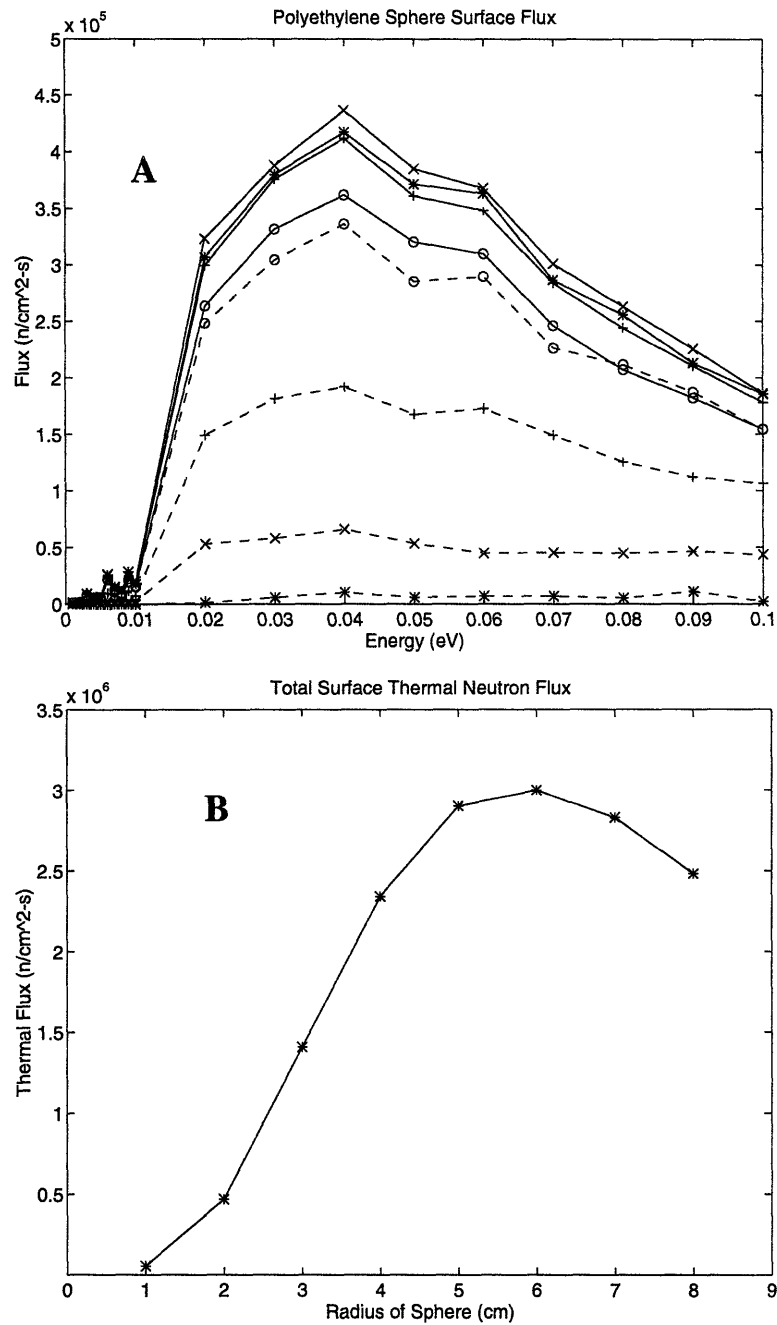


**Figure 4.18:** Thermal neutron surface flux for spheres with different radii. (A) Flux as a function of energy; (\*, dashed) radius 1cm; (x, dashed) radius 2cm; (+, dashed) radius 3cm; (o, dashed) radius 4cm; (\*, solid) radius 5cm; (x, solid) radius 6cm; (+, solid) radius 7cm; (o, solid) radius 8cm. (B) Total surface flux as a function of sphere radius (sum of flux with energy  $\leq 0.1$  eV).

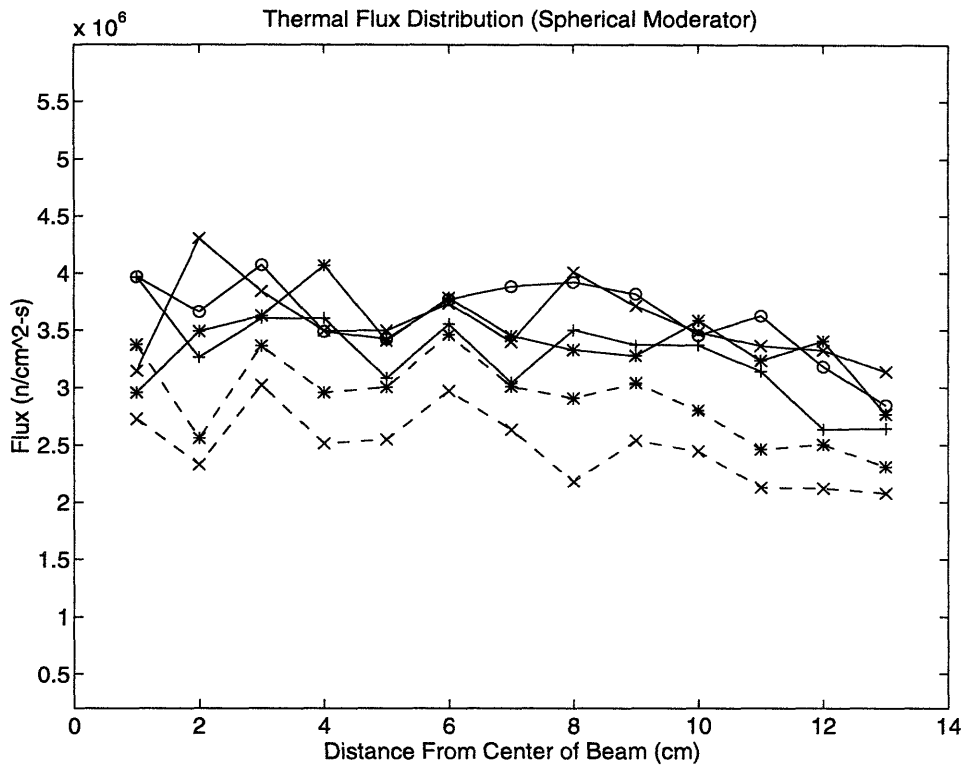


**Figure 4.19:** Thermal neutron beam flux distribution for the spherical moderator: (x, dashed) radius 3cm; (\*, dashed) radius 4cm; (+, solid) radius 5cm; (o, solid) radius 6cm; (x, solid) radius 7cm; (\*, solid) radius 8cm.

**Table 4.5**  
**Spherical Moderator Flux Statistics**

Radius of Moderator Sphere	Mean Flux ( $n/cm^2-s$ )	Standard Deviation	Coefficient of Variation	Mean MCNP Error
3 cm	$2.48 \times 10^6$	$3.1 \times 10^5$	0.13	0.08
4 cm	$2.9 \times 10^6$	$3.68 \times 10^5$	0.13	0.08
5 cm	$3.29 \times 10^6$	$3.82 \times 10^5$	0.12	0.07
6 cm	$3.62 \times 10^6$	$3.43 \times 10^5$	0.09	0.07
7 cm	$3.57 \times 10^6$	$3.38 \times 10^5$	0.09	0.07
8 cm	$3.41 \times 10^6$	$3.32 \times 10^5$	0.10	0.07

### 4.3.5.1 Variations on Model IV and Reflector Importance

Three variations of the 6 cm radius spherical moderator were tested: 1) A 4 cm deep notch was removed from the front facing portion of the sphere, 2) a portion of the void space for the notched moderator was filled with polyethylene, resulting in a cone-shaped beam port, and 3) to test the importance of the polyethylene reflector, the reflector was removed from the 6 cm spherical configuration. Figure 4.20 shows the MCNP geometry diagrams for these three modifications.

Figures 4.21 and 4.22 show the results for these moderators--each plot contains the results for the 6 cm spherical moderator for comparison. Table 4.6 lists the flux statistics for these moderators. Both the notched and the cone-beam moderators had lower mean flux compared to the spherical shape. The COV for the cone-beam moderator was substantially higher (0.36). These results also indicate that the polyethylene reflector plays a significant role in thermal beam production. When the reflector was removed, the mean flux decreased by an order of magnitude and COV increased from 0.09 to 0.37.

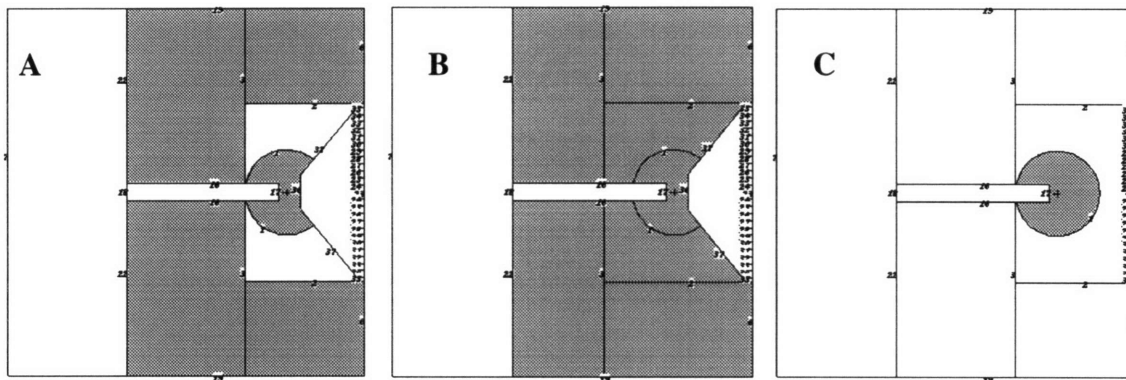


**Figure 4.20:** Three variations of the 6 cm radius spherical moderator. (A) A 4 cm deep notch was removed from the front facing portion of the sphere; (B) a portion of the void space for the notched moderator was filled with polyethylene, resulting in a cone-shaped beam port; (C) the reflector was removed from the 6 cm spherical configuration.

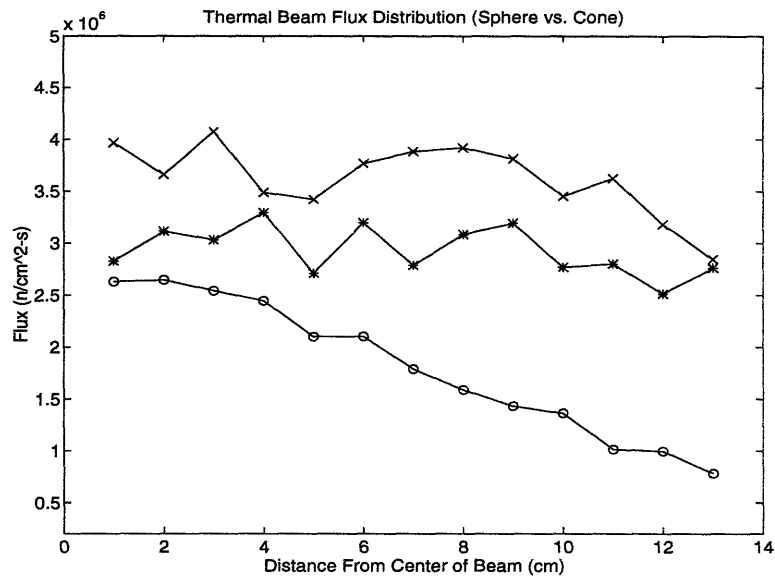


**Figure 4.21:** Thermal neutron beam flux distribution for the 6cm spherical moderator (x, solid); notched moderator (\*, solid); and cone-beam moderator (o, solid).

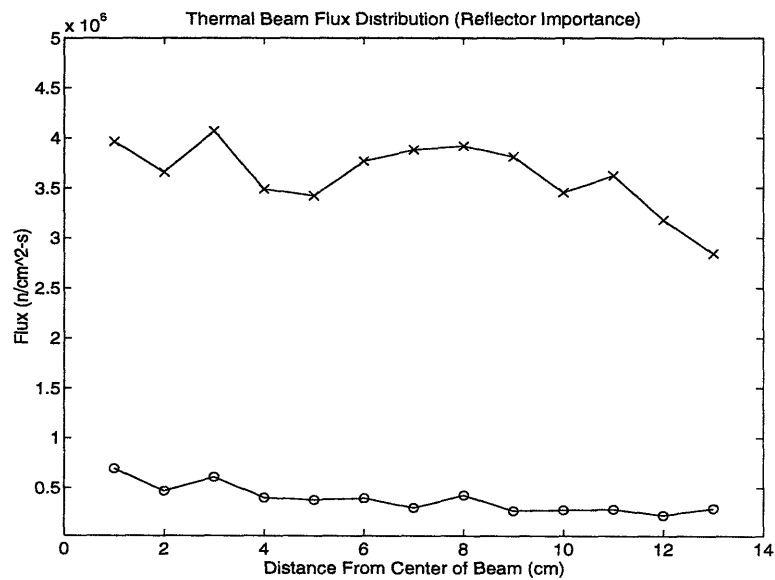


**Figure 4.22:** Thermal neutron beam flux distribution for the 6cm spherical moderator with (x, solid), and without (o, solid) a polyethylene reflector.



**Table 4.6**  
**Flux Statistics For Variations Of The 6 cm Radius Sphere Moderator**

Moderator	Mean Flux (n/cm <sup>2</sup> -s)	Standard Deviation	Coefficient of Variation	Mean MCNP Error
Notched	2.93 x 10 <sup>6</sup>	2.35 x 10 <sup>5</sup>	0.08	0.07
Void filled (cone beam)	1.8 x 10 <sup>6</sup>	6.6 x 10 <sup>5</sup>	0.36	0.08
No Reflector	3.87 x 10 <sup>5</sup>	1.37 x 10 <sup>5</sup>	0.37	0.14

## 4.4 Thermal Beam L/D Ratio

A spherical moderator with a radius of 6 cm surrounded by a polyethylene reflector yielded the highest mean thermal flux (3.62 x 10<sup>6</sup> n/cm<sup>2</sup>-s). A conical moderator with moderating material extending 6 cm from the source, surrounded by a polyethylene reflector, also yielded a high thermal flux (3.22 x 10<sup>6</sup> n/cm<sup>2</sup>-s) and had a slightly lower coefficient of variation than the spherical model (0.08 vs. 0.09). An attempt was made to identify the better configuration by comparing their thermal flux for several ranges of L/D ratio (see section 2.4.2 for discussion of L/D ratio). Table 4.7 shows the results of this analysis. The spherical moderator again yielded slightly higher flux in all but the highest L/D range, however, the MCNP errors in this range were high enough to suggest that no significant difference can be concluded

**Table 4.7**  
**Comparison of Spherical and Conical Moderator Flux L/D Ratio**

L/D Ratio	Spherical Moderator		Conical Moderator	
	Thermal Neutron Flux (n/cm <sup>2</sup> -s)	MCNP Error	Thermal Neutron Flux (n/cm <sup>2</sup> -s)	MCNP Error
0-12	2.02x 10 <sup>6</sup>	0.0033	1.8 x 10 <sup>6</sup>	0.0036
12-24	1.32 x 10 <sup>4</sup>	0.045	1.23 x 10 <sup>4</sup>	0.046
24-100	3.83 x 10 <sup>3</sup>	0.083	3.5 x 10 <sup>3</sup>	0.084
> 100	2.5 x 10 <sup>2</sup>	0.32	3.26 x 10 <sup>2</sup>	0.29

## 4.5 Summary

Polyethylene was chosen as the primary moderator material for the four moderator designs presented below due to its ability to thermalize neutrons, as assessed by thermal neutron density analysis. D<sub>2</sub>O was tested on a limited basis (model I only) to evaluate its ability to produce a more spatially uniform thermal beam than polyethylene. It was decided not to use beryllium as a reflector despite its use as a reflector in reactor engineering based on the minimal gains achieved in thermal neutron density when beryllium was used as a reflector; and after considering the difficulty of obtaining, handling, and machining beryllium.

For model I (polyethylene), the coefficient of variation (COV) ranging from 0.49-0.79. A thickness of 3 cm yielded the highest mean flux (3.21 x 10<sup>6</sup> n/cm<sup>2</sup>-s) emerging from the thermal beam surface, however, this thickness also had the largest COV (0.79). The D<sub>2</sub>O-polyethylene moderator yielded a more spatially uniform thermal beam with COV ranging from 0.17-0.41; however, the increase in flux uniformity was at the expense of flux magnitude (e.g., 6.0 x 10<sup>5</sup> n/cm<sup>2</sup>-s mean flux for the most uniform beam).

For model II, mean thermal neutron flux ranged from  $7.2 \times 10^5$  to  $1.39 \times 10^6$  n/cm<sup>2</sup>-s, with COV ranging from 0.12 to 0.48. The configurations with the highest mean flux also had the highest COV; however, there were several configurations yielding mean thermal fluxes in the range of  $9.0 \times 10^5$  n/cm<sup>2</sup>-s with COVs less than 0.20. This model yielded thermal beams with higher more uniformly distributed fluxes than model I.

For model III, mean thermal neutron flux ranged from  $2.49 \times 10^6$  to  $3.22 \times 10^6$  n/cm<sup>2</sup>-s, with COV ranging from 0.08 to 0.15. The configuration with D equal to 6 cm had both the highest mean flux and the lowest COV. This model yielded thermal beams with higher more uniformly distributed fluxes than either models I or II.

For model IV, mean flux ranged from  $2.48 \times 10^6$  to  $3.62 \times 10^6$  n/cm<sup>2</sup>-s, with COV ranging from 0.09 to 0.13. A radius of 6 cm yielded both the highest flux and lowest COV. Compared to the best conical moderator, the best spherical moderator yielded slightly higher flux ( $3.62 \times 10^6$  vs.  $3.22 \times 10^6$  n/cm<sup>2</sup>-s) and slightly higher COV (0.09 vs. 0.08).

For the variations on model IV with a 6 cm radius sphere, both the notched and the cone-beam moderators had lower mean flux compared to the spherical shape. The COV for the cone-beam moderator was substantially higher (0.36). These results also indicate that the polyethylene reflector plays a significant role in thermal beam production. When the reflector was removed, the mean flux decreased by an order of magnitude and COV increased from 0.09 to 0.37.

Thermal beam L/D ratio analysis of the best configurations of models III and IV resulted in the spherical moderator again yielding slightly higher flux in all but the highest L/D range, however, the MCNP errors in this range were high enough to suggest that no significant difference can be concluded.

It is not assumed that all moderator designs, or even all variations of those presented, have been evaluated. Thus, it cannot be concluded that those moderators yielding the highest most uniform flux are in fact the optimum design. One parameter that was not varied was the

temperature of the moderating material. As shown in Fig. 2.18, decreasing the temperature shifts the thermal peak toward lower energy. Figure 4.18 shows a relatively diffuse thermal energy distribution. Lowering the temperature of the polyethylene will lead to a shift in the thermal peak, and may also increase the total thermal flux by lowering the energy of neutrons in the epithermal range (with moderator temperature of 300 °K) into the thermal range.

Additionally, the mathematical model resulting in the energy and angular distribution of the neutron source used in these simulations assumed a thin beryllium target; recent investigations (66) show that a  ${}^9\text{Be}(d,n){}^{10}\text{B}$  reaction using a thick target (0.75 mm) results in an energy spectrum (for  $0^\circ$  trajectories) with the majority of neutrons having energies ranging from 0.5 to 2.0 MeV; however, these results are for incident deuterons energies of 2.6 MeV. The Be target used with our accelerator can be considered a thick target (38 mm), therefore, if these results hold true for deuteron energies in the range of 0.9 MeV, the moderator designs presented here should result in a higher thermal neutron flux than is indicated.

# Chapter 5

## Conclusions

It has become apparent that although high flux reactor sources are useful for high resolution radiographic and tomographic imaging of small engine parts and electrical components, if neutron imaging is to achieve widespread applicability, the neutron source will have to become smaller, more affordable, and more portable than a nuclear reactor. Although radioisotopes are small and easily maintained, the thermal neutron flux achievable with these sources makes their use on a broad basis unlikely. Accelerators, however, are now producing neutron fluxes equal to many reactors; and small, compact, accelerators, such as the one used in this project, still produce neutron fluxes greater than radioisotope sources and yet are easily operated and maintained.

Many industrial applications would benefit from a radiographic system capable of imaging large areas. Accelerator based neutron sources offer a greater potential than reactors for large area radiography, since the size of the thermal neutron beam used for imaging is dependent on the moderator assembly and not the dimensions of a reactor's thermal neutron beam port. The challenge, then, is to produce a thermal neutron beam with a large cross-sectional area, and a high, spatially uniform, flux.

The objective of this work was to produce a uniform thermal beam with an area greater than our scintillating converter screen (432 cm<sup>2</sup>). Moderator designs producing a cylindrical thermal beam with cross-sectional area of 491 cm<sup>2</sup> (12.5 cm radius) were analyzed theoretically using a Monte Carlo Neutron-Particle Transport simulation (MCNP) code. Polyethylene was chosen as the primary material for both the moderator and reflector material based on its ability to thermalize neutrons, as assessed by thermal neutron density analysis. D<sub>2</sub>O was tested in model I, but due to the low thermal flux achieved, it was not used for subsequent models. It was decided not to use beryllium as a reflector after considering the difficulty of obtaining, handling, and machining beryllium, and the minimal gains achieved in thermal neutron density analysis when beryllium was used as a reflector. The fact that polyethylene is a good neutron moderator is beneficial, since it is inexpensive and easily machined.

A spherical moderator with a radius of 6 cm surrounded by a polyethylene reflector yielded the highest mean thermal flux (3.62 x 10<sup>6</sup> n/cm<sup>2</sup>-s). A conical moderator with moderating material extending 6 cm from the source, surrounded by a polyethylene reflector, also yielded a high thermal flux (3.22 x 10<sup>6</sup> n/cm<sup>2</sup>-s) and had a slightly lower coefficient of variation than the spherical model (0.08 vs. 0.09). Thermal beam L/D ratio analysis of these two moderators resulted in the spherical moderator again yielding slightly higher flux in all but the highest L/D range, however, the MCNP errors in this range were high enough to suggest that no significant difference can be concluded.

The RFQ accelerator to be used in this project will be shipped to MIT in August, 1994. Once the accelerator is operational, several moderator designs will be assembled and evaluated experimentally. The CCD camera system has been assembled and is being tested. Once the full system, including the accelerator, moderator, and camera, has been assembled, the first objective will be to evaluate the systems ability to produce radiographs and tomographs visualizing corrosion within aluminum samples. Quantifying the extent of corrosion from neutron images will also be a major objective.

## References

- [1] Peterka F, Block H, and Pleinert H, Neutron Radiography Standard Testing Method for the Moisture Analysis in Building Materials, *Neutron Radiography: Proceedings of the Fourth World Conference*, Gordon and Breach Publishing Company, 1992.
- [2] Nakanishi TM, Matsumoto S, and Kobayashi H, Applications of Neutron Radiography to Plant Research, *Neutron Radiography: Proceedings of the Fourth World Conference*, Gordon and Breach Publishing Company, 1992.
- [3] Adams L, Andersen J, Ellen PC, Leeftang HP, Neutron Radiograph Inspection of Relays for Satellite and Space Technology Applications, *Neutron Radiography: Proceedings of the Fourth World Conference*, Gordon and Breach Publishing Company, 1992.
- [4] Dance WE, Hohman AE, Rogers RR, Carollo SF, Corrosion Detection in Aerospace Structures Using Small-Accelerator Neutron Radiology: Some Recent Results, *Neutron Radiography: Proceedings of the Fourth World Conference*, Gordon and Breach Publishing Company, 1992.
- [5] Barton JP, Bader JW, Stokes JA, Experience with Aircraft Inspection in the MNRS Using Film and Electronic Imaging, *Neutron Radiography: Proceedings of the Fourth World Conference*, Gordon and Breach Publishing Company, 1992.
- [6] Froom DA, Barton JP, Bader JW, Neutron Radiography at Sacramento ALC, *Neutron Radiography: Proceedings of the Fourth World Conference*, Gordon and Breach Publishing Company, 1992.
- [7] Leeftang HP, Markgraf JFW, Detection of Corrosion on Aircraft Components by Neutron Radiography, *Neutron Radiography: Proceedings of the Fourth World Conference*, Gordon and Breach Publishing Company, 1992.
- [8] Chandrasekharan KN, Patil BP, Ghosh JK, Quantitative Evaluation of Structural Features from Nuclear Fuel Pin Neutron Radiographs, *Neutron Radiography: Proceedings of the Fourth World Conference*, Gordon and Breach Publishing Company, 1992.
- [9] Malgouryres P, Caillot L, Souchon F, Jegat A, Neutron Radiography Applied to Studying the Densification of Nuclear Fuel Pellets Under Irradiation, *Neutron Radiography: Proceedings of the Fourth World Conference*, Gordon and Breach Publishing Company, 1992.
- [10] Fujine S, et al., Study on Visualization of Fluid Phenomena Using Neutron Radiography Technique, *Neutron Radiography: Proceedings of the Fourth World Conference*, Gordon and Breach Publishing Company, 1992.
- [11] Sonoda K, Ono A, Takenaka N, Fujii T, Tazawa S, Nakanii T, Visualization and Volumetric Fraction Measurement of Multiphase Flow by Neutron Radiography, *Neutron Radiography: Proceedings of the Fourth World Conference*, Gordon and Breach Publishing Company, 1992.
- [12] McFarland EW, Leigh J, Dai H, Lanza R, Odette R, Heterogeneous Distribution of Hydrogen in Titanium Compressor Blades: Detection and Characterization by Neutron Computed Tomography, *SPIE Proceedings v2092*, SPIE Optical Engineering Press, Bellingham, (in press).

- [13] McFarland EW, Leigh J, Dai H, Lanza R, Non-Destructive Imaging of Hydrogen in High Performance Titanium Jet Engine Components with Neutron Computed Tomography, *IEEE Nuclear Science Symposium*, 1993.
- [14] Lanza R, McFarland EW, Poulos GW, Computerized Neutron Tomography for Core analysis, *Soc. of Core Analysts*, Conference paper 9128, 12p (August 1991).
- [15] Jongen Y, Delvigne T, Cohilis P, Multi-milliampere Compact Cyclotrons Used as Neutron Sources, 4th International Conference on Applications of Nuclear Techniques: Neutrons and their Applications, Crete, 1994.
- [16] Allen MJ, Rogers JD, Townsend NJ, Hawkesworth MR, Neutron Radiography Using The Nuffield Cyclotron At The University of Birmingham, *Neutron Radiography: Proceedings of the Fourth World Conference*, Gordon and Breach Publishing Company, 1992.
- [17] Yoshii, et al., A study on Fast Neutron Television Using Baby Cyclotron, *Neutron Radiography: Proceedings of the Fourth World Conference*, Gordon and Breach Publishing Company, 1992.
- [18] MCNP4A Manual, RSIC Computer Code Collection, Los Alamos National Laboratory, Los Alamos, New Mexico, December 1993.
- [19] Godin Michael, Mobile Neutron Sources for Residual Stress Measurement, M.S.Thesis, Department of Nuclear Engineering, MIT, 1994.
- [20] Carpenter JM, Yelon WB, Neutron Sources, *Methods of Experimental Physics*, Vol. 23, Part A, pp. 99-195, 1986.
- [21] Hawkesworth MR, Neutron Radiography: Equipment and Methods, *Atomic Energy Review* 15 2 (1977).
- [22] Shaw CB, Cason JL, Portable Neutron radiographic camera using Cf-252, *Mater. Eval.* 29 (1971) 40-44.
- [23] John J, Californium-Based Neutron Radiography for Corrosion Detection In Aircraft, *Neutron Radiography and Gaging* (Berger. H., Ed.), STP 586. ASTM. Philadelphia (1976) 168-82.
- [24] Barton JP, Developments in the use of Californium-252 for Neutron Radiography, *Nucl. Technol.* 15 (1972) 56-67.
- [25] Cassidy JP, Use of a Low-Energy Van de Graaff Accelerator in Neutron Radiography of Encased Explosives, *Practical Applications of Neutron Radiography and Gaging* (Berger. H., Ed.), STP 586. ASTM. Philadelphia (1976) 117-24.
- [26] Dance WE, Neutron Radiographic Evaluation of Aerospace Structures, *Practical Applications of Neutron Radiography and Gaging* (Berger. H., Ed.), STP 586. ASTM. Philadelphia (1976) 137-51.
- [27] Swanson FR, Kuehne FJ, Neutron Radiography with a Van de Graaff Accelerator for Aerospace Applications, *Practical Applications of Neutron Radiography and Gaging* (Berger. H., Ed.), STP 586. ASTM. Philadelphia (1976) 137-51.
- [28] Bacon GE, *Neutron Physics*, Wykeham Publications, London, 1969.
- [29] Scharf W, *Particle Accelerators And Their Uses: Part 2, Applications of Accelerators*, Harwood Academic Publishers, 1986.
- [30] Berger H, *Neutron Radiography*, Elsevier, Amsterdam (1965).



- [31] Berger H, Comparison of Several Methods for the Photographic Detection of Thermal Neutron Images, *J. Appl. Phys.* 33 1 (1962) 48-55.
- [32] Hawkesworth MR, Films for Neutron Radiography: An Investigation of Film-intensifying Screen Image Recorders, *J. Phys., E (London)* 2 (1969) 325-42.
- [33] Hawkesworth MR, Radiography with Low Intensity Neutron Beams: Some Reciprocity Failure Characteristics of Films used with Light-Emitting Intensifying Screens, *J. Phys., E (London)* 2 (1969) 673-78.
- [34] Durrani SA, Khan HA, Solid State Track Detectors for Neutron Image Recording, Radiography with Neutrons (Hawkesworth MR, Ed.). BNES. London (1975) 71-77.
- [35] Berger H, Radiograph with Track-Etch Detectors, *Proc. 7th Int. Conf. Nondestructive Testing*, Warsaw, B (1973).
- [36] Chalmeton V, Microchannel Image Intensifier for Neutron Radiography, *Proc. 7th Int. Conf. Nondestructive Testing*, Warsaw, B (1973).
- [37] Berger H, Characteristics of a Thermal Neutron Television Imaging System, *Mater. Eval.* 24 9 (1966) 475-81.
- [38] Schnurer GT, McMain AT, Neutron Radiography with a TRIGA Neutrovision System, Proc. ANS Conf. Neutron Sources and Applications, Augusta. Conf. 710402 III (1971) 78-86.
- [39] Holland BG, Pain LF, Description and Assessment of a Dynamic Neutron Scinticamera, UKAEA (AWRE) Rep. NP Memo 113 (1971).
- [40] Kobayashi H, Recent Development of Cooled CCD Camera for NR Imaging-Tomography, *Neutron Radiography: Proceedings of the Fourth World Conference*, Gordon and Breach Publishing Company, 1992.
- [41] McFarland E, Lanza R, Na H, Mcguire M, Dai H, Quantitative Evaluation of a Neutron Radiography and Tomography System Using Cooled Charge Coupled Devices Designed for Low Fluence Sources, *Neutron Radiography: Proceedings of the Fourth World Conference*, Gordon and Breach Publishing Company, 1992.
- [42] Na H, McFarland E, Lanza R, A Segmented Array Approach to Large Scale Neutron Radiography and Tomography Using Cooled Charge Coupled Devices, *Neutron Radiography: Proceedings of the Fourth World Conference*, Gordon and Breach Publishing Company, 1992.
- [43] Casali F, et al., A system for Neutron Radiography with a Cooled CCD Camera, *Neutron Radiography: Proceedings of the Fourth World Conference*, Gordon and Breach Publishing Company, 1992.
- [44] Lanza R, McFarland EW, Poulos GW, Multi-Dimensional Neutron-Computed Tomography Using Cooled Charge Coupled Devices, *IEEE Trans. on Nuc. Sci.*, v38 pp. 612-622 (1991).
- [45] McFarland E, Lanza R, Recent Advances In Neutron Tomography, in Carpenter JM, Cline DB, Lanza R, Mildner DF, Eds., SPIE Proceedings Vol. 1737, Neutrons, X rays, and Gamma Rays: Imaging Detectors, Material Characterization Techniques, and Applications, pp. 101-111, SPIE Optical Engineering Press, Bellingham (1992).
- [46] Radon J, Uber die Bestimmung von Funktionen durch ihre Integralwerte langs gewisser Mannigfaltigkeiten, *Ber. Verh. Sachs. Akad. Wiss. Leipzig Math. Phys. Kl.* 69 262-77.

- [47] Webb S, *The Physics of Medical Imaging*, Instituted of Physics Publishing, Bristol and Philadelphia, 1988.
- [48] Feldkamp LA, Davis LC, Dress JW, Practical Cone-Beam Algorithm, *J. Optical Soc. of Amer., Optics and Image Science* vol. 1 pp. 612-619 (1984).
- [49] Bhatia M, Karl WC, Willsky AS, A Wavelet-Based Method For Multiscale Tomographic Reconstruction, *IEEE Transactions on Medical Imaging*, In Press.
- [50] CCD Detectors, Thompson Composants Militaires et Spatiaux, 50 Rue J.P. Timbaud-B.P. 330, Tel: (33-1) 47 68 53 00.
- [51] Lindeburg, MR, *Engineer-In-Training Reference Manual*, 7th edition, Professional Publications, Inc., 1990, p. 35-14.
- [52] ST-138 Controller: Operations Manual, Princeton Instruments Inc., Manual Version 1, Revision B, April 5. 1993.
- [53] Wiedemann H, *Particle Accelerator Physics: Basic Principles and Linear Beam Dynamics*, Springer-Verlag Berlin Heidelberg, 1993.
- [54] Vlasov AD, *Theory of Linear Accelerators*, U.S. Department of Commerce: Clearinghouse for Federal Scientific and Technical Information, Springfield, Virginia, 1968.
- [55] Scharf W, *Particle Accelerators And Their Uses: Part 1, Accelerator Design*, Harwood Academic Publishers, 1986.
- [56] Scharf W, *Particle Accelerators And Their Uses: Part 2, Applications of Accelerators*, Harwood Academic Publishers, 1986.
- [57] Wideroe R, *Archiv fur Elektrotechnik*, **21** 387 (1928).
- [58] Lawrence EO, Livingston MS, *Phys. Rev.*, **40** 19(1932).
- [59] Cockcroft JD, Walton ETS, *Proc. of the Royal Soc. of London*, **A136** 619(1932).
- [60] Kapchinskii IM, Teplyakov VA, Linear ion accelerator with Spatially Homogeneous Strong Focusing, *Prib. Tekh. Eksp.*, **19** 2(1970).
- [61] *Physics of Particle Accelerators*, Month M and Dienes M (eds.), *AIP Conf. Proc. #184, Am. Inst. Phys.*, New York, 1989, p. 1829.
- [62] Krane KS, *Introductory Nuclear Physics*, John Wiley & Sons, Inc., 1988.
- [63] Harms AA, Wyman DR, *Mathematics and Physics of Neutron Radiography*, D. Reidel Publishing Co., Dordrecht, Holland, 1986, pp. 11-13.
- [64] Pruitt JS, Swartz CD, Hanna SS, Energies and Angular Distributions of Neutrons from  ${}^9\text{Be}(d,n){}^{10}\text{B}$ , *Phys. Rev.*, **92** 6(1953) 1456-60.
- [65] Karadeniz MC, Low lying Energy Levels of  ${}^{10}\text{B}_5$ , *J. Phys. A: Math., Nucl. Gen.*, **7** 18(1974) 2284-88.
- [66] Meadows JW, The  ${}^9\text{Be}(d,n)$  Thick-Target Neutron Spectra for Deuteron Energies Between 2.6 and 7.0 MeV, *Nuc. Instr. and Meth. in Phys. Res.*, **A324** (1993) 239-246.

# Appendix I

## Derivation of Neutron Cross-Section

The notion of a cross section as a measure of interaction probability began with the idea that the effective size of a nucleus should be proportional to the probability that an incident particle would react with it. Each spherical nucleus is pictured as representing a cross-section or target area to a parallel beam of neutrons. A small cylinder of area  $dA$  and thickness  $dx$  is constructed of a single-nuclide material with an atom density of  $n$  per  $\text{cm}^3$ . A neutron entering the disk at random location on the surface  $dA$  has a probability of hitting a target nucleus equal to the total area of the target divided by the total area of the disk. If there are  $N$  nuclei, and each nucleus is assumed to have a cross-sectional area  $\sigma$ , then the total area of the target is:

$$NdA = \sigma \rho dV \quad (\text{AI.1})$$

where  $\rho$  is the atom density and  $dV$  the volume of the disk. Then,

$$\rho dV = \rho dA dx \quad (\text{AI.2})$$

and the total area is:

$$\sigma \rho dA dx \quad (\text{AI.3})$$

The probability that a neutron will interact in traveling a distance  $dx$  through the material is:

$$Pi = \frac{\sigma \rho dA dx}{dA} = \rho \sigma dx \quad (\text{AI.4})$$

However the apparent area,  $\sigma$ , changes with neutron energy, i.e., the interaction probability is a function of the neutron energy; therefore, the concept of a nucleus cross-section as the determinant of interaction probability was dropped. The cross section,  $\sigma$ , then, is defined such that its product with the atom density,  $n$ , and distance  $dx$  is equal to the interaction probability:

$$\sigma = \frac{Pi}{\rho dx} \quad (\text{AI.5})$$

and is a function of the type of reaction, neutron energy, and target nuclide.

This quantity, with units of  $\text{cm}^{-2}$ , is known as the microscopic cross-section. It is an effective area used to characterize a single nucleus. It is a probability per unit nuclide density and per unit thickness of material through which the neutrons travel. There is also a macroscopic cross-section,  $\Sigma$ , with units of  $\text{cm}^{-1}$ . It is simply the product of the microscopic cross-section and the atom density of a material. The macroscopic cross-section is the probability per unit distance traveled that a neutron will interact with a material; therefore, it also is a function of reaction type, neutron energy, and target nuclide.

## Appendix II

### Neutron Beam Attenuation

Since contrast in a neutron radiographic image is the result of a spatially differential attenuation of the incident neutron beam, it will be defined quantitatively. We introduce the term neutron flux,  $\Phi$ :

$$\Phi = Nv \quad (\text{AII.1})$$

$N$  = density of neutrons per unit volume

$v$  = distance per unit time

$$\Phi = \frac{\text{neutrons}}{\text{Area} \cdot \text{time}} = \frac{\text{neutrons}}{\text{cm}^2 \cdot \text{s}} \quad (\text{AII.2})$$

The rate of neutron interaction, or reaction rate, is equal to:

$$\Sigma \Phi dV \quad (\text{AII.3})$$

or,

$$\Sigma \Phi = \frac{\text{ReactionRate}}{\text{UnitVolume}} \quad (\text{AII.4})$$

when the volume is unspecified, and  $\Sigma$  is now the total macroscopic cross-section for all the different reactions and energies for a given nuclide.

If a beam of monoenergetic neutrons crosses the surface of a sample, one neutron will be removed for each reaction. Thus, the rate of decrease of neutron flux with distance will equal the reaction rate:

$$\frac{d}{dx} \Phi(x) = -\Sigma \Phi(x) \quad (\text{AII.5})$$

$$\Phi(x) = \Phi(0) e^{-\Sigma x} \quad (\text{AII.6})$$

where  $\Sigma$  is again the total macroscopic cross-section, implying that all interactions, including scattering, remove neutrons from the incident beam.

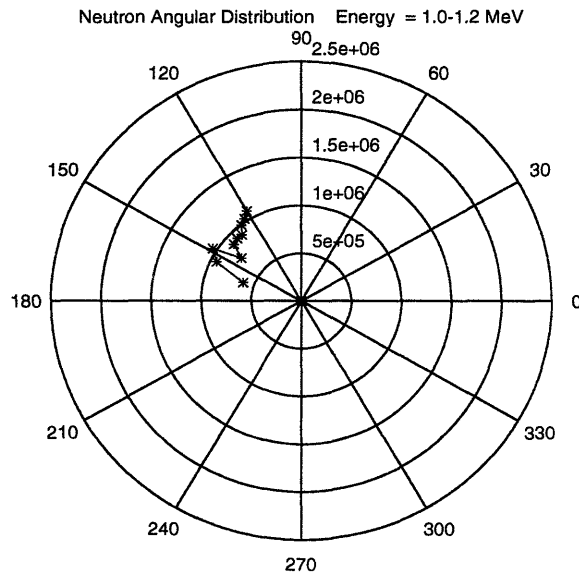
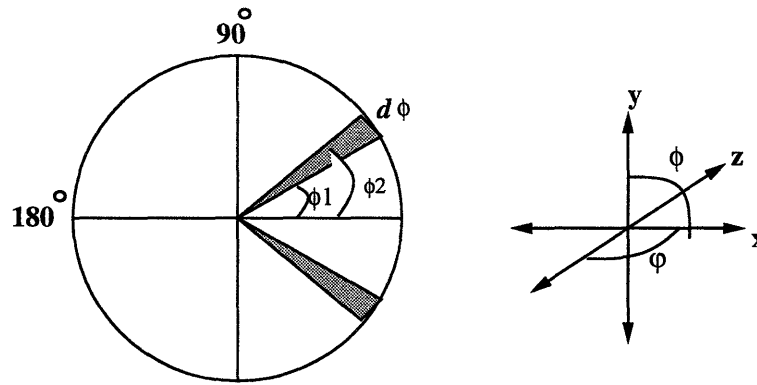
Another useful term is the mean free path, which is the average distance a neutron travels before, or between, an interaction for any given nuclide, neutron energy, and reaction.

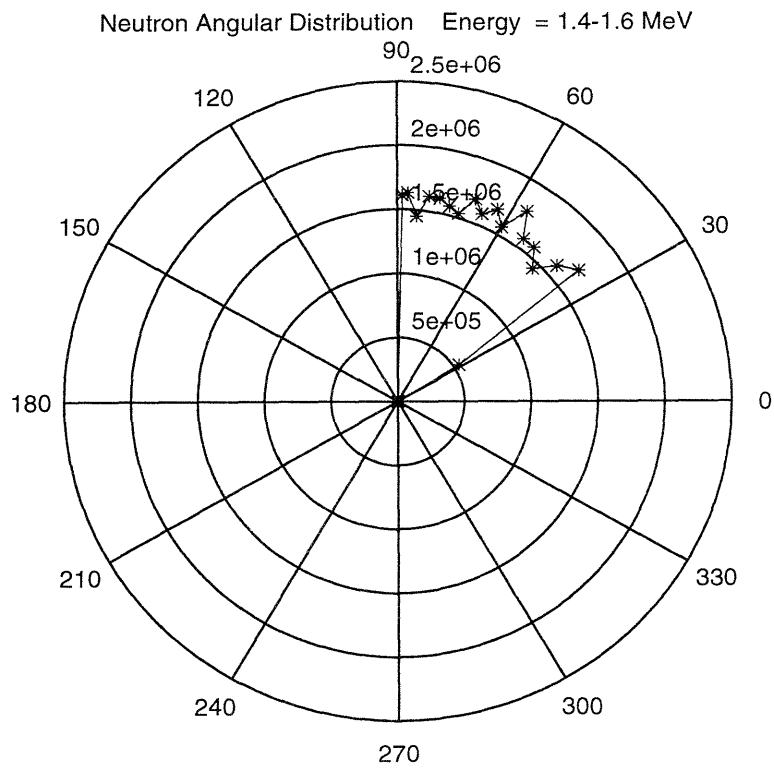
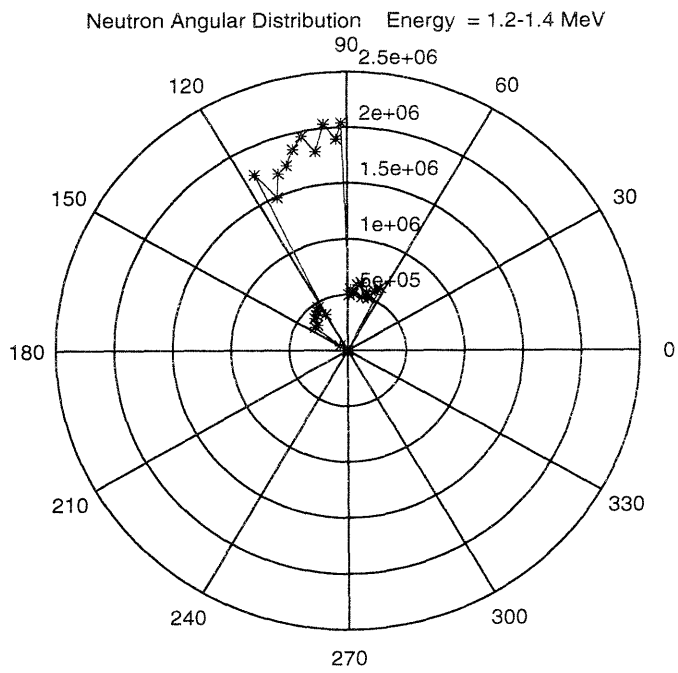
$$\lambda = \frac{1}{\Sigma} \quad (\text{AII.7})$$

## Appendix III

### Neutron Source Energy-Angular-Flux Distribution

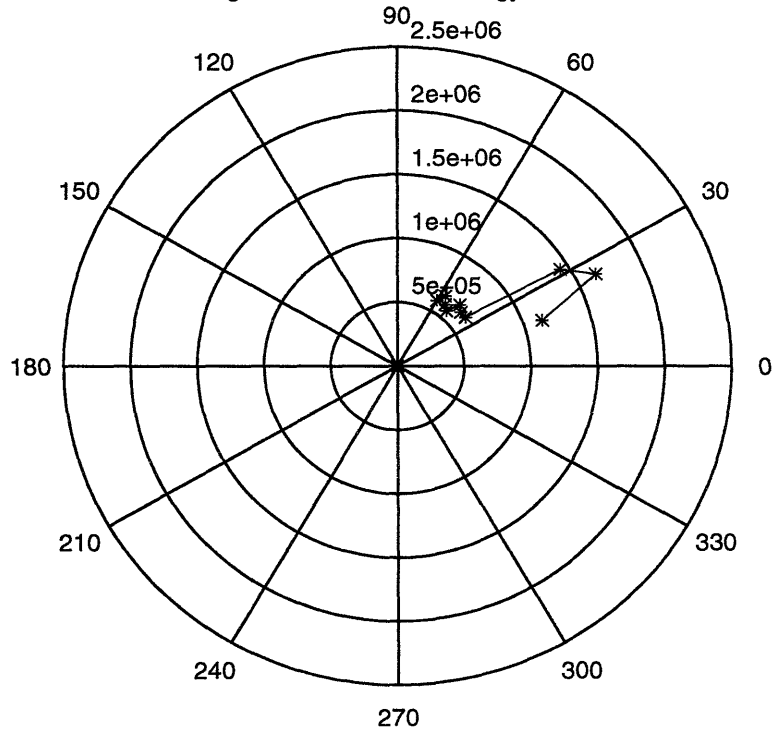
Shown here is a series of figures similar to 4.3a illustrating the angular distribution of the modeled neutron source for 0.2 MeV energy bins spanning the range of the neutron source energy distribution. As in Fig 4.3a, each point in denotes the average flux across a section of the spherical surface defined by the surface  $2\pi\sin\phi d\phi$ , symmetric about  $\phi$ . Source intensity was  $10^{10}$  n/s.



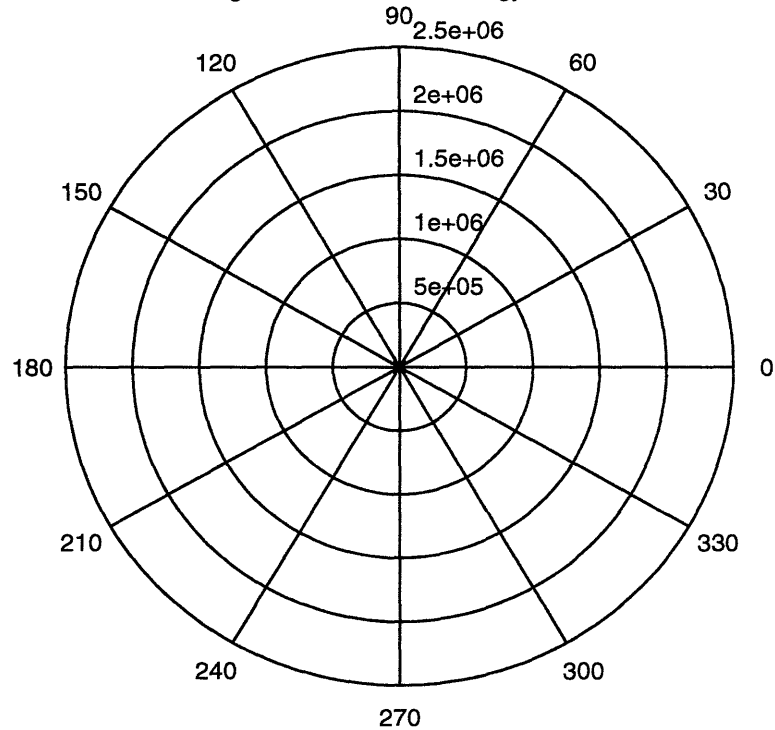


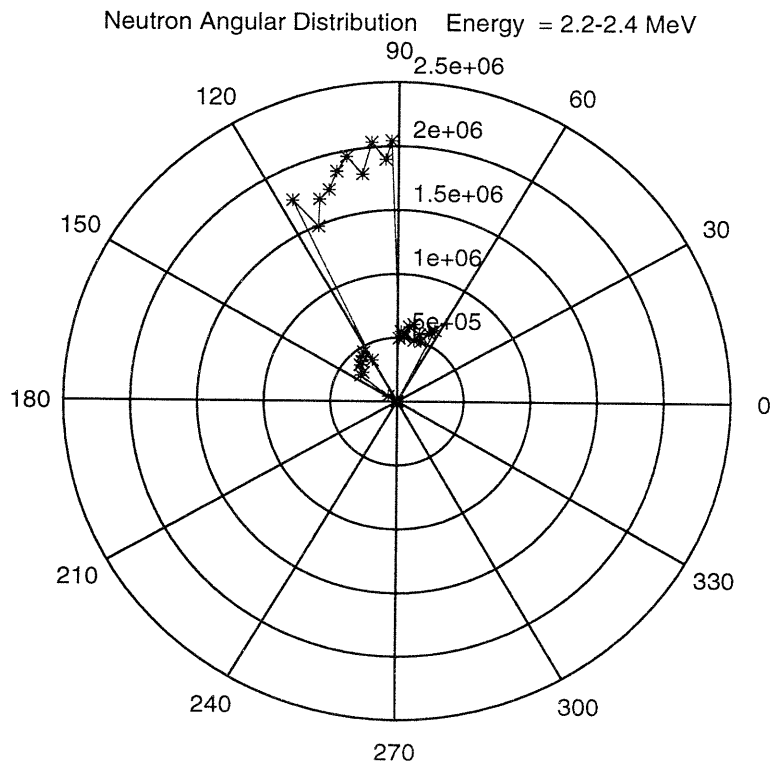
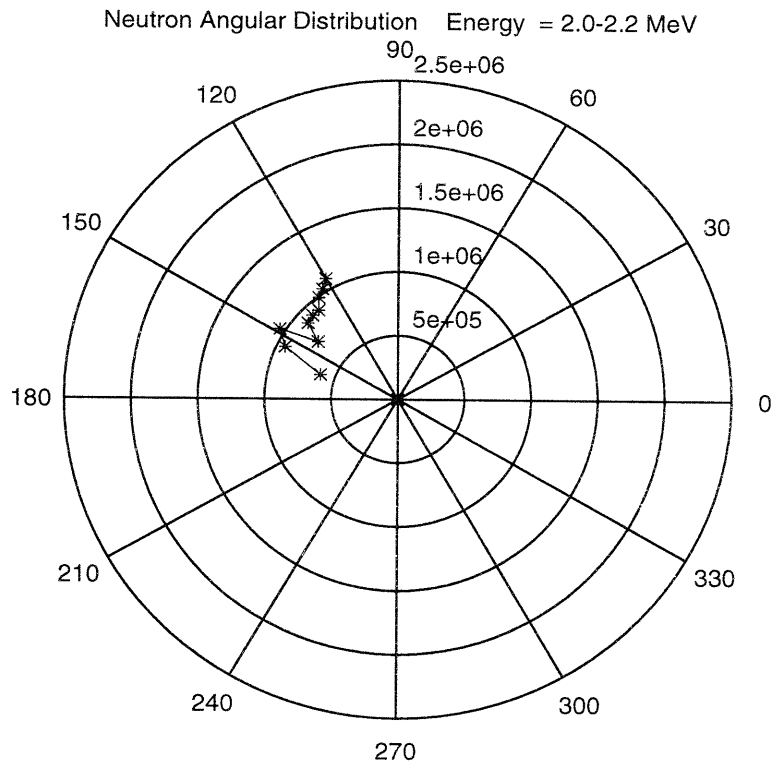


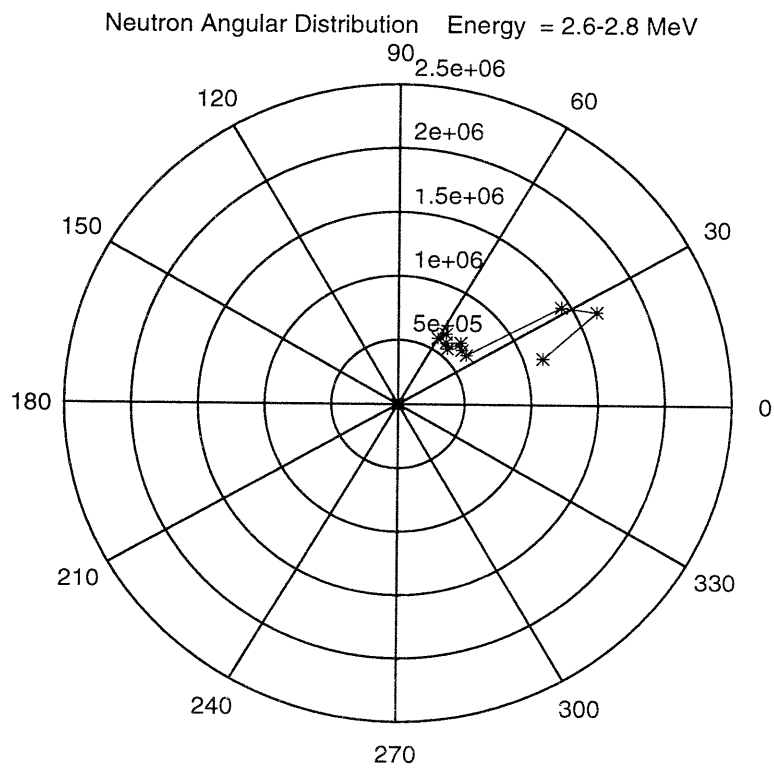
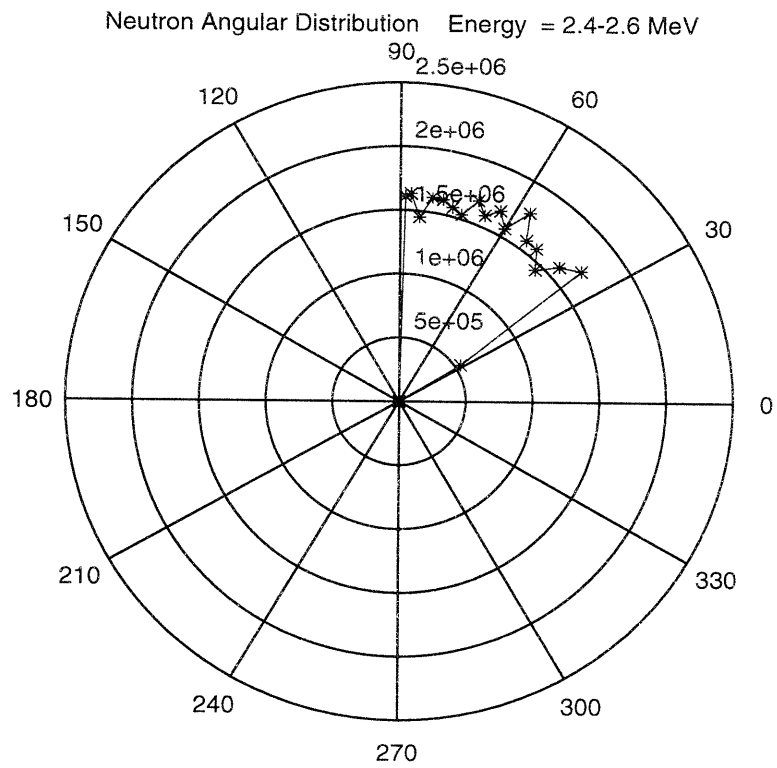
Neutron Angular Distribution Energy = 1.6-1.8 MeV

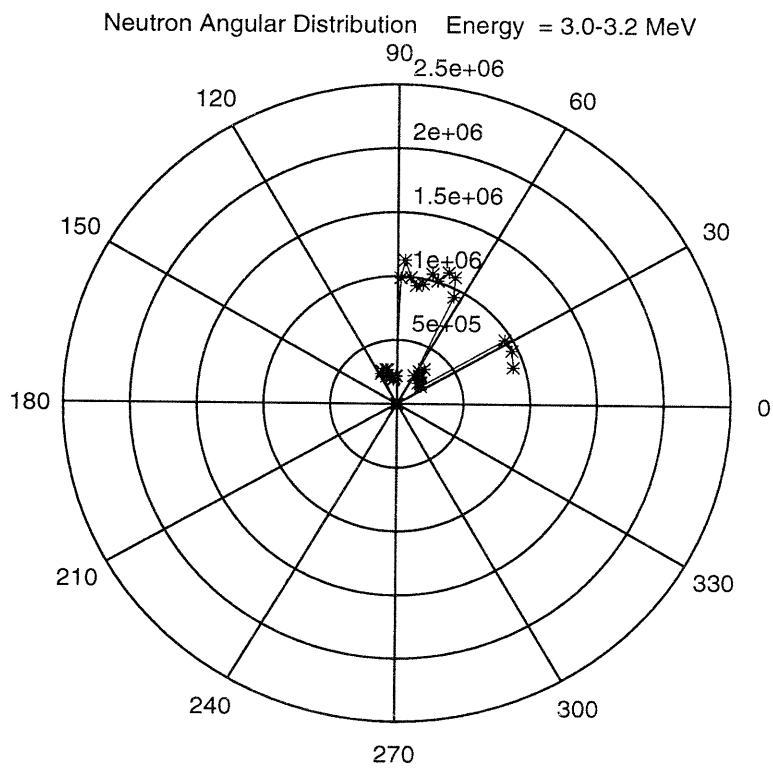
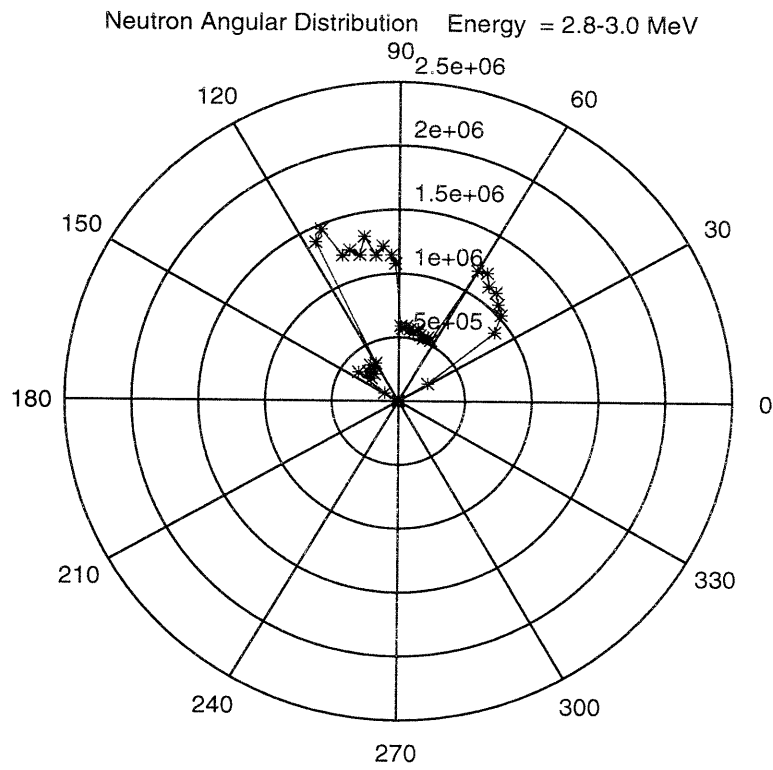


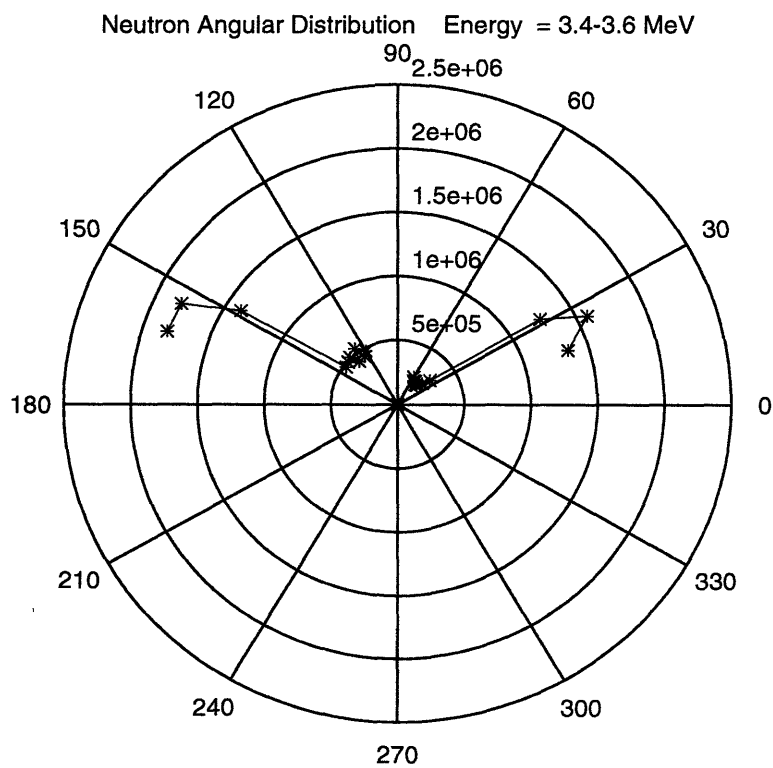
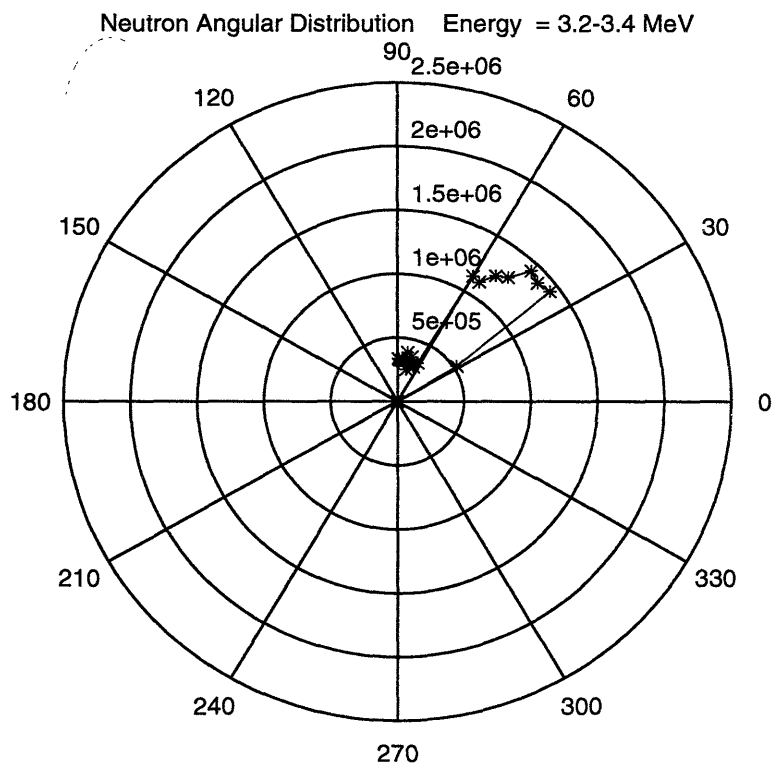
Neutron Angular Distribution Energy = 1.8-2.0 MeV

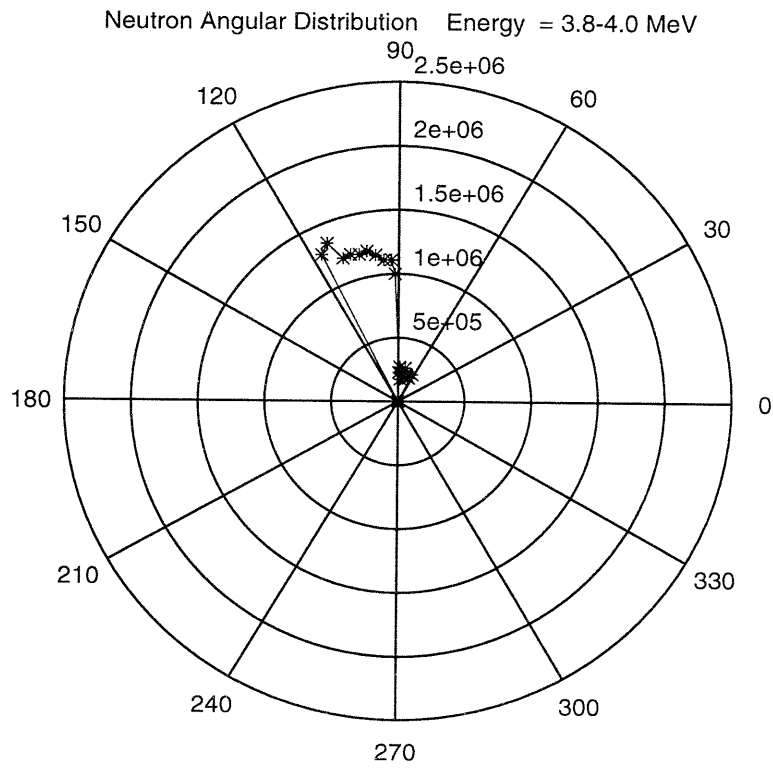
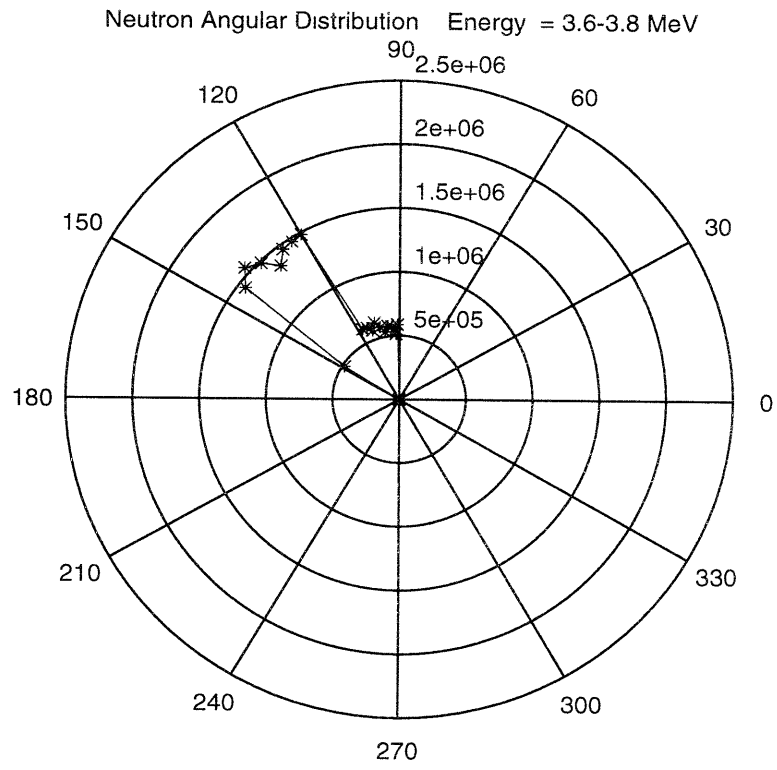


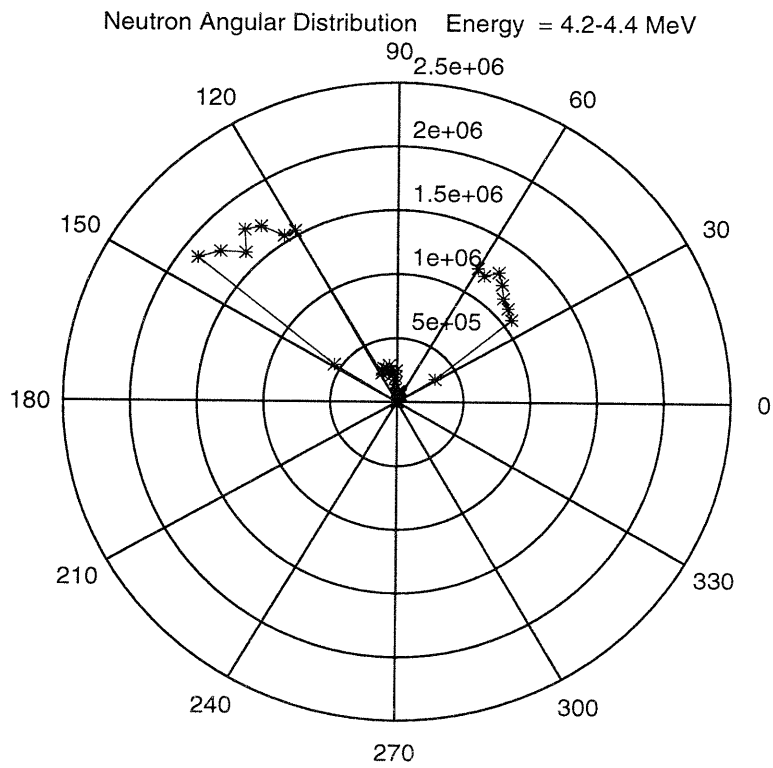
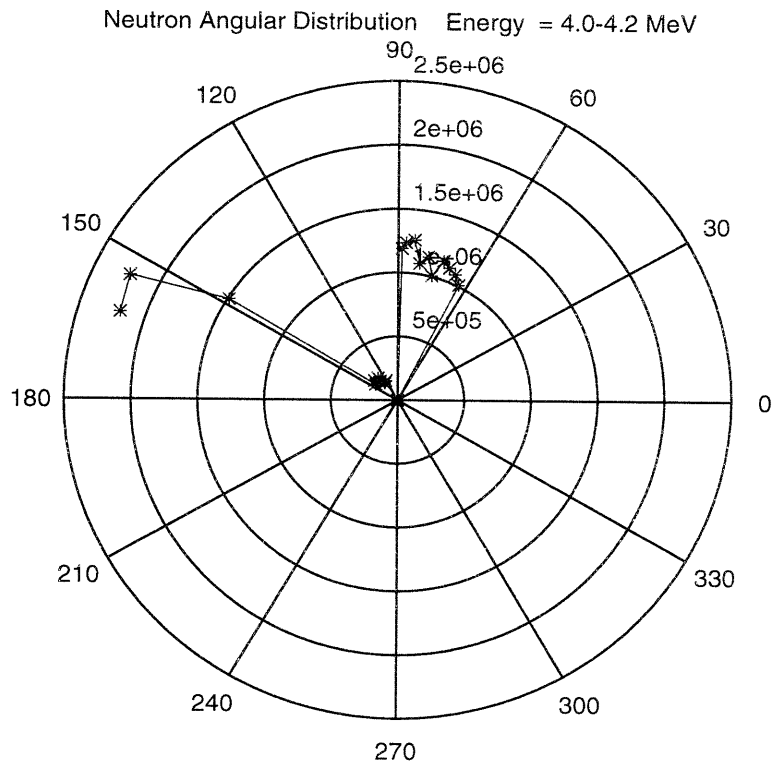




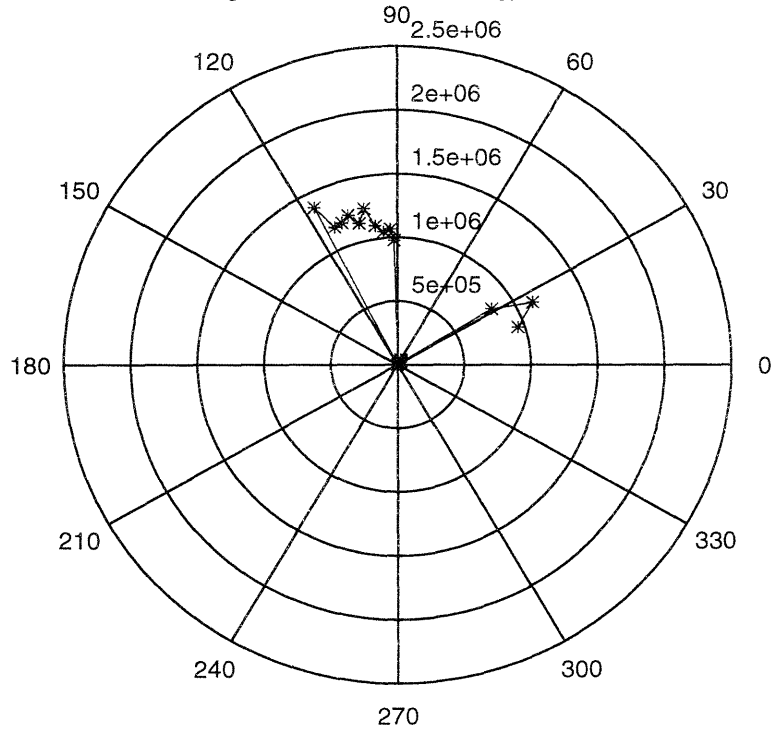




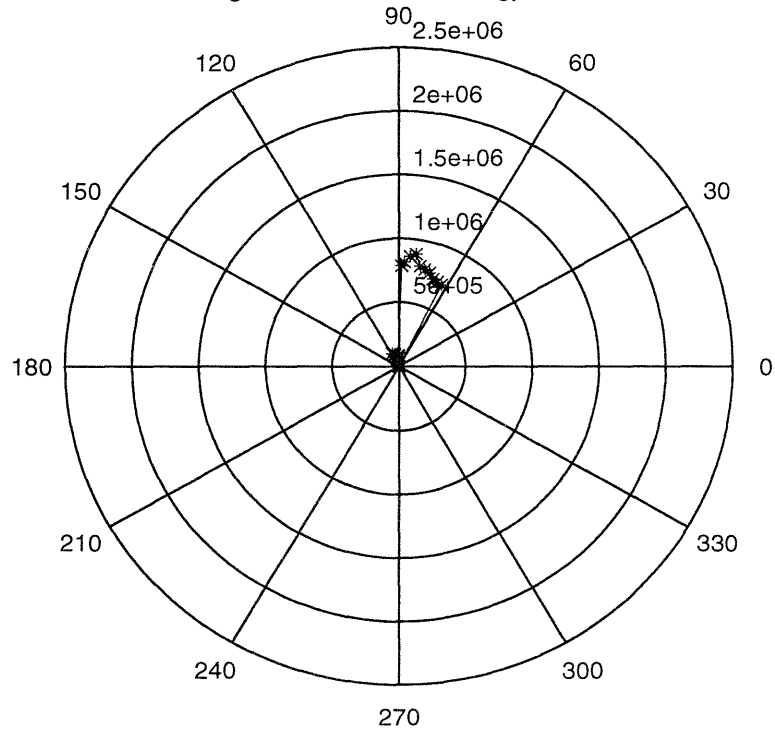




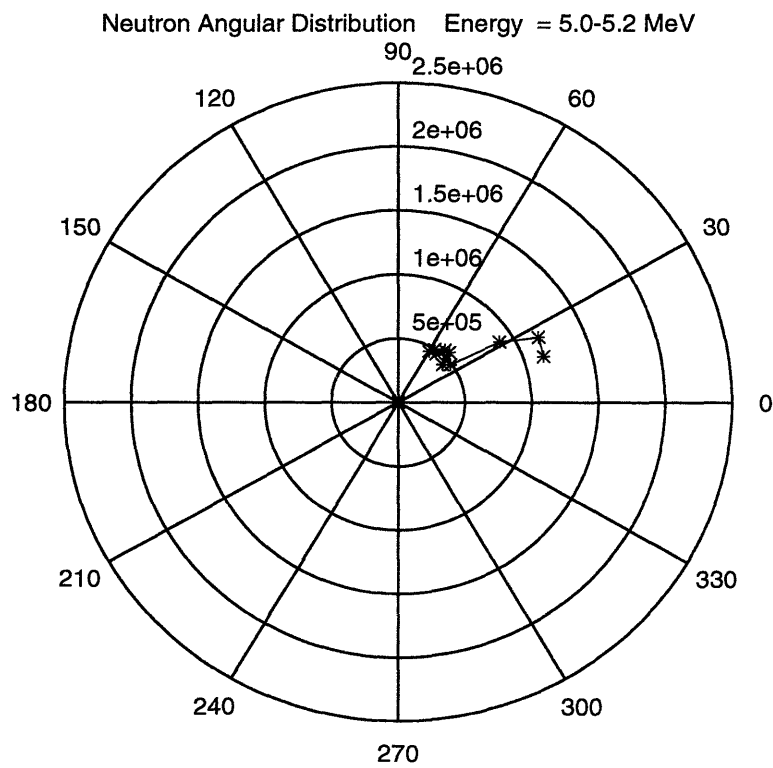
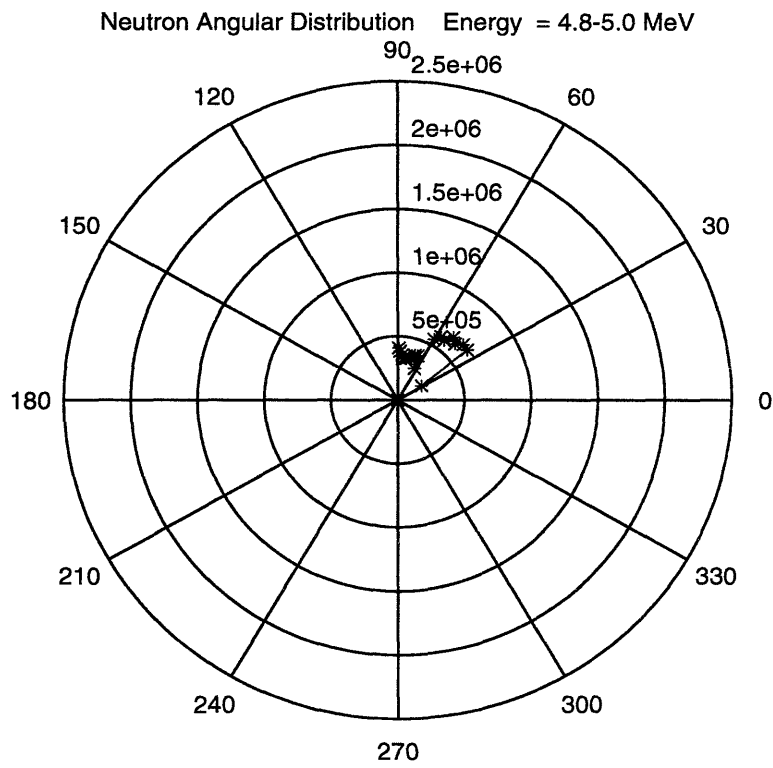
Neutron Angular Distribution Energy = 4.4-4.6 MeV



Neutron Angular Distribution Energy = 4.6-4.8 MeV







# Appendix IV

## Moderator Thermal Neutron Flux Density

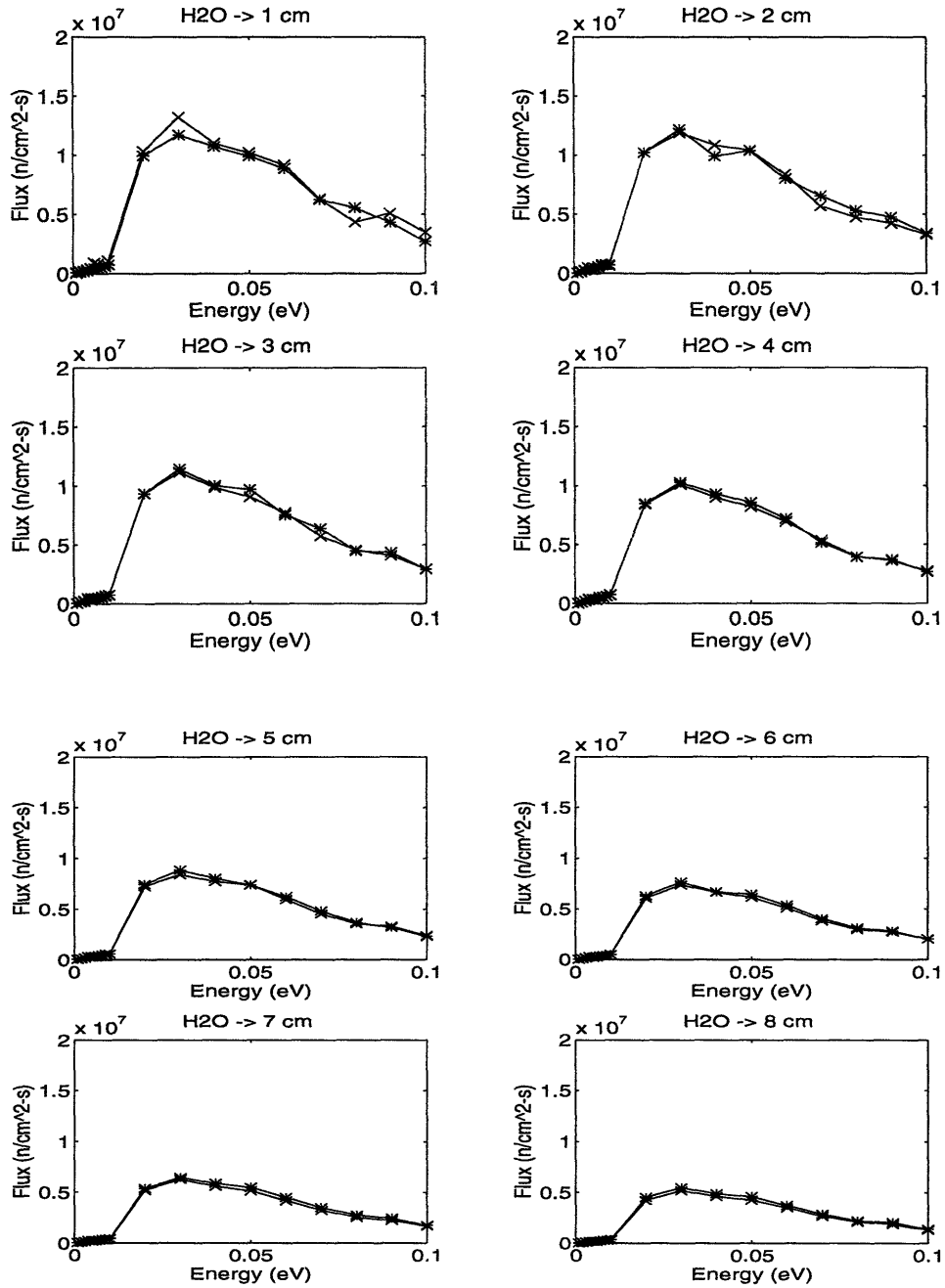


**Figure AIV.1:** Thermal neutron flux density for H<sub>2</sub>O (1-8 cm from source).  
(\*) Backward hemisphere, (x) Forward hemisphere.

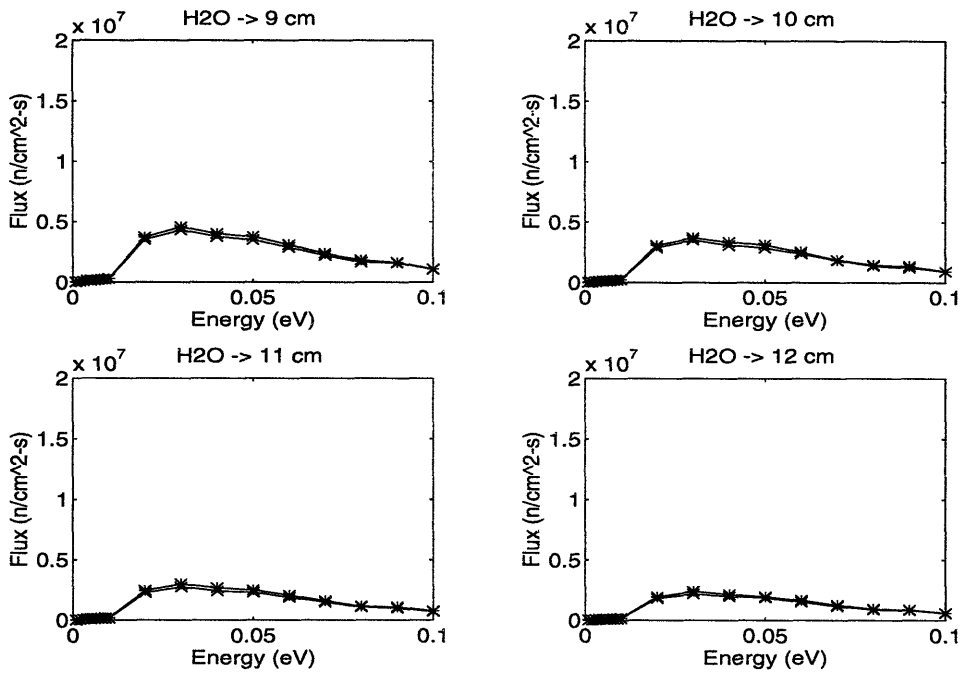


**Figure AIV.2:** Thermal neutron flux density for H<sub>2</sub>O (9-12 cm from source).  
 (\*) Backward hemisphere, (x) Forward hemisphere.

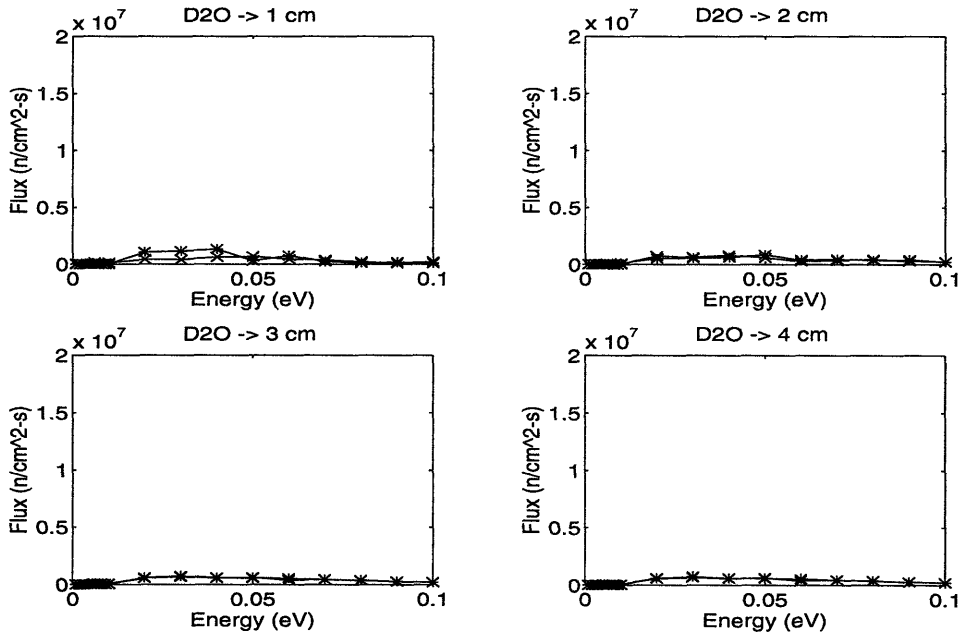


**Figure AIV.3:** Thermal neutron flux density for D<sub>2</sub>O (1-4 cm from source).  
 (\*) Backward hemisphere, (x) Forward hemisphere.

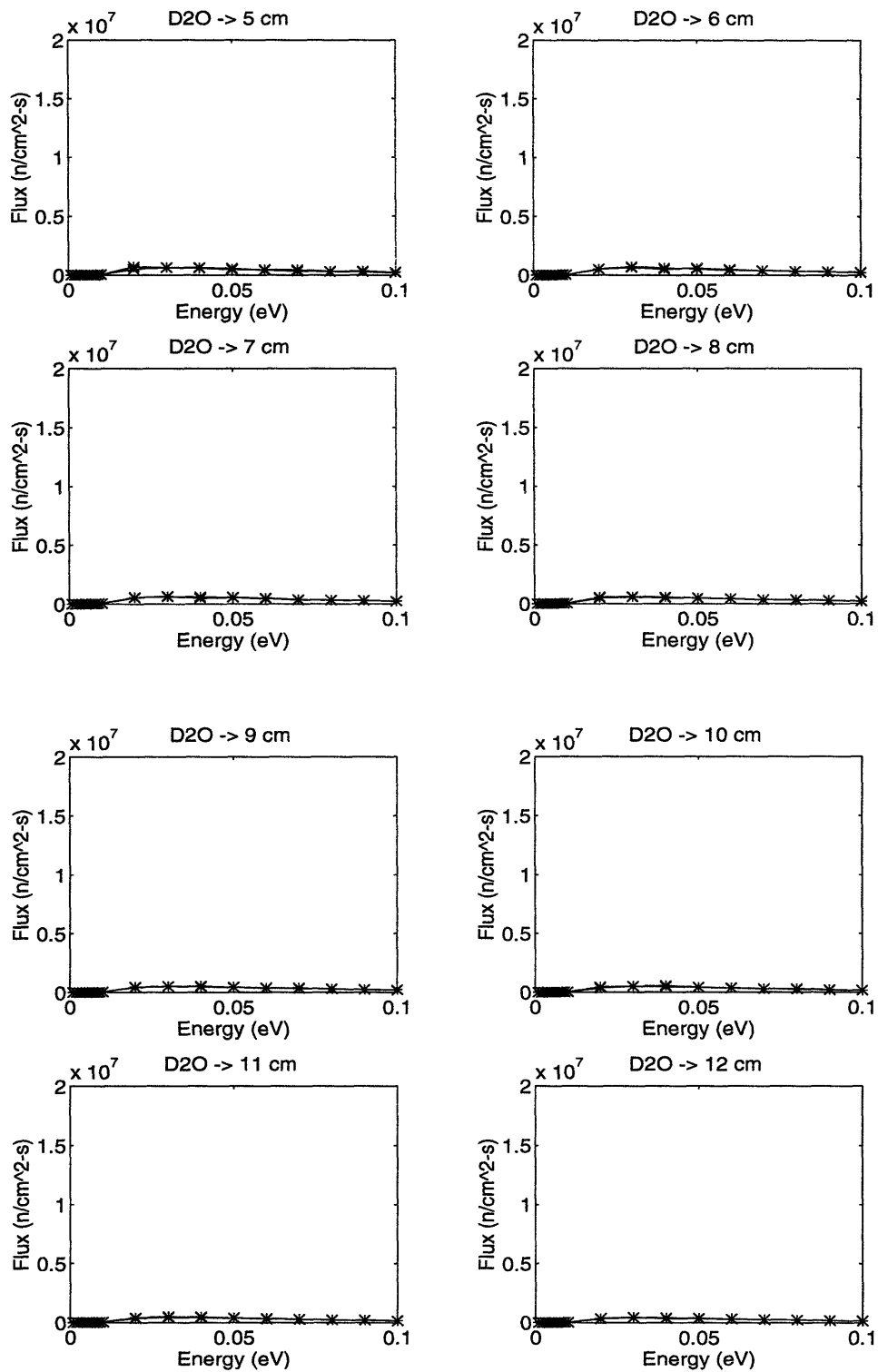


**Figure AIV.4:** Thermal neutron flux density for D<sub>2</sub>O (5-12 cm from source).  
 (\*) Backward hemisphere, (x) Forward hemisphere.

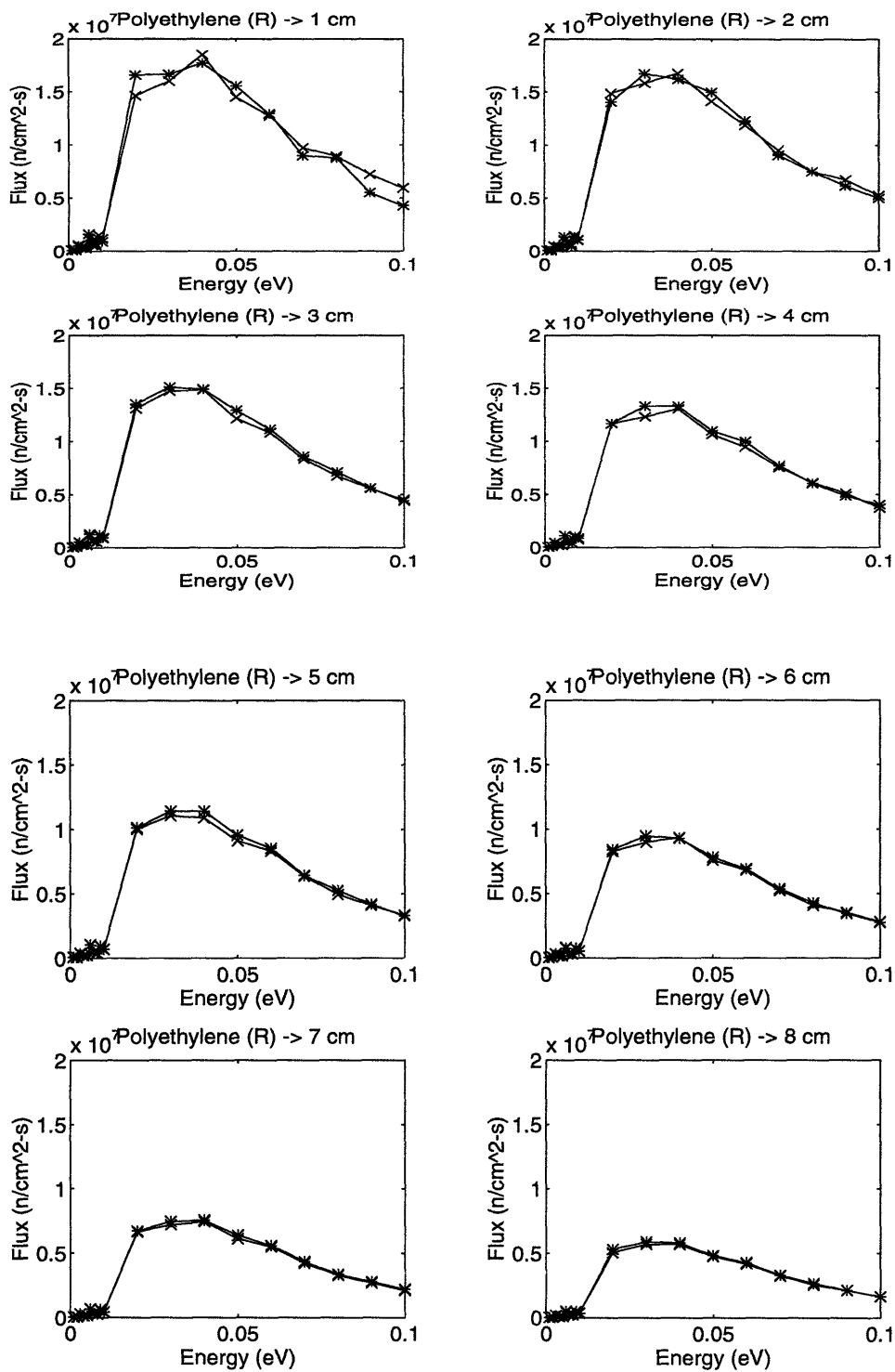


**Figure AIV.5:** Thermal neutron flux density for polyethylene with Be reflector (1-8 cm from source). (\*) Backward hemisphere, (x) Forward hemisphere.

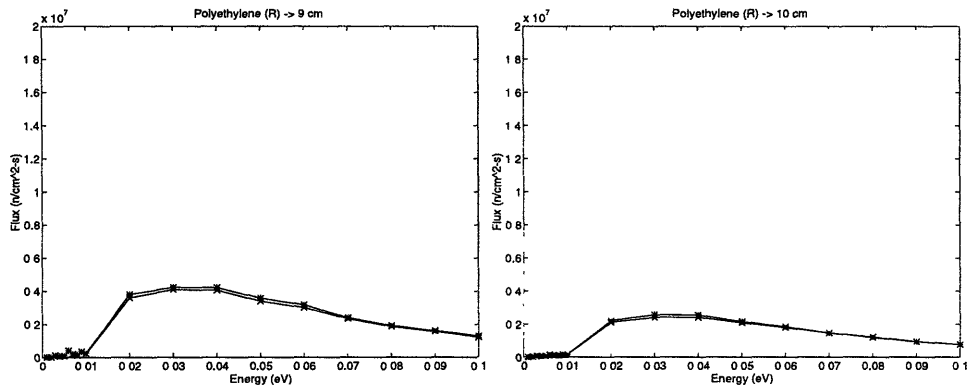


**Figure AIV.6:** Thermal neutron flux density for polyethylene with Be reflector (9-10 cm from source). (\*) Backward hemisphere, (x) Forward hemisphere.

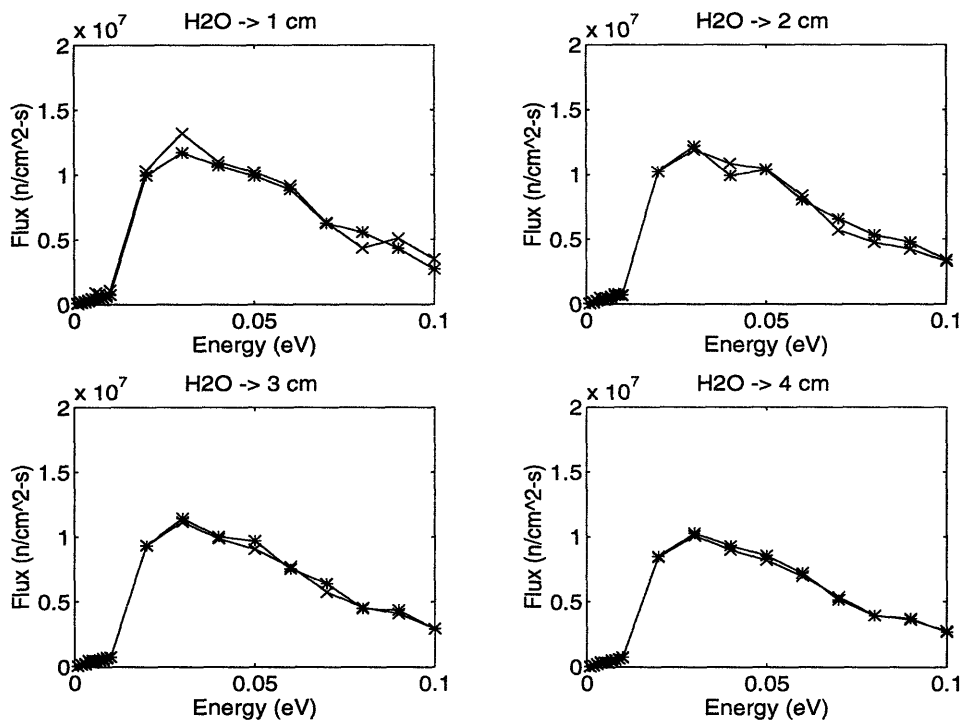


**Figure AIV.7:** Thermal neutron flux density for H<sub>2</sub>O with Be reflector (1-4 cm from source). (\*) Backward hemisphere, (x) Forward hemisphere.

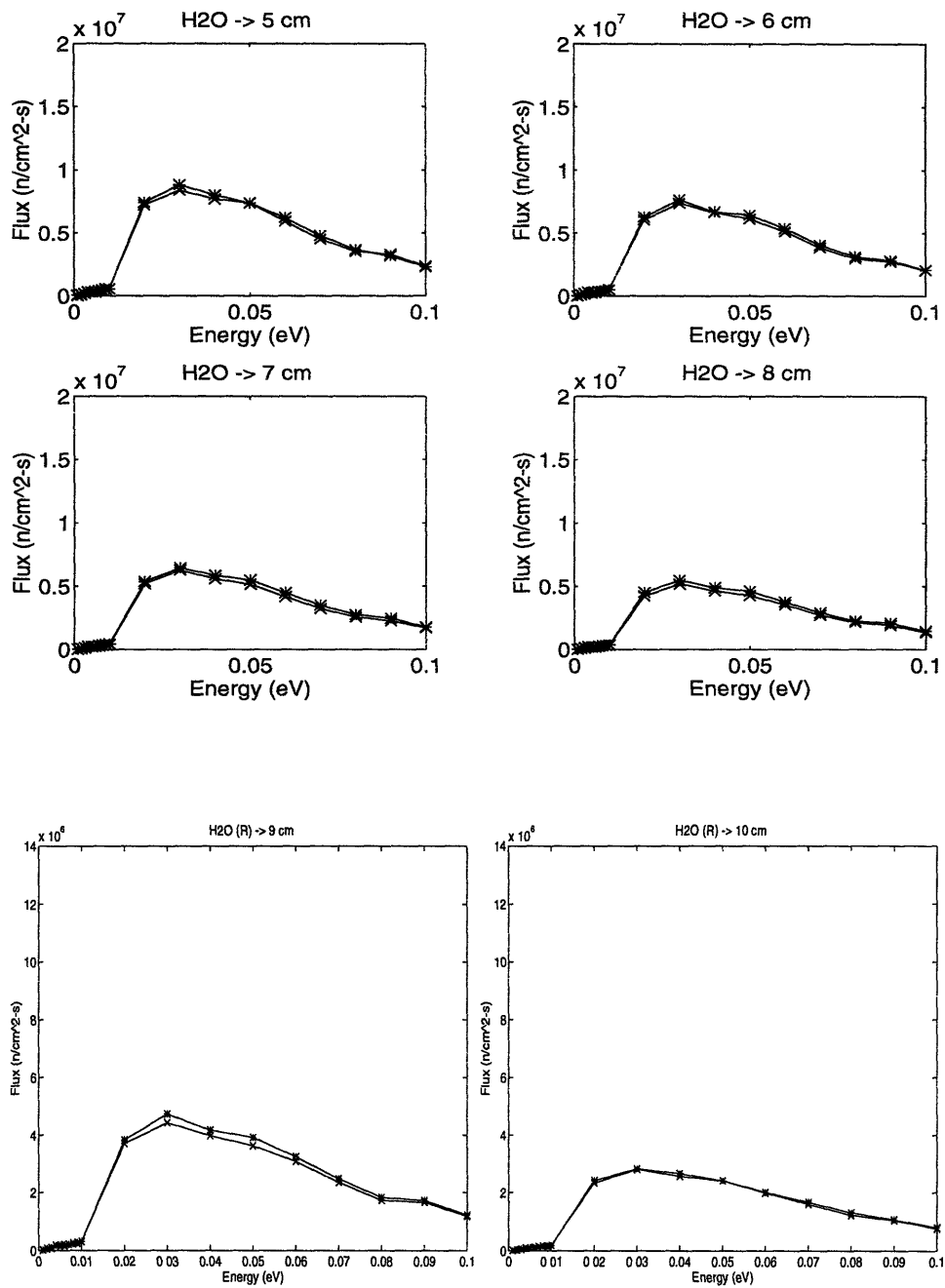


**Figure AIV.8:** Thermal neutron flux density for H<sub>2</sub>O with Be reflector (5-10 cm from source). (\*) Backward hemisphere, (x) Forward hemisphere.

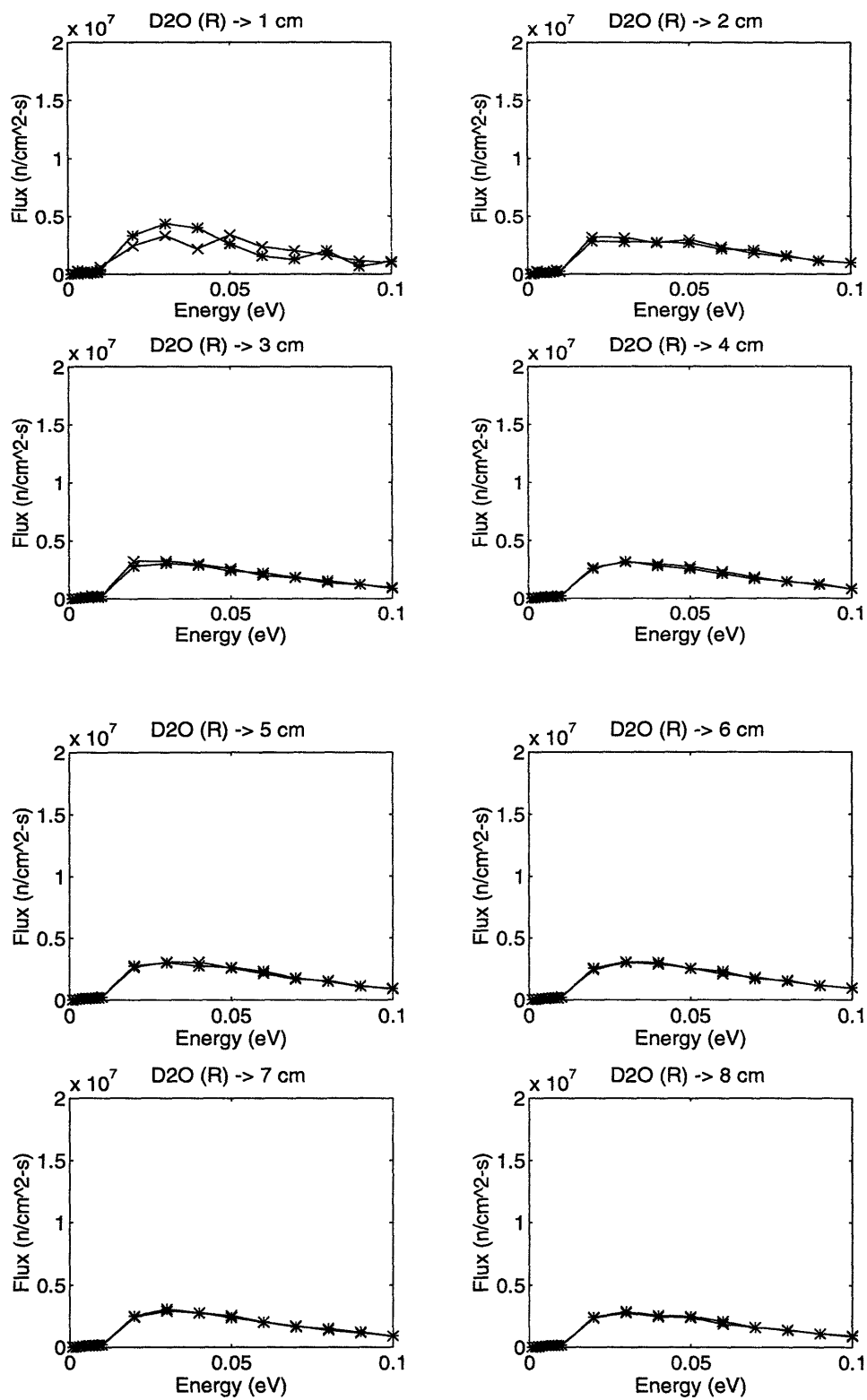


**Figure AIV.9:** Thermal neutron flux density for D<sub>2</sub>O with Be reflector (1-8 cm from source). (\*) Backward hemisphere, (x) Forward hemisphere.



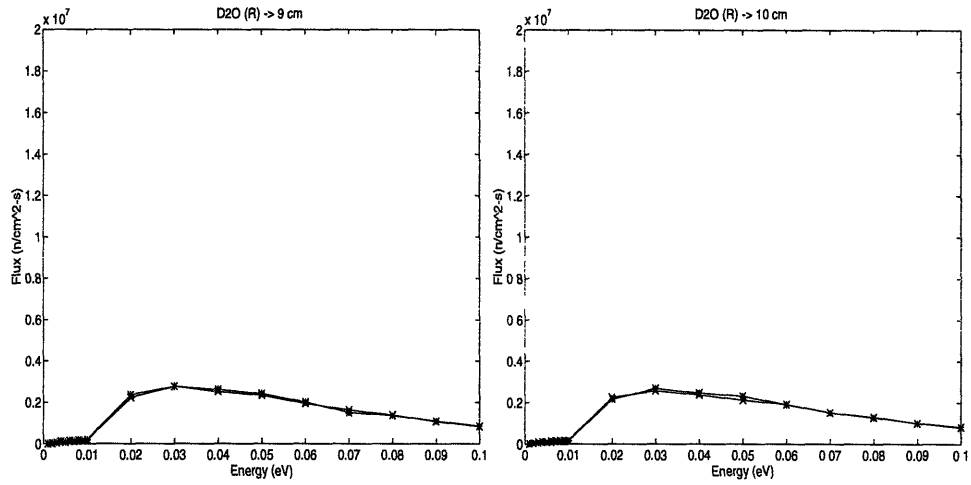


**Figure AIV.10:** Thermal neutron flux density for D<sub>2</sub>O with Be reflector (9-10 cm from source). (\*) Backward hemisphere, (x) Forward hemisphere.